

Journal Name

Crossmark

PAPER

RECEIVED
dd Month yyyyREVISED
dd Month yyyy

Mathematical derivation and verification of the amplitude of LISA's interferometric signals on an ultra-stable interferometer testbed

Alvise Pizzella^{1,2,*} , Lennart Wissel^{1,2} , Miguel Dovale-Álvarez^{1,2} , Pablo Martínez Cano^{1,3} , Rodrigo García Álvarez^{1,2} , Christoph Bode^{1,2} , Juan José Esteban Delgado^{1,2}  and Gerhard Heinzl^{1,2} 

¹Max Planck Institute for Gravitational Physics (Albert Einstein Institute), D-30167 Hannover, Germany ²Leibniz Universität Hannover, D-30167 Hannover, Germany ³University of Granada, 18012-Granada, Spain *Author to whom any correspondence should be addressed.

E-mail: alvise.pizzella@aei.mpg.de **E-mail:** gerhard.heinzl@aei.mpg.de

Keywords: LISA, Gravitational Waves, Heterodyne Efficiency, Differential Wavefront Sensing, Interferometric noise, Quadrant Photodiodes

Abstract

The Laser Interferometer Space Antenna (LISA) mission aims to detect gravitational waves by interferometrically measuring the change of separation between free-falling test masses (TMs). LISA's interferometers must deliver $\text{pm}/\sqrt{\text{Hz}}$ sensitivity while accommodating beam tilts up to 1 mrad at the photodiodes, which degrade the interferometric amplitude and increase the induced readout noise coupling. This paper uses an analytical framework developed by the authors in a previous work, based on minimal and justified approximations, that relates beam tilt to the resulting heterodyne signal amplitude in a generic two-beam interferometer with circular-area photodiodes (PDs). A set of interferometric topologies is analyzed, all of high relevance for LISA. We derive the exact amplitude response for an infinite detector and a closed-form approximation for finite detectors, and we validate both against numerical simulations and experimental measurements on an ultra-stable LISA-representative testbed. We then use this model to quantify the phase-noise amplification arising from reduced signal-to-noise ratio (SNR) under tilt, showing that curvature mismatches between the interfering beams substantially enhance this effect. Finally, we introduce a compact function that captures the angular dependence of correlated and uncorrelated phase noises in quadrant photodiode (QPD)-based readouts. Here, a new noise feature, caused by wavefront curvature mismatch, is predicted and measured for the first time. These results indicate that controlling wavefront curvature mismatch in the test mass interferometer (TMI) is essential to limit excess phase noise. The models and results derived in this paper, although originating in the context of LISA, are general and can be applied to any interferometric topology undergoing tilts with pivot on the detector plane.

1 Introduction

The quest for the detection of gravitational waves started with Joseph Weber at the University of Maryland in the early nineteen sixties, using resonant bar detectors at room temperature [1]. This first generation of detectors was followed by a second generation of cryogenic resonant bar antennas, which operated between 1985 and 2010 [1]. As these failed to obtain sufficient evidence to claim a detection, an alternative technology for gravitational-wave detection, laser interferometry, was proposed by Weber [2]. The foundations for its use in the Laser Interferometer Gravitational-Wave Observatory (LIGO) were established by Rainer Weiss in [3].

After several years of effort, finally, on 14 September 2015, the Advanced LIGO detectors, a second-generation laser interferometer sensitive in the Hz-kHz band, first detected a gravitational wave signal originating from a binary black hole merger, designated event GW150914 [4]. This landmark observation firmly established laser interferometry between free-falling test masses (TMs) as a mature and effective technology for gravitational-wave detection, thereby advancing its further development. Currently, a third-generation ground-based detectors, such as the Einstein Telescope [5] and Cosmic Explorer [6], is

under development; their low-frequency sensitivity, however, is ultimately constrained by ground motion and by the residual noise due to the length and angular control systems needed to maintain the interferometers in a suitable operating point [7]. Accessing the rich sub-Hz gravitational-wave spectrum requires moving away from such noise sources, and hence moving to space; this is the motivation of the LISA mission [8].

LISA will enable the exploration of a rich region of the gravitational-wave spectrum, in the frequency range between 0.1 mHz and 1 Hz. The mission was officially adopted by European Space Agency (ESA) in 2024 [9]. Core enabling technologies — residual TM acceleration at the 10^{-15} m/s² level in interplanetary orbit, drag-free spacecraft control, and picometer-precision interferometric displacement sensing — were successfully demonstrated by the LISA Pathfinder (LPF) mission, launched on 3 December 2015 [10, 11, 12].

Unlike LPF, however, LISA is designed to have the longest measurement baseline ever implemented in a scientific experiment: 2.5 million km between spacecraft. This design requires a novel heterodyne interferometry scheme capable of operating over interplanetary distances. Demonstrating its performance on ground is indeed profoundly challenging.

LISA probes the separation between free-falling TMs that are shielded from external disturbances by their host spacecraft. The TM-to-TM measurement is split into three sub-measurements:

- (i) a TM to spacecraft displacement measurement in the transmitting spacecraft, performed in the TMI;
- (ii) a spacecraft-to-spacecraft displacement measurement, performed in the science interferometer (SCI);
- (iii) a second TM to spacecraft TMI measurement in the receiving spacecraft.

An reference interferometer (RFI) is added as a necessary phase reference within each spacecraft, linking the two onboard lasers [13].

The LISA spacecraft exchange laser beams that propagate for $\sim 2.5 \times 10^9$ m, or ~ 8.3 light-seconds. During this journey, the TEM₀₀ Gaussian beam diverges into a several-kilometer-wide profile, of which only a 30 cm portion is captured by a receiving telescope. This results in a "flat-top", or "top-hat (TH)", beam profile [14], which further propagates through the interferometer. This received beam (Rx) is interfered with a local TEM₀₀ beam called Tx beam — as it is a fraction of the beam being transmitted — producing a heterodyne beat note whose differential phase variations encode path length variations in the optical link. The combination and detection of these beams occurs on the LISA-optical bench (LOB) [15]. The LOB consists of an ultra-low-expansion glass baseplate, to which optical elements are bonded via hydroxide-catalysis bonding [16]. Each spacecraft hosts two LOBs, establishing the triangular links of the constellation.

The ambitious sensitivity of pm/Hz^{1/2} is challenged by several noise sources. According to recent estimates, Tilt-to-length (TTL) coupling noise — which was a major noise source in LPF [17] — is one of the main contributors to the overall noise floor in LISA [18]. TTL coupling is caused by the unavoidable angular jitter of the spacecraft, and its optical components, with respect to the TMs and the line of sight, and the consequent spurious path length signals that the jitter produces.

In LISA, beam tilts mainly originate from a well-defined pivot, which allows the use of custom-designed imaging systems to suppress TTL. Tilts of the spacecraft result in rotations of the Rx beam wrt. the receiving telescope entrance pupil, which is in turn imaged into a fixed aperture located on the LOB, called Rx-clip. The Rx-clip is then imaged onto the SCI photodiodes, ensuring that the impact of spacecraft tilts on the pathlength signals is minimized.

TTL primarily affects the SCI, and its influence on the optically measured path length variations Δs is mitigated through three mechanisms. First, the Drag-Free and Attitude Control System (DFACS) actively stabilizes the attitudes and alignment of both spacecraft and TMs, reducing the overall angular jitter. Second, custom imaging systems passively suppress TTL by mapping the relevant beam pivot points onto the PDs [19, 14]. Third, the residual path length variations $\Delta s(\varphi, \eta)$ are removed in post-processing using the independently measured tilt angles [20]. Accurate subtraction and control require an angular readout with precision near 1 nrad/ $\sqrt{\text{Hz}}$ in the LISA band, provided by the differential wavefront sensing (DWS) technique.

The performance of both the longitudinal and angular readout is affected by the alignment of the interfering beams. The presence of large tilts degrades the overlap, or heterodyne efficiency (HE), of the two beams, ultimately leading to a smaller signal and a consequently reduced SNR. The induced asymmetry in the case of non-zero tilts may also affect the otherwise very high common-mode rejection, a key factor in the very high sensitivity of DWS.

A complete description of the HE generally requires numerical evaluation of detector-plane integrals. In this article, we instead develop an analytical approach based on physically justified approximations. This yields compact expressions for the first few orders Maclaurin coefficients of the HE response on single-element PDs (SEPDs) and QPDs, expressed in terms of fundamental geometrical parameters:

wavelength, beam profile and sizes, wavefront curvatures, and PD diameter. We then validate these expressions through comparison with a high-stability optical testbed representative of the LISA LOB.

We then use these results to quantify the impact of beam tilts on the noise in the longitudinal pathlength signal (LPS) and DWS signals in LISA's readout architecture. We investigate, in particular, the impact of wavefront curvature mismatches, as these lead to diverse HEs across the segments of a QPD. Our considerations suggest introducing a new function, derived from the HE and encompassing the overall QPD's response to tilts, to enable a straightforward derivation of the QPD signal's noise. We derive this in a general context using two Gaussian beams (GBs), which can be applied to any interferometric topology subject to tilts. We further derive this for a GB-TH interferometric topology, which is relevant mostly only for spaceborne interferometers as LISA, Taiji [21] and Tianqin [22], or Grace-Follow On [23].

Finally, we apply these results to LISA's TMI, to quantify the noise benefits of intentionally tilting the TMs to compensate for misalignments in the LOB's build.

Section 2 introduces the testbed; Section 3 and Section 4 develop the analytical model; Section 5 presents the experimental verification; Section 6 analyzes the consequences for phase noise; and Section 7 considers the noise trade-offs associated with operating the TM at a small static tilt.

2 Setup

2.1 Overview of the testbed

A testbed for simulating the above-described effects on the LOB was developed by the authors of [24]. The TTL coupling and DWS Optical Bench Simulator (TDOBS) testbed was primarily designed to demonstrate, in a LISA-representative manner, that imaging systems can effectively suppress TTL coupling [24]. In addition to its initial scope, TDOBS can serve as a versatile platform for testing several other aspects of LISA's metrology, such as imaging systems, photoreceivers, readout systems, and mechanisms for compensating linear TTL [24]. The optical layout is shown in Fig. 1.

The testbed consists of two Zerodur[®] glass-ceramic baseplates: the optical bench (OB) and the telescope simulator (TS). The OB is a simplified realization of the LOB, featuring a single interferometer that can emulate any of LISA's three interferometers. The TS, an optical ground-support equipment mounted above the OB, provides beams representative of either the TMI (a tilting GB) or the SCI (a tilting TH beam), referred to as Rx Gaussian-beam (Rx-GB) and Rx flat-top (Rx-FT), respectively. The TH beam allows for testing the SCI in a relatively compact space.

A pair of steering mirrors on the TS synthesizes beam tilts representative of TM motion or spacecraft attitude fluctuations. The testbed was recently upgraded to operate with beat notes in the 5–28 MHz range (i.e., the LISA heterodyne band) and with low-noise photoreceivers (PRs) comparable to those foreseen for LISA [25, 26].

2.2 Laser modulation bench

The laser modulation bench generates and delivers three beams (Rx, Local Oscillator (LO), and Tx) to TDOBS. All beams originate from a single NPRO-type Nd:YAG laser at 1064 nm stabilized to a molecular iodine reference, achieving a frequency stability of approximately 1000 Hz/√Hz at 1 mHz [27].

The testbed uses three tunable optical frequencies to simulate the three LISA beams. To generate these, the main beam is split into three paths and sent through a double-pass acousto-optic modulator (AOM) stage [28], providing MHz-level frequency shifts with high tuning bandwidth and efficient fiber coupling. The Rx beam is further split using a half-wave plate and a polarizing beam splitter (PBS). The resulting four beams are coupled into single-mode, polarization-maintaining optical fibers and routed to TDOBS. Of the two Rx beams, one is sent to the Rx-GB fiber injector optical sub-assembly (FIOS), while the other is directed to the flat-top beam generator (Rx-FT) [14].

2.3 Photoreceivers

In this paper, we refer to the PR as the ensemble formed by the PD and its associated trans-impedance amplifier (TIA). LISA employs round quadrant photodiodes (QPDs), i.e. PDs whose active area is divided into four rotationally symmetric segments (see Fig. 2). The used material for the absorption layer is indium gallium arsenide (InGaAs), chosen due to its high quantum efficiency at 1064 nm despite the higher capacitance. Each QPD segment is read out by a dedicated TIA.

Each quadrant photoreceiver (QPR) segment must satisfy an input-equivalent current noise density requirement $\tilde{i}_{\text{en}}(f) < 2 \text{ pA}/\sqrt{\text{Hz}}$ within the LISA heterodyne band. An expression valid for beat note frequencies in this band is given in eq. (1) from [29], noting its explicit frequency dependence:

$$\tilde{i}_{\text{en}}(f) \approx \sqrt{\frac{4k_B T}{R_F} + \tilde{i}_{\text{ACE}}^2 + \left(2\pi f(C_{\text{PD}} + C_{\text{ACE}})\tilde{e}_{\text{ACE}}\right)^2}, \quad (1)$$

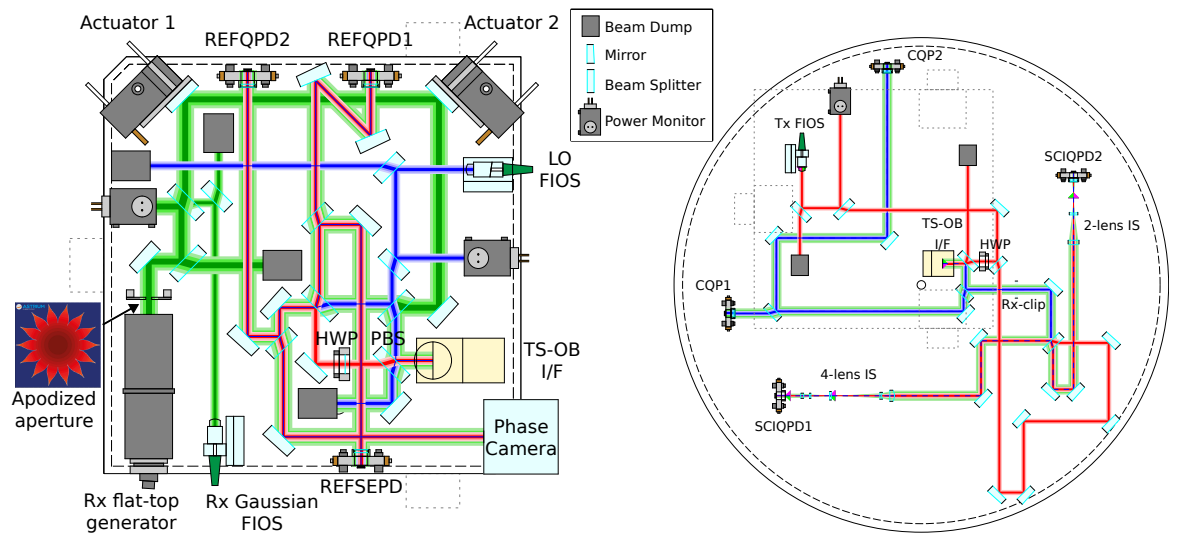


Figure 1: Optical layout of the testbed. *Left:* The telescope simulator (TS) provides the optical bench (OB) (right) with laser beams (Rx-GB and Rx-FT, both in green) to simulate LISA’s TMI and SCI. The first beam is a TEM₀₀ Gaussian beam provided by a fiber injector optical sub-assembly (FIOS) with a width of ~2 mm. The second is a flat-top beam generated by clipping a 9 mm radius beam Gaussian beam on an apodized aperture; this generates a beam flat in both intensity and phase with a diameter of ~4 mm [24]. The TS sits on top of the OB and is held by three Zerodur® feet, which are indicated by the dashed lines. An optical link is established via a vertical interface (TS/OB I/F). A pair of actuated steering mirrors, named "act1" and "act2" on the left, on the TS tilt the Rx beams around the Rx-clip (this is an aperture, which is physically located on the LOB) to simulate either the spacecraft jitter in the SCI or the TM jitter on the TMI. An additional FIOS generated TEM₀₀ Gaussian beam, the LO (blue), is used as an alignment aid for the TS with respect to the OB and as a phase reference. The TS hosts four optical copies of the Rx-clip (located on the OB). In these optical copies, one reference SEPD (REFSEPD), two reference QPDs (REFQPDs) and a phase camera are placed. *Right:* The OB is a simplified version of the OBs in LISA. It features a local FIOS generated TEM₀₀ Gaussian beam, the Tx beam, and only one interferometer, where all three the Tx, Rx, and the LO beams interfere. At the interferometer’s two output ports, the two science QPDs (SCIQPDs) are placed. These output ports feature imaging systems to image the point of rotation of the Rx beam onto the center of the QPDs and reduce TTL coupling. In this Figure we show the two types of imaging systems that were developed for TDOBS, one featuring 2 lenses, and one featuring 4 lenses. During the work reported in this article, two 4-lens imaging systems were used. The TS’s nominal position on top of the OB is indicated by the dashed lines. Such position is defined with the aid of a Calibrated QPD Pair (CQP); this is a pair of large silicon QPDs positioned on the LOB. When the LO beam impinges on the center of both QPDs of the CQP, the Tx beam TS also propagates to the center of the PDs on the TS. Figure and caption from [26].

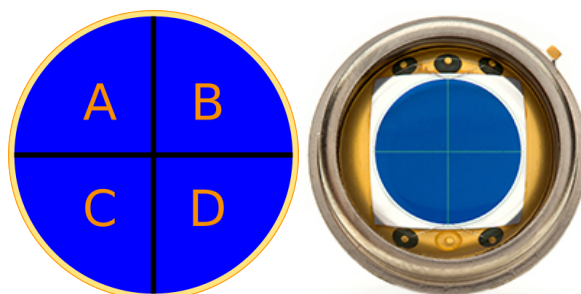


Figure 2: *Right:* Picture of a large commercial QPD. *Left:* definition of the used segment-nomenclature throughout the paper. The area between the segments is called *slit*. Depending on the specific QPD model, the slit can be either insensitive, partially sensitive, or even more sensitive than the active area itself. Note that the QPDs in this experiment use a diameter of 1 mm.

where the subscript ACE denotes the active circuit element used as the amplifier; \tilde{i}_{ACE} , \tilde{e}_{ACE} and C_{ACE} represent its current noise density, voltage noise density, and input capacitance, respectively. C_{PD} is the PD (or QPD segment)'s capacitance, R_F is the feedback resistance of the TIA, k_B is the Boltzmann constant and T is the temperature of the TIA.

Minimizing this electronic noise requires careful optimization of both the TIA and the QPDs. In particular, the QPD-segment's capacitance must be kept as small as possible to avoid noise increases at higher heterodyne frequencies. Since $C_{PD} \propto r_{QPD}^2$, where r_{QPD} is the QPD radius, this constrains the detector's size, and further introduces a trade-off with the DWS gain [26, Section III].

The QPRs used in TDOBS were developed close to the current LISA baseline [30]. As the flight-model QPDs are still under development, we had to chose commercial counterparts. For the QPDs, the GAP1000Q model from GPD Optoelectronics was selected. This features a 1 mm diameter active area with 20 μm slits. The associated TIAs follow the present LISA baseline and use a transistor first-stage amplifier [30]. Characterized using the white-light method [29], these TIAs exhibit input-equivalent current noise below 2 pA/ $\sqrt{\text{Hz}}$ up to ~ 15 MHz (see Fig. 3).

A total of four such QPRs are used in TDOBS: two serve as REFQPDs on the TS in optical copies of the Rx-clip, while the remaining two are SCIQPDs placed at the interferometer output ports on the OB.

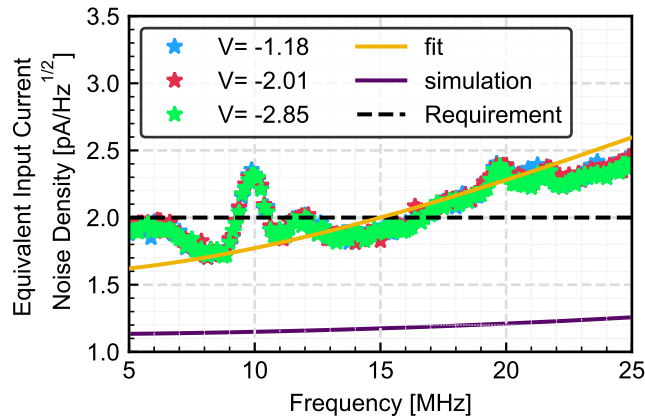


Figure 3: Measurement with three different light intensities, SPICE simulation, and fit of the electronic noise from the TIA used for the photodiodes in TDOBS. The fit function is $f(x) = \sqrt{p_0^2 + (p_1 x)^2}$, reproducing eq. (1).

2.4 Imaging Systems

Pupil-to-pupil imaging systems are used to mitigate TTL coupling, as well as beam walk, defined as the lateral displacement of the beam spot on the PD surface along one or both transverse axes [14].

Mathematically, they can be described using the ray-transfer matrix formalism [31, chapter 15] by a 2×2 $\begin{pmatrix} A & B \\ C & D \end{pmatrix}$ matrix with null B element. As ray-transfer matrices have a determinant of one when there is no change of refraction index, this implies that $D = A^{-1}$:

$$\mathbf{r}' = M_{IS}\mathbf{r}, \quad M_{IS} = \begin{pmatrix} m^{-1} & 0 \\ C & m \end{pmatrix}, \quad (2)$$

where $\mathbf{r} = (x, \theta)$ is the vector describing the ray's position and angle, and m is the *angular magnification*. Moreover, such systems can be designed to produce a collimated output for a collimated input by imposing $C = 0$ in eq. (2). The imaging systems used in TDOBS and in LISA, including the telescope, are of this collimating type.

When a GB is propagated through an imaging system, its mode changes. For a collimating system, a GB characterized by spot radius w_{in} and radius of curvature (RoC) R_{in} at the input pupil plane emerges with

$$w_{out} = m^{-1} w_{in}, \quad (3)$$

$$R_{out} = m^{-2} R_{in}. \quad (4)$$

In LISA, imaging systems also serve to compress the beam size, allowing for smaller QPR dimensions. As a consequence, the beam's incidence angle is magnified by a factor m (see eq. (2)).

LISA implements the imaging systems such that the tilt pivot of the beam arriving at the PR coincides with the detector center. Furthermore, the telescope functions as a four-mirror collimating imaging system that images the Rx beam onto the Rx-clip, and additional collimating imaging systems further image the

Rx-clip onto each QPR surface. This peculiarity of LISA's design allows for a description of tilts as only rotations about the centres of the QPDs. This principle is depicted in Figure 4.

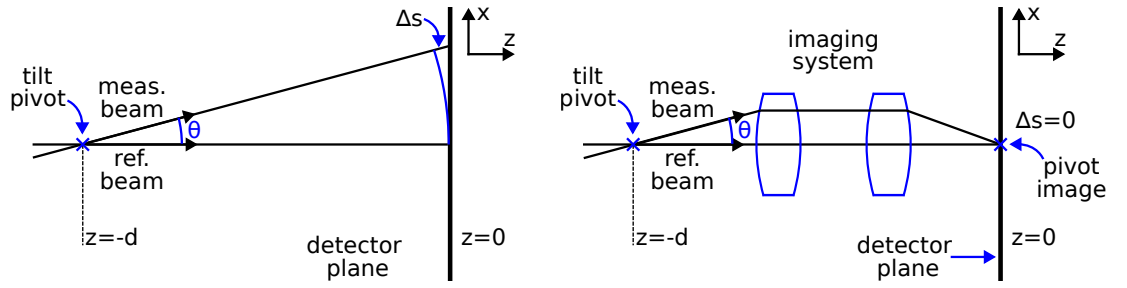


Figure 4: Description of the lever arm effect between two beams, which dominates the geometrical TTL. Two beams, the reference beam and the measurement beam, interfere. The resulting intensity is measured by a PR located on the $z = 0$ plane. The measurement beam can rotate about the pivot point $(0, 0, -d)^T$, representing either the Rx-clip or the TM's surface in LISA. Such a tilt causes the measurement beam to propagate over a longer path; we denote the additional path-length as Δs . The extra path length is interferometrically measured at the PR; if Δs is not constant in time, it generates a noise term, and such noise is called TTL. Imaging systems reduce the lever arm effect between two beams and beam walk by imaging the point of rotation of the beam into the center of the PR. This means the optical path length is unchanged by the tilt, as light always takes the shortest path. As a consequence of this design, beam tilts in LISA have the center of the QPD as a rotation pivot and reduced undesired beam walk on the QPD. Figure from [26].

2.5 Phasemeters

The phasemeter is responsible for reading out the phases of the electrical beat notes from the QPR; in addition to the phases, also the amplitude of each beat note is returned. TDOBS employs two phasemeters, both sampling the input signals at $f_s = 80$ MHz. The first is based on I/Q demodulation and requires precise knowledge of the beat note frequencies to be tracked. It is an older 16-channel model, not designed to meet the stringent LISA phase noise requirement, but remains essential to TDOBS because its control software drives the steering mirrors on the TS.

The second phasemeter is an engineering-model precursor of the LISA phasemeter. This 8-channel version features digital phase-locked loop (DPLL)-based beat-note tracking and is designed to meet the required LISA performance up to its Nyquist frequency. Its dominant noise sources are thermally induced phase fluctuations and analog-to-digital converter (ADC)-clock jitter. The latter is mitigated by injecting a common electrical pilot tone that is tracked across all channels, enabling post-processing corrections [32, 33, 34].

2.6 Longitudinal Path Length Signal

The LPS signal is the main QPD signal, and encodes the gravitational wave's signal. This signal combines the readout of the four segments to synthesize a SEPD-like response. We define the LPS as the average phase (AP) across the four segments normalized by the wave number $k = 2\pi/\lambda$,

$$\text{LPS}_{\text{AP}} = \frac{1}{k} \phi_{\text{AP}} = \frac{1}{k} \frac{\phi_A + \phi_B + \phi_C + \phi_D}{4}, \quad (5)$$

This average-phase LPS is used throughout the paper as the effective longitudinal readout of the QPD. Another possible combination of the four segments' readout to recover a longitudinal signal, the LPF-LPS, is discussed in [35].

2.7 Differential Wave Front Sensing

The DWS [36, 37] signal is the QPD signal used for the angular readout. Its principle is to measure the relative wave-front angle between two interfering beams using the phase differences of their heterodyne beat notes across the QPD. As sketched in Fig. 5, a reference beam is assumed to be centered and normally incident, while the measurement beam rotates around the detector center. The segment phases ϕ_i are combined to form the vertical and horizontal DWS combinations:

$$\text{DWS}_v = \phi_{\text{top}} - \phi_{\text{bottom}} = \frac{\phi_A + \phi_B - \phi_C - \phi_D}{2}, \quad (6)$$

$$\text{DWS}_h = \phi_{\text{right}} - \phi_{\text{left}} = \frac{\phi_A - \phi_B + \phi_C - \phi_D}{2}, \quad (7)$$

which depend on the vertical and horizontal tilt angles η and φ , respectively. For small tilts, the response is approximately linear [38, 26],

$$\text{DWS} \approx \kappa_1 \theta, \quad \kappa_1 \sim r_{\text{QPD}}/\lambda \sim 10^3, \quad (8)$$

with θ being the tilt angle representative of either η or φ , and κ_1 the zero-angle DWS gain. We refer to θ as the wavefront angle (WFA) when indicating it is the angle recovered from DWS. A more accurate treatment that accounts for the GB structure and larger tilt angles is reported in [26]. A practical phasemeter implementation is described in [39].

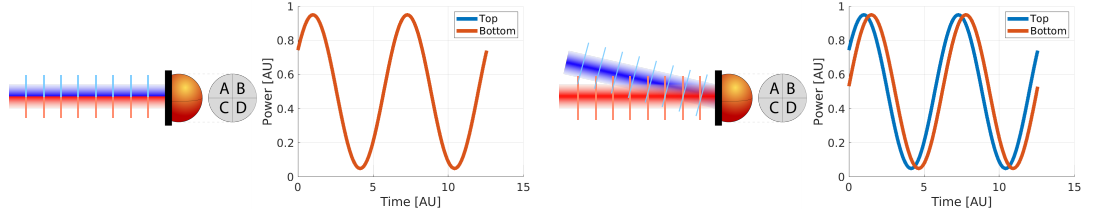


Figure 5: Principle of DWS. A reference beam (red) and measurement beam (blue) with a MHz-scale frequency difference produce a heterodyne beat tone on each QPD segment. When aligned (left), all beat notes share the same phase. When the measurement beam is tilted (right), the wave fronts reach the top segments earlier than the bottom ones, producing a phase difference proportional to the tilt angle. Figure from [26].

3 Tilted beam intensity

This section derives the relation between the HE and the tilt angle θ in the case of the interference of two fundamental-mode GBs, or one fundamental-mode GB and a TH, beam being detected by a PD. Two PD shapes are considered: a SEPD and a QPD. The former, although of no interest for LISA, is included in the analysis for completeness, as it is easier to model and also furnishes a useful comparison. This estimation can be done analytically under the assumption that the PD's radius is much larger than the beam's spot radius; this is calculated in subsections 3.2 and 3.3 in the case of two GBs impinging on an infinite SEPD and infinite QPD, respectively. Subsection 3.4 extends these calculations to the case where the measurement beam is a TH. An analytical extension of this method to a finite and circular PD is also possible; this is calculated in subsections 3.5 and 3.6 in the case of two GBs impinging on a finite SEPD and finite QPD, respectively. This last case also requires the wavefront curvature mismatch between the beams to be small. Subsection 3.7 extends these models to the case where the measurement beam is a TH. A numerical model is also developed, to describe the cases that don't respect these conditions; we report one such model in subsection 3.8, which we compare against the analytical expressions.

3.1 Framework

This subsection defines the mathematical framework of the model and the overlap and HE of two beams. The framework presented in this paper is a further development of that presented in [26, III.A]; here, as the model was used to calculate the DWS signal, only the interference phase was considered, whereas in this work, for the HE, also the beam's amplitude must be considered. Readers who are already familiar with [26] can skip the following lines until eq. (24). For the sake of self-consistency, the initial assumptions are repeated in the following lines.

To start, two fundamental-mode GBs are assumed. The presence of imaging systems, as mentioned in [26, II.D] and in Figure 4, justifies the restriction of the analyzed rotations to those with the pivot located at the PD's center. Let $\vec{x} = (x, y, z)^T$ be the laboratory's reference frame (RF). In this RF, the PD is a surface defined by $z = 0$, and the reference beam propagates along the z -axis. The electric field of the reference beam in the lab's RF is given by

$$\vec{E}(\vec{x})_r = \text{Re} \left[E_r \hat{\epsilon}_r \mathcal{E}_r(\vec{x}) e^{i\omega_r t} \right], \quad (9)$$

$$\mathcal{E}_r(\vec{x}) = \sqrt{\frac{2}{\pi}} \frac{w_{0,r}}{w_r(z_r)} \exp \left(-\frac{x^2 + y^2}{w_r(z_r)^2} + i \left(k \frac{x^2 + y^2}{2R_r(z_r)} + kz_r + \eta(z_r) \right) \right), \quad (10)$$

where $E_r \in \mathbb{C}$ [V/m] is a complex scalar determining the beam's amplitude and initial phase, $\hat{\epsilon}_r = (\epsilon_{x,r}, \epsilon_{y,r}, 0)^T$, $\epsilon_{x,r}, \epsilon_{y,r} \in \mathbb{C}$, $\hat{\epsilon}_r \perp \hat{\epsilon}_z$ is a generic polarization unitary vector of an electromagnetic wave

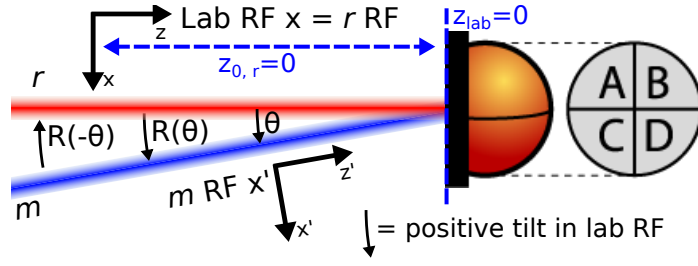


Figure 6: Framework of the used reference frames. The QPD defines the lab's RF, with the QPD's center being located at $\vec{x} = \vec{0}$. The reference beam's RF shares the same coordinates with the lab's RF, but is shifted along the z -axis. The measurement beam's RF is rotated and shifted along the z axis with respect to the lab's RF. A positive tilt of the beam is defined as an anticlockwise tilt. The measurement beam's RF can be obtained by rotating the lab's RF by an angle θ . Dually, the lab's RF can be obtained by rotating the measurement beam's RF by an angle $-\theta$. The tilt shown in the figure causes the measurement beam's path length to the top segments A and B to be larger than that to the bottom segments C and D. Therefore, in such a configuration, the DWS_v signal is positive. Figure from [26].

propagating along the z -axis, $\mathcal{E}_r(\vec{x})$ is the complex scalar wave amplitude, $z_r = z - z_{0,r}$ is the waist position adjusted z -coordinate and $w_{0,r}$ is the reference beam's waist, $w_r(z_r)$, $R_r(z_r)$ and $\eta(z_r)$ are the reference beam's spot size, RoC and Gouy phase at the position z_r , respectively, and $\omega_r = 2\pi\frac{c}{\lambda}$ is the angular frequency. From here onward, we will mostly omit the argument z_r . Equation (10) is normalized such that

$$\int_{\mathbb{R}^2} |\mathcal{E}_r(\vec{x})|^2 dx dy = w_{0,r}^2 \forall z. \quad (11)$$

The total power of the beam can be recovered as

$$P_{0,r} = \frac{1}{2Z} \int_{\mathbb{R}^2} |\vec{E}_r(\vec{x})|^2 dx dy = \frac{1}{2Z} |E_r|^2 w_{0,r}^2 = I_{0,r} w_{0,r}^2, \quad (12)$$

where $Z[\Omega]$ is the wave impedance of the medium in which the beam is propagating and $I_{0,r}$ is the reference beam's intensity [W/m^2].

The measurement beam propagates on a generic axis, which is rotated by a small angle $\theta \ll 1$ around the QPD's center with respect to the z -axis called z' . This axis is used to define the measurement beam's RF in the primed coordinates $\vec{x}' = (x', y', z')^T$. Without loss of generality, this rotation is assumed to be a pitch (vertical) rotation. As justified in Figure 4, the rotation pivot can be assumed to be the QPD's center $(x, y, z)^T = (0, 0, 0)^T$. Therefore, the lab's RF and measurement beam's RF are related by a rotation matrix

$$\begin{pmatrix} x \\ y \\ z \end{pmatrix} = \begin{pmatrix} 1 & 0 & 0 \\ 0 & \cos(\theta) & \sin(\theta) \\ 0 & -\sin(\theta) & \cos(\theta) \end{pmatrix} \begin{pmatrix} x' \\ y' \\ z' \end{pmatrix} \quad \text{or } \vec{x} = R(-\theta)\vec{x}'. \quad (13)$$

The electric field of the measurement beam is expressed by the same eqs. (9) and (10) in the measurement beam's RF. We name this quantity

$$\vec{E}'_m(\vec{x}') = \text{Re} \left[E_m \hat{\epsilon}'_m \mathcal{E}'_m(\vec{x}') e^{i\omega_m t} \right], \quad (14)$$

Expressing $\vec{E}'_m(\vec{x}')$ in the lab's RF requires a change of coordinates. It can be expressed in the same form as

$$\vec{E}_m(\vec{x}, \theta) = \text{Re} \left[E_m \hat{\epsilon}_m(\theta) \mathcal{E}_m(\vec{x}, \theta) e^{i\omega_m t} \right], \quad (15)$$

We now evaluate the relation between all primed and unprimed quantities. The beam's amplitude E'_m is a scalar and does not vary in the change of coordinates: $E_m = E'_m$. The electric field is a vector field; therefore a generic electric field transforms as

$$\vec{E}(\vec{x}) = R(-\theta)\vec{E}'(\vec{x}') = R(-\theta)\vec{E}'(R(\theta)\vec{x}), \quad (16)$$

where in the second step the inverse of eq. (13) has been used. The rotation of the complex scalar wave amplitude of the measurement beam results in eq. (18) as shown in [26]. The polarization unitary vector is also rotated, resulting in eq. (17).

$$\hat{\epsilon}'_m = \begin{pmatrix} \epsilon_{x,m} \\ \epsilon_{y,m} \\ 0 \end{pmatrix} \rightarrow \hat{\epsilon}_m(\theta) = R(-\theta)\hat{\epsilon}'_m = \begin{pmatrix} \epsilon_{x,m} \\ \cos(\theta)\epsilon_{y,m} \\ \sin(\theta)\epsilon_{y,m} \end{pmatrix} \quad (17)$$

This rather complicated expression can be simplified by neglecting the dependence of w_m , R_m and η on the transverse coordinate y . This leads to eq. (19) as shown in [26, section III], making this a linear framework.

$$\begin{aligned} \mathcal{E}_{m, \text{full}}(\vec{x}, \theta) &= \mathcal{E}'_m(R(\theta)\vec{x}) \\ &= \sqrt{\frac{2}{\pi}} \frac{w_{m,0}}{w_m(\sin(\theta)y + z_m)} \exp\left(-\frac{x^2 + (\cos(\theta)y + \sin(\theta)z)^2}{w_m^2(\sin(\theta)y + z_m)} + \right. \\ &\quad \left. + i\left(k\frac{x^2 + (\cos(\theta)y + \sin(\theta)z)^2}{2R_m(\sin(\theta)y + z_m)} + k(\sin(\theta)y + z_m) + \eta(\sin(\theta)y + z_m)\right)\right), \end{aligned} \quad (18)$$

$$\mathcal{E}_{m, \text{approx}}(\vec{x}, \theta) = \sqrt{\frac{2}{\pi}} \frac{w_{m,0}}{w_m} \exp\left(-\frac{x^2 + y^2}{w_m^2} + i\left(k\frac{x^2 + y^2}{2R_m} + \underbrace{ky\theta}_{\text{tilt}} + kz_m + \eta(z_m)\right)\right). \quad (19)$$

The remaining tilt coupling is given by the extra pathlength term $\exp(iky\theta)$. The intensity of the superimposed reference and measurement beams I_{ifm} is recovered by taking the square modulus of the sum of the two electric fields, and dividing it by twice the wave impedance of the medium in which the beam is propagating $Z[\Omega]$:

GB-GB:

$$\begin{aligned} I_{\text{ifm}}(x, y, \theta) &= \frac{1}{2Z} \left[\underbrace{\left(E_r \sqrt{\frac{2}{\pi}} \frac{w_{r,0}}{w_r(z_r)}\right)^2 \exp\left(-2\frac{x^2 + y^2}{w_r(z_r)^2}\right)}_{|E_r|^2} + \underbrace{\left(E_m \sqrt{\frac{2}{\pi}} \frac{w_{m,0}}{w_m(z_m)}\right)^2 \exp\left(-2\frac{x^2 + y^2}{w_m(z_m)^2}\right)}_{|E_m|^2} \right. \\ &\quad \left. + \underbrace{\hat{\epsilon}_r \cdot \hat{\epsilon}_m \left(E_r E_m \frac{2}{\pi} \frac{w_{r,0}}{w_r(z_r)} \frac{w_{m,0}}{w_m(z_m)} \exp\left(-2\frac{x^2 + y^2}{w_{\text{eff}}^2} (1 - i\rho) + i(kz_r + \eta(z_r) - ky\theta - kz_m - \eta(z_m) + (\omega_r - \omega_m))\right)\right)}_{\vec{E}_r \cdot \vec{E}_m + \vec{E}_r^* \cdot \vec{E}_m} + c.c. \right], \end{aligned} \quad (20)$$

where $*$ indicates complex conjugation and the quantities

$$\frac{2}{w_{\text{eff}}^2} = \frac{1}{w_r^2(z)} + \frac{1}{w_m^2(z)}, \quad (21)$$

$$\frac{1}{R_{\text{rel}}} = \frac{1}{R_r(z)} - \frac{1}{R_m(z)}, \quad (22)$$

$$\rho = \frac{w_{\text{eff}}^2 k}{4R_{\text{rel}}}, \quad (23)$$

have been introduced [26]. The quantity w_{eff} is the effective spot radius of the two overlapped beams, and R_{rel} is their absolute wavefront mismatch [26]. The quantity ρ is the effective-spot-radius-normalized wavefront curvature mismatch; an expression for ρ depending only on the fundamental parameters of the interfering beams is derived in [26, eq. (33)] in the case of two fundamental mode GBs. Both R_{rel} and ρ depend on the beam's labelling, and are hence odd under the swapping of the two beams. In this linearized framework, the same holds also for the tilt angle θ . Consequently, any physical effect of a combination of these parameters must respect this symmetry [26].

Our goal is deriving the variation of the amplitude of the beam interference overlap as a function of the tilt and with respect to the individual beam's powers; we hence split the beam's intensity into the three components mentioned in eq. (20). From here on, we make the assumption that both beams have linear and horizontal polarization, given by $\epsilon_m = \epsilon_r = (1, 0, 0)^T$. Since the tilt is vertical, this results in $\hat{\epsilon}_r \cdot \hat{\epsilon}_m = 1$ independently of θ . Note that if both polarization and tilt were vertical $\epsilon_m = \epsilon_r = (0, 1, 0)^T$, then the scalar product $\hat{\epsilon}_r \cdot \hat{\epsilon}_m = \cos(\theta)$ would depend on the tilt angle. This effect, although negligible, must be taken into account due to the vector nature of the electric field. A simplified expression for the overlap intensity term in eq. (20), which still contains the relevant phenomena, is given by

$$I_{\text{simp}}(x, y, \theta) = \frac{2}{\pi} \exp\left(-2\frac{x^2 + y^2}{w_{\text{eff}}^2} (1 - i\rho) - ik y \theta\right) + c.c. \quad (24)$$

The full equation of the intensity eq. (20) can be recovered using eq. (25)

GB-GB:

$$I_{\text{ifm}}(x, y, \theta) = I_r + I_m + C e^{i\psi} \left(I_{\text{simp}}(x, y, \theta) + c.c. \right), \quad (25)$$

where the quantities I_r , I_m , C and Ψ are

$$I_r = \frac{2}{\pi} I_{r,0} \left(\frac{w_{r,0}}{w_r(z_r)} \right)^2 \exp \left(-2 \frac{x^2 + y^2}{w_r(z_r)^2} \right), \quad (26)$$

$$I_m = \frac{2}{\pi} I_{m,0} \left(\frac{w_{m,0}}{w_m(z_m)} \right)^2 \exp \left(-2 \frac{x^2 + y^2}{w_m(z_m)^2} \right), \quad (27)$$

$$C = \hat{\epsilon}_r \cdot \hat{\epsilon}_m \sqrt{I_{r,0} I_{m,0}} \left(\frac{w_{r,0}}{w_r(z_r)} \frac{w_{m,0}}{w_m(z_m)} \right), \quad (28)$$

$$\Psi = kz_r + \eta(z_r) - kz_m - \eta(z_m) + (\omega_r - \omega_m). \quad (29)$$

We use eq. (24) to evaluate the detector-plane integrals, and later revert the result back into the form of I_{ifm} to determine the HE.

Given a PD of any geometry, the power measured by a PD is the integral of the intensity over the PD's surface. Throughout the whole paper, the beams are assumed to be centered on the PD.

$$P_{\text{PD}}(\theta) = \int_{S_{\text{PD}}} dx dy I_{\text{ifm}}(x, y, \theta) \quad (30)$$

The total power can be split into three terms corresponding to the ones underbraced in eq. (20). These are the power of the reference beam $P_{\text{PD},r}$, the power of the measurement beam $P_{\text{PD},m}$, and the *overlap power term* $P_{\text{pd}}(\theta)$. $P_{\text{PD},m}$ depends, in principle, on the tilt angle θ . Such dependency vanishes if the PD's size is much larger than the measurement beam's size, and is negligible otherwise. Hence, the dependence of $P_{\text{PD},m}$ on θ is neglected. Hence, only the *overlap power term* depends on the tilt angle θ .

$$P_{\text{PD},r} = \frac{1}{2Z} \int_{S_{\text{PD}}} dx dy |\vec{E}_r(\vec{x})|^2 \quad (31)$$

$$P_{\text{PD},m} = \frac{1}{2Z} \int_{S_{\text{PD}}} dx dy |\vec{E}_m(\vec{x}, \theta)|^2 \quad (32)$$

$$P_{\text{PD},\text{ifm}}(\theta) = \frac{1}{2Z} \int_{S_{\text{PD}}} dx dy \vec{E}_r(\vec{x}) \cdot \vec{E}_m^*(\vec{x}, \theta) \quad (33)$$

The power measured by the PD can hence be written as

$$P_{\text{PD}}(\theta) = P_{\text{PD},r} + P_{\text{PD},m} + 2 \text{Re} [P_{\text{PD},\text{ifm}}(\theta)]. \quad (34)$$

The HE and *heterodyne phase shift* $\sqrt{\eta_{\text{het}}}(\theta)$, $\psi_{\text{het}}(\theta) \in \mathbb{R}$ of two interfering beams are defined in this paper as

$$\sqrt{\eta_{\text{het}}}(\theta) e^{i\psi_{\text{het}}(\theta)} = \frac{P_{\text{PD},\text{ifm}}(\theta)}{\sqrt{P_{\text{PD},r}} \sqrt{P_{\text{PD},m}}}. \quad (35)$$

These are two purely geometrical quantities, which are independent of the beams' powers. In particular, the HE is limited in the range $0 \leq \sqrt{\eta_{\text{het}}}(\theta) \leq 1$, while for the heterodyne phase shift it must hold $0 \leq \psi_{\text{het}}(\theta) < 2\pi$. The HE quantifies the overlap of the two beams, and hence the "quality" of the interference. It should not be confused with the *visibility*, or *contrast*, [25], which is often used in homodyne interferometry.

$$V = \frac{P_{\text{PD},\text{max}} - P_{\text{PD},\text{min}}}{P_{\text{PD},\text{max}} + P_{\text{PD},\text{min}}}, \quad (36)$$

which is instead beam-power-dependent. The power in eq. (34) can finally be rewritten as

$$P_{\text{PD}}(\theta) = P_{\text{PD},r} + P_{\text{PD},m} + 2 \sqrt{\eta_{\text{het}}}(\theta) \times \sqrt{P_{\text{PD},r} P_{\text{PD},m}} \cos(2\pi f_{\text{het}} t + \psi_{\text{het}}(\theta)). \quad (37)$$

to show its dependence on the HE, and where in the argument of the cosine the $f_{\text{het}} t$, $f_{\text{het}} = \frac{1}{2\pi}(\omega_r - \omega_m)$ term was added to describe the heterodyne interference, which is the case in LISA where $f_{\text{het}} \in [5 - 25]$ MHz. The visibility in eq. (36) can hence be re-written as

$$V = \frac{4 \sqrt{\eta_{\text{het}}}(\theta) \sqrt{P_{\text{PD},r} P_{\text{PD},m}}}{P_{\text{PD},r} + P_{\text{PD},m}}. \quad (38)$$

In eq. (37), the $P_{\text{PD},r}$ and $P_{\text{PD},m}$ terms are usually called *DC powers*. The remaining term is called the *beat note*, and is the signal encoding the differential path length variation caused by gravitational waves.

While the angle-dependent heterodyne phase shift $\psi_{\text{het}}(\theta)$ is responsible for non-geometric TTL (NG-TTL) in this specific case of rotations about the QPD's center, the angular dependence of the HE is responsible for variations of the signal's amplitude. This induces variations of the SNR, defined as [40]:

$$\text{SNR} = \frac{\text{Signal RMS}}{\text{Noise ASD}}, \quad (39)$$

where, shortly, "Signal RMS" is the signal's amplitude and "Noise ASD" is the noise level. We refer to subsection 6.1 for further detail on eq. (39). Since the noise level does not depend on the beam alignment, while the signal's amplitude does, this mechanism leads to a tilt-dependent coupling of additive interferometric readout noise, distinct from TTL, where a real path length variation occurs. As beam tilts are going to be present in LISA, this article is focused on understanding how these affect the HE and, therefore, how they also affect LISA's interferometric readout noise, i.e. the readout noise of the QPD signals, both LPS and DWS. Even though LISA only employs QPDs, for completeness, this phenomenon is also analyzed on SEPDs, as these are an extremely valid example to show additional features that arise by segmenting the detector's active area.

3.2 Two Gaussian Beams on an Infinite SEPD

We now derive the HE as a function of the beam tilt angle for an infinite SEPD. This result can be obtained exactly. In order to calculate the HE defined in eq. (35), one has to first calculate the two individual beam powers $P_{\text{PD}, r/m}$ as defined in eq. (12). As the area of the SEPD is infinite, the SEPD detects the totality of each beam's power, hence $P_{\text{PD}, r/m} = P_{0, r/m}$. By integrating the simplified beam intensity in eq. (24) over the SEPD's active area, one gets the infinite SEPD overlap power:

$$\begin{aligned} P_{\text{SEPD}, \infty}(\theta) &= \int_{-\infty}^{+\infty} dx \int_{-\infty}^{+\infty} dy I_{\text{smp}}(x, y, \theta) \\ &= \frac{w_{\text{eff}}^2}{1 - i\rho} \exp\left(-\frac{k^2 w_{\text{eff}}^2 \theta^2}{8(1 - i\rho)}\right). \end{aligned} \quad (40)$$

Noting that $\frac{w_{\text{eff}}^2}{w_m w_r} = \frac{2w_r w_m}{w_r^2 + w_m^2}$, when taking the ratio in eq. (35), this leads to the HE and heterodyne phase for an infinite SEPD of

$$\begin{aligned} \sqrt{\eta_{\text{het}, \text{SEPD}, \infty}}(\theta) &= \frac{1}{\sqrt{1 + \rho^2}} \frac{2w_r w_m}{w_r^2 + w_m^2} \times \\ &\quad \times \exp\left(-\frac{k^2 w_{\text{eff}}^2 \theta^2}{8(1 + \rho^2)}\right), \end{aligned} \quad (41)$$

$$\psi_{\text{het}, \text{SEPD}, \infty}(\theta) = \arctan(\rho) - \underbrace{\rho \frac{k^2 w_{\text{eff}}^2 \theta^2}{8(1 + \rho^2)}}_{\text{NG-TTL}}. \quad (42)$$

Note that eqs. (41) and (42) depend on θ , w_{eff} and k only through their product $\Theta = k w_{\text{eff}} \theta$, meaning that the result for specific values of k and w_{eff} can be carried over to different values by an appropriate rescaling of the angle θ . Also note that eq. (41) is even in both θ and ρ , respecting the previously mentioned symmetries under beam-swap. Equation (42), instead, depends on the sign of ρ , as to be expected for a differential phase. It is hence maximum at $\theta = 0$, where

$$\sqrt{\eta_{\text{het}, \text{SEPD}, \infty}}(\theta = 0) = \frac{1}{\sqrt{1 + \rho^2}} \frac{2w_r w_m}{w_r^2 + w_m^2}, \quad (43)$$

$$\psi_{\text{het}, \text{SEPD}, \infty}(\theta = 0) = \arctan \rho. \quad (44)$$

Lastly, note that the second term in eq. (42) is responsible for the NG-TTL, as it generates a tilt varying phase corresponding to no real path length variation; such term vanishes in the case of perfect beam mode-match. The HE at $\theta = 0$ is equal to one only in the case of perfect mode match, defined by $w_r = w_m$ and $\rho = 0$, and no tilt. In all other cases, the HE degrades. Figure 7 plots the HE as a function of the beam tilt on an infinite SEPD in eq. (41) for some specific values of ρ .

What can be concluded from Figure 7 is that the phase readout noise from a SEPD strongly depends on the beam's alignment. The presence of large beam tilts reduces the overlap between the beams and, consequently, the amplitude of the interferometric signal. Such a signal, hence, results in a lower SNR, as it is compared against noises which are unaffected by the tilt. The additional presence of wavefront curvature mismatch exacerbates the SNR loss at null tilt angles, while it moderately improves the HE at larger tilts.

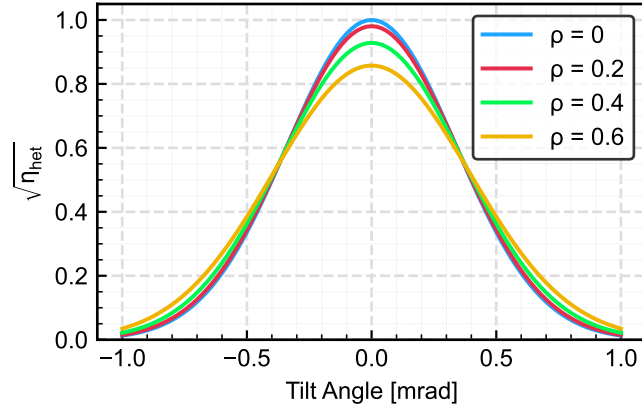


Figure 7: HE on a SEPD as a function of the measurement beam's tilt angle for two same spot-radius beams resulting in $w_r = w_m = w_{\text{eff}} = 1$ mm, $\lambda = 1064$ nm, plotted for four different values of the effective-spot-radius-normalized relative wavefront curvature mismatch parameter ρ . The plotted curves are derived from eq. (41). The presence of wavefront curvature mismatch on one side strongly reduces the maximum achievable HE. On the other side, it mildly broadens the angular range of the interferometric signals (LPS and DWS). The expected value of w_{eff} in the LISA interferometers is ~ 400 μm [26, Table III], giving an angular range of ~ 1.5 mrad where the HE stays above the value of 0.5 (not shown in this plot).

3.3 Two Gaussian Beams on an Infinite QPD

We now derive the HE as a function of the beam tilt angle for the individual segments of an infinite QPD, assumed for simplicity to be slit-less. This case is the first step toward a description of the TMI in LISA; it captures most of the features but misses some implications due to the comparable sizes of QPD and the beam.

This result differs from that on a SEPD, as the integration domain is halved. We further stress that a) adding the individual QPD voltages and b) adding the phase readout from the individual QPD segments, as LISA's architecture does, leads to structurally different results; The first case yields a SEPD of equivalent size, hence featuring the same HE. The second case cannot be — at least directly — related to an equivalent size SEPD.

This result can also be obtained exactly. Due to the system's symmetry, we can simplify the QPD calculation by dividing it into just two sections: a top part and a bottom part of the QPD. This is because the two top segments are unchanged by the symmetry $x \rightarrow -x$, and similarly for the two bottom segments. Therefore, we only need to derive one equation for the top segments and one for the bottom segments, streamlining the overall calculation by avoiding the need to analyze all four segments individually. As a first step, we calculate the individual beam powers impinging on each QPD half. This is simply half of the total power, or $P_{\text{PD}, r/m} = \frac{1}{2}P_{0, r/m}$. As a second step, we integrate the simplified beam intensity in eq. (24) over the QPD's top and bottom segments' active area, one gets the infinite QPD-half overlap powers:

$$\begin{aligned}
 P_{\text{QPD, top}, \infty}(\theta) &= \int_{-\infty}^{+\infty} dx \int_0^{+\infty} dy I_{\text{smp}}(x, y, \theta) \\
 &= \frac{w_{\text{eff}}^2}{2(1-i\rho)} \left(1 - i \operatorname{erfi} \left(\frac{k w_{\text{eff}} \theta}{2^{\frac{3}{2}} \sqrt{1-i\rho}} \right) \right) \times \\
 &\quad \times \exp \left(-\frac{k^2 w_{\text{eff}}^2 \theta^2}{8(1-i\rho)} \right)
 \end{aligned} \tag{45}$$

$$\begin{aligned}
 P_{\text{QPD, btm}, \infty}(\theta) &= \int_{-\infty}^{+\infty} dx \int_{-\infty}^0 dy I_{\text{smp}}(x, y, \theta) \\
 &= \frac{w_{\text{eff}}^2}{2(1-i\rho)} \left(1 + i \operatorname{erfi} \left(\frac{k w_{\text{eff}} \theta}{2^{\frac{3}{2}} \sqrt{1-i\rho}} \right) \right) \times \\
 &\quad \times \exp \left(-\frac{k^2 w_{\text{eff}}^2 \theta^2}{8(1-i\rho)} \right) \\
 &= P_{\text{QPD, top}, \infty}(-\theta)
 \end{aligned} \tag{46}$$

Note that, also here, eqs. (45) and (46) only depend on θ , w_{eff} and k only through their product $\Theta = k w_{\text{eff}} \theta$. These two eqs. (45) and (46) only differ for the sign of the *imaginary error function* $\operatorname{erfi}(x)$ term. Since $\operatorname{erfi}(x)$ is an odd function, $P_{\text{QPD, top}, \infty}(\theta) = P_{\text{QPD, btm}, \infty}(-\theta)$.

From eqs. (45) and (46), it is possible to recover an exact equation for the HE and heterodyne phase of an infinite QPD by taking, respectively, the absolute value and the argument. Using the property of the imaginary error function $\operatorname{erfi}(x^*) = \operatorname{erfi}^*(x)$ and calculating the ratio in eq. (35), one gets the HE and heterodyne phase for the top and bottom segments of a QPD, reported in eqs. (47–50) respectively.

$$\sqrt{\eta_{\text{het, QPD, top, } \infty}(\theta)} = \frac{1}{\sqrt{1+\rho^2}} \frac{2w_r w_m}{w_r^2 + w_m^2} \exp\left(-\frac{k^2 w_{\text{eff}}^2 \theta^2}{8(1+\rho^2)}\right) \sqrt{1 + 2 \operatorname{Im} \left[\operatorname{erfi} \left(\frac{k w_{\text{eff}} \theta}{2^{\frac{3}{2}} \sqrt{1-i\rho}} \right) \right] + \left| \operatorname{erfi} \left(\frac{k w_{\text{eff}} \theta}{2^{\frac{3}{2}} \sqrt{1-i\rho}} \right) \right|^2} \quad (47)$$

$$\psi_{\text{het, QPD, top, } \infty}(\theta) = \arctan(\rho) - \rho \frac{k^2 w_{\text{eff}}^2 \theta^2}{8(1+\rho^2)} + \arg \left(1 - i \operatorname{erfi} \left(\frac{k w_{\text{eff}} \theta}{2^{\frac{3}{2}} \sqrt{1-i\rho}} \right) \right) \quad (48)$$

$$\sqrt{\eta_{\text{het, QPD, btm, } \infty}(\theta)} = \frac{1}{\sqrt{1+\rho^2}} \frac{2w_r w_m}{w_r^2 + w_m^2} \exp\left(-\frac{k^2 w_{\text{eff}}^2 \theta^2}{8(1+\rho^2)}\right) \sqrt{1 - 2 \operatorname{Im} \left[\operatorname{erfi} \left(\frac{k w_{\text{eff}} \theta}{2^{\frac{3}{2}} \sqrt{1-i\rho}} \right) \right] + \left| \operatorname{erfi} \left(\frac{k w_{\text{eff}} \theta}{2^{\frac{3}{2}} \sqrt{1-i\rho}} \right) \right|^2} \quad (49)$$

$$\psi_{\text{het, QPD, btm, } \infty}(\theta) = \arctan(\rho) - \rho \frac{k^2 w_{\text{eff}}^2 \theta^2}{8(1+\rho^2)} + \arg \left(1 + i \operatorname{erfi} \left(\frac{k w_{\text{eff}} \theta}{2^{\frac{3}{2}} \sqrt{1-i\rho}} \right) \right) \quad (50)$$

Note that the heterodyne phase in eqs. (48) and (50) contains the same NG-TTL term in eq. (42); they also contain a further term, which leads to the DWS signal described in [26, eqs. (38, 39)]. Also note that, when calculating the AP-LPS defined in eq. (5), measuring the interference with a QPD instead of a SEPD gives an extra QPD-AP term, leading to additional NG-TTL with respect to a SEPD. This can be seen by taking the average of eqs. (48) and (50), shown in eq. (51). This term also vanishes in the case of perfectly matched GBs, as found also numerically in [35, Figure 12] in the case of square QPDs. Also, using the LPF-LPS definition would cancel out this extra term.

$$\psi_{\text{het, QPD, AP, } \infty}(\theta) = \underbrace{\arctan(\rho) - \rho \frac{k^2 w_{\text{eff}}^2 \theta^2}{8(1+\rho^2)}}_{\text{SEPD}} + \underbrace{\frac{1}{2} \arg \left(1 + \operatorname{erfi}^2 \left(\frac{k w_{\text{eff}} \theta}{2^{\frac{3}{2}} \sqrt{1-i\rho}} \right) \right)}_{\text{QPD-AP term}} \quad (51)$$

Analogous expressions can be derived in the case of a horizontal tilt, with the correspondences

$$\sqrt{\eta_{\text{het, QPD, top, } \infty}(\theta)} \Leftrightarrow \sqrt{\eta_{\text{het, QPD, left, } \infty}(\theta)} \quad (52)$$

$$\sqrt{\eta_{\text{het, QPD, btm, } \infty}(\theta)} \Leftrightarrow \sqrt{\eta_{\text{het, QPD, right, } \infty}(\theta)} \quad (53)$$

These two equations, as well as eqs. (47) and (49), only differ for the sign of the $\operatorname{Im}[\operatorname{erfi}(\cdot)]$ term, due to the fact that $\operatorname{erfi}(x)$ is an odd function. Note that, also including the DWS signal in [26], this is the first QPD function to depend on the sign of ρ . As previously argued, the substitution $\rho \rightarrow -\rho$ is in fact equivalent to $\theta \rightarrow -\theta$, as this corresponds to swapping the two beams in the linear framework. This respects the fact that both θ and ρ change signs under beam-swap. In case of perfect beam mode-match $\rho = 0$, eqs. (47–50) take the simpler, and same in the case of the HE, form

$$\sqrt{\eta_{\text{het, QPD, } \infty}(\theta)} = \frac{2w_r w_m}{w_r^2 + w_m^2} \sqrt{1 + \operatorname{erfi}^2 \left(\frac{k w_{\text{eff}} \theta}{2^{\frac{3}{2}}} \right)} \times \exp\left(-\frac{k^2 w_{\text{eff}}^2 \theta^2}{8}\right), \quad (54)$$

$$\psi_{\text{het, QPD, } \infty}(\theta) = \arg \left(1 \pm i \operatorname{erfi} \left(\frac{k w_{\text{eff}} \theta}{2^{\frac{3}{2}}} \right) \right), \quad (55)$$

where in eq. (55) the + is to be taken for the top segments, while the - for the bottom ones, and we remind that $\operatorname{erfi}(x) \in \mathbb{R} \forall x \in \mathbb{R}$.

The resulting HE for the top segments of an infinite QPD in eq. (47) is plotted in Figure 8 for a few values of ρ . What can be concluded from this Figure is, similarly to the SEPD case in Figure 7, that the phase readout noise from a QPD-segment strongly depends on the beam's alignment. The consequent decrease in SNR affects all QPD signals, meaning both LPS and DWS. The reduction in DWS sensitivity is not to be confused with what is presented in [26, Figure 7], where the only cause is the reduction of DWS response; the result derived in this subsection concerns only the segment's signal amplitude, which is the main driver of the readout phase noise. These two noise contributions, in fact, add up, as later derived in Section 7.

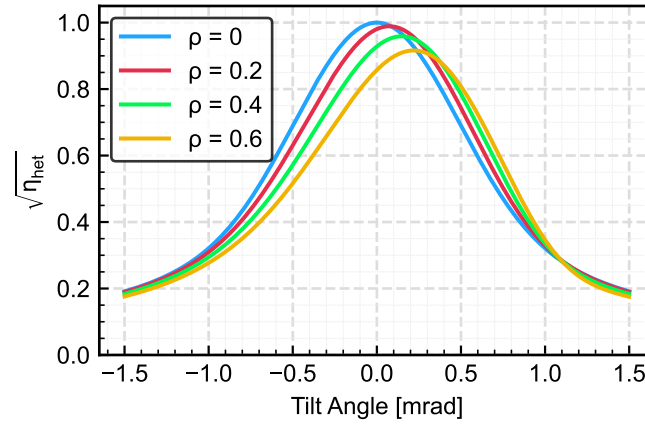


Figure 8: Plot of the HE of the top segments of an infinite QPD as a function of the measurement beam's tilt angle for two same spot-radius beams resulting in $w_r = w_m = w_{\text{eff}} = 1$ mm, $\lambda = 1064$ nm, plotted for four different values of the effective-spot-radius-normalized relative wavefront curvature mismatch parameter ρ . The plotted curves are derived analytically from eq. (47). If eq. (49) was used, the same effect would happen, but in the opposite angle. If negative values of ρ were used, the HE's peak would shift into the opposite direction. The presence of wavefront curvature mismatch not only strongly reduces the maximum achievable HE but also shifts the angle at which the HE peaks. Furthermore, asymmetry of the plot increases with ρ . An intuitive explanation of this phenomenon is given in Figure 11.

A key difference in the HE of an infinite SEPD segment and that of an infinite QPD is that the former always peaks at $\theta = 0$, while the latter peaks at $\theta = 0$ only if $\rho = 0$. In other words, in the case of perfect beam mode-match, the HE is maximum at zero tilt; otherwise, the peak angle is not zero, and its exact value depends on ρ ; in particular, it must be an odd function of ρ . This is intuitive, but not straightforward, when looking at eqs. (47) and (49). It can, however, be made evident, for instance, by taking a Maclaurin expansion. For instance, expanding eq. (47) to second-order in both ρ and θ leads to eq. (56).

$$\sqrt{\eta_{\text{het, QPD, top, } \infty}}(\theta) = \frac{2w_r w_m}{w_r^2 + w_m^2} \left(\sqrt{1 - \rho^2} + kw_{\text{eff}} \frac{\rho}{\sqrt{2\pi}} \theta - (kw_{\text{eff}})^2 \left(\frac{2\pi - 4 - (3\pi - 5)\rho^2}{16\pi} \right) \theta^2 \right) + \mathcal{O}(\rho^3, \theta^3). \quad (56)$$

In this series, the odd terms in θ are not zero. With this second-order series, one can easily find the value of θ at which the maximum of $\sqrt{\eta_{\text{het, QPD, top, } \infty}}$ is reached:

$$\theta_{\text{max, QPD, top}} \approx \frac{\sqrt{2\pi}\rho}{(kw_{\text{eff}})(2\pi - 4 - (3\pi - 5)\rho^2)}. \quad (57)$$

Dually, the tilt angle at which $\sqrt{\eta_{\text{het, QPD, btm, } \infty}}(\theta)$ is maximum is $\theta_{\text{max, QPD, btm}} = -\theta_{\text{max, QPD, top}}$. Last, for symmetry reasons, and according to eqs. (47) and (49), it holds

$$\sqrt{\eta_{\text{het, QPD, top, } \infty}}(\theta = 0) = \sqrt{\eta_{\text{het, QPD, btm, } \infty}}(\theta = 0). \quad (58)$$

As evident from eq. (57), this phenomenon is caused by the presence of wavefront curvature mismatch, combined with the fact that the QPD's active area is not symmetric around the measurement beam's tilt pivot, as it was in the case of an infinite SEPD. A geometrical interpretation of it is depicted in Figure 11. The presence of a wavefront curvature mismatch breaks the QPD-segment symmetry of tilts, hence leading top and bottom segments of a QPD to be illuminated by different intensities.

The determination of the peak angle of eqs. (47) and (49) as a function of ρ is possible only numerically. Figure 9 plots the values of $\theta_{\text{max, QPD, top}}$ as a function of ρ , together with the peak value of the HE $\sqrt{\eta_{\text{het, QPD, top, } \infty}}(\theta = \theta_{\text{max, QPD, top}})$.

By adding the powers measured by the top and bottom halves of an infinite QPD, one gets the total beam power impinging on the QPD. This principle can be used to define the HE of the QPD as a whole, resembling LISA's architecture, where the phase measurements from the individual QPD segments are combined in post-processing. We name this quantity whole-QPD HE $\sqrt{\eta_{\text{het, vQPD, } \infty}}(\theta)$. This can be calculated by adding up the two eqs. (47) and (49) and dividing the result by two, as done in eq. (59). This result, once more, would be of difficult analytic interpretation, while it's more intuitive to take a look at its second-order Maclaurin expansion in both θ and ρ as reported in eq. (60). This can be compared with the analogous second-order Maclaurin expansion of the HE on an infinite SEPD in eq. (41), reported in eq. (61). It is important to stress that this quantity differs from the HE of a SEPD. While it must, for symmetry reasons, be an even function and hence peak at $\theta = 0$, it degrades significantly slower as a function of the tilt angle. This

can mathematically be seen by comparing the quadratic terms in eq. (60) and eq. (61). The quadratic term of eq. (60) is always smaller than that of eq. (61), indicating that the name whole-QPD HE is less affected by beam tilts than the HE of SEPD. The reason why the whole-QPD HE decreases slower as a function of the beam tilt angle can be intuitively understood from Figure 11: in the presence of a beam tilt, a local phase offset builds up between the wavefronts of the interfering beams. Such local phase offset is monotonically related to the distance from the PD's center. Its presence reduces the constructiveness of the interference pattern of the two beams over the detector; such a pattern is integrated by the PD, which hence outputs a beat note with smaller amplitude. The full plot of the two heterodyne efficiencies is shown in Figure 10.

This article is, to our knowledge, the first to acknowledge this wavefront-curvature mismatch-driven feature of the beam overlap in the presence of tilts around the centre of a QPD. This has further implications in the QPD signals noise which are discussed in Section 6.

$$\sqrt{\eta_{\text{het}, \forall \text{QPD}, \infty}(\theta)} = \frac{1}{2} \left(\sqrt{\eta_{\text{het}, \text{QPD}, \text{top}, \infty}(\theta)} + \sqrt{\eta_{\text{het}, \text{QPD}, \text{btm}, \infty}(\theta)} \right) \quad (59)$$

$$\approx \frac{2w_r w_m}{w_r^2 + w_m^2} \left(\sqrt{1 - \rho^2} + \frac{(kw_{\text{eff}})^2 (4 - 5\rho^2 + \pi(-2 + 3\rho^2))}{16\pi} \theta^2 \right) + \mathcal{O}(\rho^3, \theta^3) \quad (60)$$

$$\sqrt{\eta_{\text{het}, \text{SEPD}, \infty}(\theta)} \approx \frac{2w_r w_m}{w_r^2 + w_m^2} \left(\frac{1}{\sqrt{1 + \rho^2}} - \frac{(kw_{\text{eff}})^2}{4(1 + \rho^2)^{\frac{3}{2}}} \theta^2 \right) + \mathcal{O}(\theta^3) \quad (61)$$

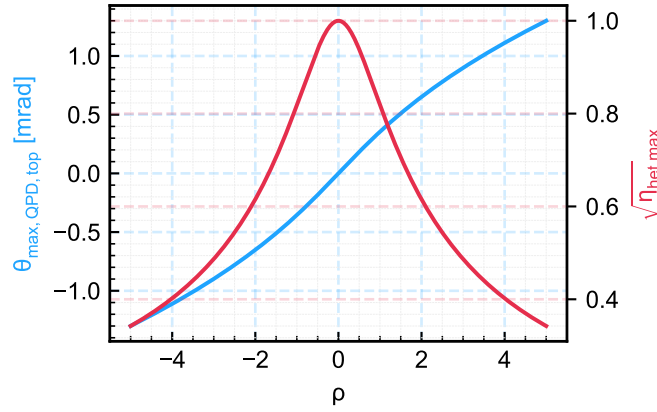


Figure 9: Plot of the peak angle $\theta_{\text{max}, \text{QPD}, \text{top}}(\rho)$, defined as the angle at which the HE for a given value of ρ $\sqrt{\eta_{\text{het}, \text{QPD}, \text{top}, \infty}(\theta)}$ is maximum, and of the HE evaluated at $\theta_{\text{max}, \text{QPD}, \text{top}}$, for two interfering beams with $w_r = w_m = w_{\text{eff}} = 1$ mm. These are two non-linear functions of the effective-spot-radius-normalized relative wavefront curvature mismatch parameter ρ , which must be, respectively, even and odd. One can see that the presence of a wavefront curvature mismatch always degrades the maximum reachable HE.

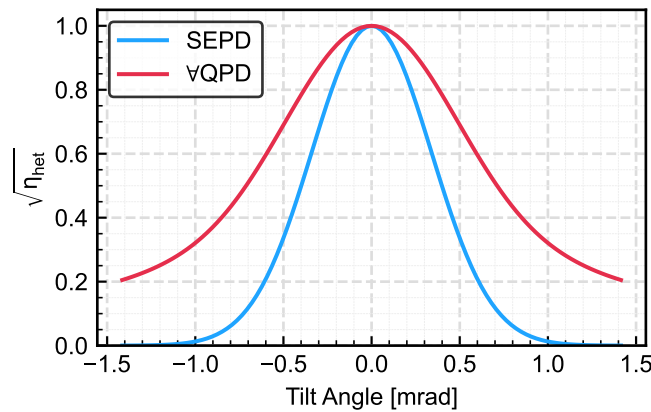


Figure 10: Plot of the HE for an infinite SEPD in eq. (41) and the whole-QPD HE for an infinite QPD (calculated numerically, approximated in eq. (60)). The used beam parameters are $w_{\text{eff}} = w_r = w_m = 1$ mm and $\rho = 0$. The HE for a SEPD degrades noticeably quicker as a function of the beam tilt than the whole-QPD HE.

We furthermore stress that in LISA's architecture, where the phase of each QPD-segment is extracted separately and the phase combinations are extracted afterwards, that the SEPD HE is physically inaccessible, as it cannot be measured. On the other hand, the whole-QPD HE is the relevant parameter to describe the HE of such a system.

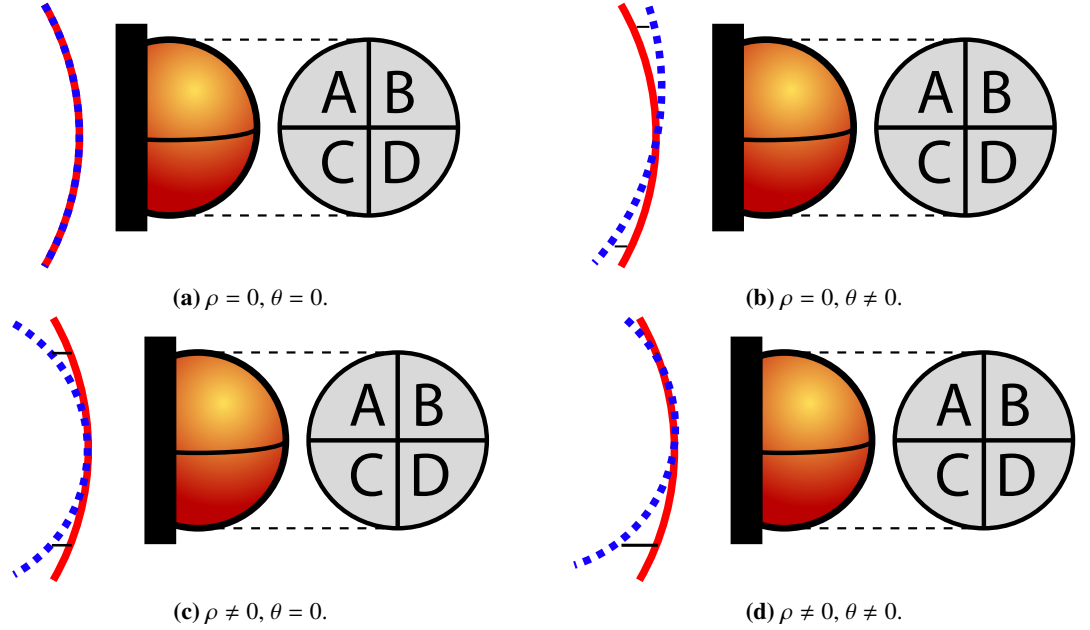


Figure 11: Geometric interpretation of the shift in the HE's maximum angle on a QPD. The principle followed in this explanation can be found also in [35, Figure 2]. The four figures represent four situations where the wavefronts of a reference beam (red) and of a measurement beam (blue) impinge on a QPD. The black lines indicatively represent the wavefront curvature mismatch. The measurement beam is free to rotate around the center of the QPD's surface, hence so does its wavefront. In subfigure 11a, there is no wavefront curvature mismatch, and the beams are parallel. In this situation, the two beams have the same local phase difference $\phi_{\text{off}}(y)$ at every point of the QPD's surface, which we parametrize only with y as there is no dependence on x due to translational symmetry; as this argument is independent of the absolute phase difference, we can say $\phi_{\text{off}}(y) = 0, \forall y$. This results in coherent interference of the two beams in the totality of the QPD surface, and hence maximizes the HE. In subfigure 11b, there is no wavefront curvature mismatch, but a beam tilt is present. Due to the tilt, the wavefronts of the two beams manifest a y -coordinate dependent phase offset, given by the tilt term in eq. (19). Setting for simplicity $\phi_{\text{off}}(y=0) = 0$, this is $\phi_{\text{off}}(y) = ky \propto |y|$. The presence of this phase offset inhibits constructive interference over the whole QPD, hence decreasing the HE. This effect is independent of the sign of $\phi_{\text{off}}(y)$, hence the measured HE is the same on both halves of the QPD. In subfigure 11c, a wavefront curvature mismatch is present, and the beams are parallel. Due to the mismatch, the wavefronts of the two beams are in phase only at $y = 0$, while in all other points of the QPD a wavefront mismatch proportional to the absolute value of the distance to the QPD's center arises, or $\phi_{\text{off}}(y)$. Such a phase offset is an even function of y ; in fact, in this case the resulting DWS signal is zero. This leads to a similar situation as in subfigure 11b: the HE degrades symmetrically in the two QPD halves. In subfigure 11d, both a wavefront curvature mismatch and a tilt are present. In comparison to subfigure 11c, the tilt has reduced the phase offset on the top segments, while on the other hand, the phase offset is increased in the bottom segments. The local intensity and the measured power are hence increased in the top segments, and decreased in the bottom ones. The presence of a wavefront curvature mismatch, hence, breaks the tilting symmetry, and the top segments manifest a higher HE than the bottom segments: this is exactly what Figure 8 shows. Looking only at subfigures 11b and 11d, one can also see why a beam curvature mismatch results in a varying heterodyne phase on a SEPD.

3.4 Top-Hat - Gaussian Beam on an Infinite PD

This subsection addresses the calculation of the heterodyne interference of a GB with a tilting TH beam; this case is a first step towards the description of the SCI in LISA. This result cannot be obtained by approximating the measurement beam's waist value to infinity, as it was performed in [26] for the calculation of the DWS signal of a TH beam and a GB, as this would make the TH beam's power diverge. Instead, this requires a proper modelling of the TH beam to obtain its total power.

In this subsection, the tilting GB, i.e. the measurement beam defined in eqs. (9) and (10), is replaced by a TH beam, defined as

$$\vec{E}(\vec{x})_{\text{TH}} = \begin{cases} \text{Re} [\hat{\epsilon}_m E_{\text{TH}} e^{ikz}] & x^2 + y^2 \leq r_{\text{TH}}^2 \\ 0 & \text{elsewhere} \end{cases} \quad (62)$$

in its coordinate frame. The tilts of the TH beam are obtained by rotating the vector field using eq. (16). This

gives the same result as of eq. (17) for the polarization unitary vector, while the TH beam gains the tilt term $e^{ik\theta y}$. The electric field in eq. (62), hence, becomes

$$\vec{E}(\vec{x})_{\text{TH}} = \text{Re} \left[\hat{\epsilon}_m E_{\text{TH}} e^{ik\theta y + ikz} \right] \quad (63)$$

when different from zero. We neglect variations of the boundary conditions in eq. (62) due to the tilt, as these are second-order in θ . The intensity of the plane wave is

$$I(\vec{x})_{\text{TH}} = \begin{cases} \frac{1}{2Z} |E_{\text{TH}}|^2 = I_{\text{TH}} & x^2 + y^2 \leq r_{\text{TH}}^2 \\ 0 & \text{elsewhere} \end{cases} \quad (64)$$

Note that eq. (64) is independent of the z coordinate. The integration of this intensity on an infinite SEPD results in the total TH beam's power

$$P_{\text{TH}} = I_{\text{TH}} \pi r_{\text{TH}}^2. \quad (65)$$

The overlap of the TH beam and of the GB behaves as the overlap of two GBs, of which one has an asymptotically infinite spot size. Assuming $w_{m,0} = \infty$, this results in $w_{\text{eff}} = \sqrt{2}w_r(z)$, $R_{\text{rel}} = R_r(z)$ and $\rho = \frac{kw_r(z)^2}{2R_r(z)} = \frac{z}{z_{R,r}}$. Therefore, the same simplified expression for the overlap intensity term in eq. (24) can be used to describe the main geometrical dependencies of this configuration. To recover the full beam intensity, however, eq. (66) has to be used

$$\text{GB-TH: } I_{\text{ifm}}(x, y, \theta) = I_r + I_{\text{TH}} + C e^{i\Psi} \left(I_{\text{smp}}(x, y, \theta) + c.c. \right), \quad (66)$$

which relies on eqs. (26) and (64) as well as on the quantities C and Ψ :

$$C = \hat{\epsilon}_r \cdot \hat{\epsilon}_m \sqrt{I_{r,0} I_{\text{TH}}} \left(\frac{w_{r,0}}{w_r(z_r)} \right) \sqrt{\frac{\pi}{2}} \quad (67)$$

$$\Psi = kz_r + \eta(z_r) - kz_m. \quad (68)$$

An important remark is that, within this framework, when evaluating the integral of eq. (66), the constraint set by the finite radius of the TH beam is mathematically equivalent to that set by the size of the PD — which is assumed to be infinite in this subsection. To reasonably assume that the PD's size is infinite, and hence to integrate eq. (24) on an infinite PD surface, it must hold $r_{\text{TH}} \sim r_{\text{PD}} \gg w_r(z_r)$. With these assumptions, the resulting overlap powers on a SEPD and the top segments of a QPD are again described by eqs. (40) and (45), respectively. However, the resulting HE differs in the normalization, as the expression for the TH beam's power, which appears in the denominator of eq. (35), has changed. The resulting expression includes the quantity $w_r(1 + \rho^2)^{-\frac{1}{2}}$. However, due to the simplified expression of the parameter ρ in this specific case, one can check that this results simply in $w_{0,r}$. The resulting HE on a SEPD and the top segments of a QPD are reported as a function of the GB's spot size in eqs. (69) and (70). The result for the bottom segments of a QPD can be obtained by switching the sign of θ in eq. (70). Note that equation eq. (69) depends only on the waist size of the GB $w_{0,r}$, and not on its spot size. It also does not depend on the wavefront curvature mismatch, as it is independent of ρ . On the other hand, eq. (70) depends on w_r and ρ only in the square root. Regarding the heterodyne phase, there is no variation for the heterodyne phase with respect to that of a GB-GB interference, and this case is still described with eqs. (42) and (48).

$$\sqrt{\eta_{\text{het, SEPD, } \infty}}(\theta) = \frac{\sqrt{2}w_{0,r}}{r_{\text{TH}}} \exp\left(-\frac{k^2 w_{0,r}^2 \theta^2}{4}\right) \quad (69)$$

$$\sqrt{\eta_{\text{het, QPD, top, } \infty}}(\theta) = \frac{\sqrt{2}w_{0,r}}{r_{\text{TH}}} \exp\left(-\frac{k^2 w_{0,r}^2 \theta^2}{4}\right) \sqrt{1 + 2 \text{Im} \left[\text{erfi} \left(\frac{kw_r \theta}{2\sqrt{1-i\rho}} \right) \right] + \left| \text{erfi} \left(\frac{kw_r \theta}{2\sqrt{1-i\rho}} \right) \right|^2} \quad (70)$$

This result is, however, of little use, as it is valid only for $r_{\text{TH}} \gg w_r(z_r)$, and hence $\sqrt{\eta_{\text{het, PD, } \infty}}(\theta)$ tends to zero. Note also that, for $w_{0,r} > r_{\text{PD}}/\sqrt{2}$, eqs. (42) and (48) give an unphysical result. As the interesting cases are those with $r_{\text{th}} \sim r_{\text{PD}}$, the GB-TH interference requires, hence, a finite QPD modelling.

3.5 Two Gaussian Beams on an Finite SEPD

We now derive the HE as a function of the beam tilt angle for a finite SEPD. This result can be obtained exactly only for $\theta = 0$; such a condition is useful to calculate as a reference. As a first step for this derivation, we calculate the beam power impinging on the SEPD to be derived. This is no longer in the total power of

the beam, but a fraction of it, given by eq. (71), and depends on the ratio between the QPD's radius, r_{QPD} , and the beam's spot radius.

$$P_{\text{SEPD}, \circ, r/m} = P_{0, r/m} \left(1 - \exp \left(-2 \frac{r_{\text{QPD}}^2}{w_{r/m}^2(z_{r/m})} \right) \right) \quad (71)$$

Integrating eq. (24) on a finite circle or radius r_{QPD} gives

$$\begin{aligned} P_{\text{SEPD}, \circ}(\theta = 0) &= \int_0^{r_{\text{QPD}}} r \, dr \int_0^{2\pi} d\phi I_{\text{smp}}(x, y, \theta = 0) \\ &= \frac{w_{\text{eff}}^2}{1 - i\rho} \left(1 - e^{-\beta^2(1-i\rho)} \right). \end{aligned} \quad (72)$$

where we defined $\beta = \sqrt{2}r_{\text{SEPD}}/w_{\text{eff}}$. Calculating the HE and heterodyne phase shift gives

$$\sqrt{\eta_{\text{hetSEPD}, \circ, \theta=0}} = \frac{1}{\sqrt{1 + \rho^2}} \frac{2w_r w_m}{w_r^2 + w_m^2} \frac{1}{\sqrt{1 - \exp(-\beta_r^2)} \sqrt{1 - \exp(-\beta_m^2)}} \sqrt{1 - 2e^{-\beta^2} \cos(\beta^2 \rho) + e^{-2\beta^2}} \quad (73)$$

$$\psi_{\text{het, SEPD}, \circ, \theta=0} = \arctan \rho + \arctan \left(\frac{e^{-\beta^2} \sin(\beta^2 \rho)}{1 - e^{-\beta^2} \cos(\beta^2 \rho)} \right) \quad (74)$$

These two derived quantities tend to eqs. (41) and (42), respectively, in the limit $\beta \rightarrow \infty$. As one can see, both expressions include the oscillatory terms $\cos / \sin(\beta^2 \rho)$. Their impact vanishes in the case of a perfect beam match $\rho = 0$. Otherwise, when not suppressed by the term $e^{-2\beta^2}$; however, so if $\beta \rightarrow 1$, largely different outcomes of $\sqrt{\eta_{\text{hetSEPD}, \circ, \theta=0}}$ and $\psi_{\text{het, SEPD}, \circ, \theta=0}$ may occur for different values of ρ . Note that, due to the cylindrical symmetry specific to the case $\theta = 0$, eqs. (41) and (42) also represent the HE and heterodyne phase shift of a QPD-segment.

We proceed now to derive an expression of the HE as a function of the beam tilt angle. To make the integration possible, we expand in θ of the simplified beam intensity in eq. (24). We hence integrate the overlap intensity term eq. (24) on the finite SEPD. This calculation cannot be done analytically on a finite circular area centered at $(x, y) = (0, 0)$. A way to circumvent this issue is by Maclaurin expanding in the simplified overlap intensity term $I_{\text{smp}}(x, y, \theta)$ the term that prevents the integration of the beam intensity, which is the pathlength term $\exp(ik\theta y)$; this comes at the cost of reducing the angular range of validity of the result. The term $\exp(ik\theta y)$ can hence be expanded in θ , giving an expression which is valid only for small tilts. This procedure is justified, as the tilt range that we aim to describe is indeed small, of the order of a few mrad at most. Conversely, as argued in [26, subsection III B], the finite size of the PD can increase the angular range of validity of the resulting expressions if the SEPD's size is very small, counteracting the shrinking of such range due to the expansion in θ . Note that, for a SEPD, this expansion must be at least second-order in θ , as the integration on the SEPD cancels out the odd powers of y , and hence of θ . This also implies that the resulting expression gains one order in precision in the expansion. The expansion of eq. (24) to the second-order in θ gives eq. (75). The integration can then be performed in polar coordinates for convenience. The finite SEPD overlap power is reported in eq. (76), at second-order.

$$I_{\text{smp}}(x, y, \theta) \approx I_{\text{smp-}\theta 2}(x, y, \theta) = \frac{2}{\pi} \exp \left(-2 \frac{x^2 + y^2}{w_{\text{eff}}^2} (1 - i\rho) \right) \left(1 - ik\theta y - \frac{1}{2} (k\theta y)^2 \right) + \mathcal{O}(k\theta)^3. \quad (75)$$

$$\begin{aligned} P_{\text{SEPD}, \circ}(\theta) &= \int_0^{r_{\text{QPD}}} r \, dr \int_0^{2\pi} d\phi I_{\text{smp-}\theta 2}(r, \phi, \theta) \\ &= \frac{w_{\text{eff}}^2}{8(1 - i\rho)^2} \left(8(1 - i\rho) - k^2 w_{\text{eff}}^2 \theta^2 - e^{-2 \frac{r_{\text{QPD}}^2}{w_{\text{eff}}^2} (1 - i\rho)} \left(8(1 - i\rho) - 2k^2 \theta^2 (r_{\text{QPD}}^2 (1 - i\rho) + w_{\text{eff}}^2) \right) \right) + \mathcal{O}(k\theta)^4 \end{aligned} \quad (76)$$

Note that this procedure is exact in ρ : to calculate the HE from the power term in eq. (76), no expansion in ρ is required, while such expansion was needed for the DWS signal in [26]. This is due to the fact that the integration domain has circular symmetry. From eq. (76), the HE can be derived by taking the absolute value and normalizing by the square root of the beams' powers. The resulting expression is a polynomial, which has the same order as the Maclaurin expansion in eq. (75). We report the resulting HE for a finite SEPD in eq. (147), where we went two orders further and derived it to eighth-order in θ . The parameters $\beta = \sqrt{2}r_{\text{SEPD}}/w_{\text{eff}}$, $\beta_r = \sqrt{2}r_{\text{SEPD}}/w_r$, $\beta_m = \sqrt{2}r_{\text{SEPD}}/w_m$ have been introduced for simplicity. The non-listed t_1 , t_3 , t_5 and t_7 coefficients are zero.

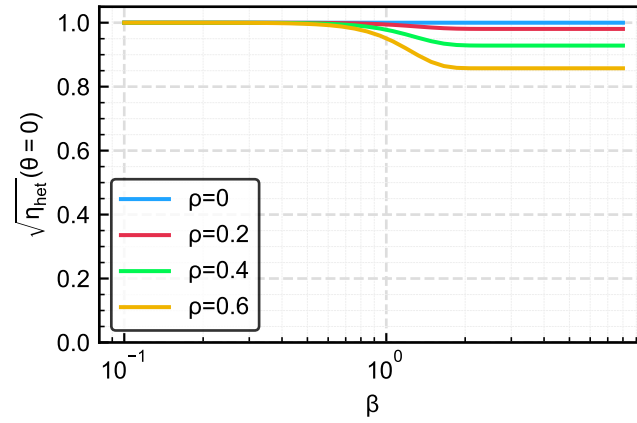
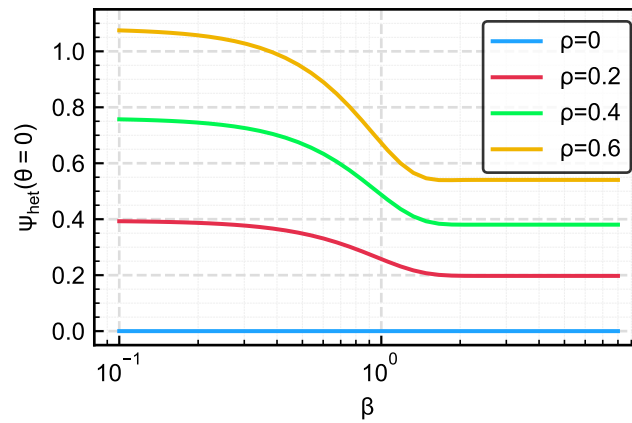
(a) $\sqrt{\eta_{\text{hetSEPD}, \circ, \theta=0}}$ (b) $\psi_{\text{het}, \text{SEPD}, \circ, \theta=0}$

Figure 12: Plot of the HE and heterodyne phase shift for two GBs impinging on a finite SEPD in eqs. (41) and (42). The used beam parameters are $w_{\text{eff}} = w_r = w_m = 1$ mm. Both figures manifest a large variation of the plotted quantity around $\beta \sim 1$.

From eq. (147), new knowledge can be gained regarding the limit of the coefficients t_0 , t_2 and t_4 for small SEPD radii. In this limit, the HE tends to one independently of the tilt and of the wavefront curvature mismatch ρ and tilt angle θ .

$$\lim_{\beta \rightarrow 0} \sqrt{\eta_{\text{het},0}} t_0 = 1 \quad \forall \rho, \theta \quad (77)$$

$$\lim_{\beta \rightarrow 0} \sqrt{\eta_{\text{het},0}} t_2 = 0 \quad \forall \rho, \theta \quad (78)$$

$$\lim_{\beta \rightarrow 0} \sqrt{\eta_{\text{het},0}} t_4 = 0 \quad \forall \rho, \theta \quad (79)$$

$$\lim_{\beta \rightarrow 0} \sqrt{\eta_{\text{het},0}} t_6 = 0 \quad \forall \rho, \theta \quad (80)$$

Numerical simulations (see subsection 3.8 for more details) are used to assess the validity of the approximations for finite SEPD sizes. Figure 13 compares the HE on a finite SEPD of two beams calculated either numerically using the method described in subsection 3.8, or analytically to second-, fourth- and sixth-order using eq. (147). As one can see, the angular range of this method is strongly limited by the order of the used expansion. Figure 14 compares the resulting HE for three values of the β parameter around the value of one. One can see that a small value of β corresponds to a broader main peak in the interference pattern. Figure 15 compares the analytically calculated t_0 , t_2 , t_4 and t_6 coefficients in eq. (147) to the numerically calculated ones for a specific value of ρ . The numerical model confirms the analytically estimated coefficients.

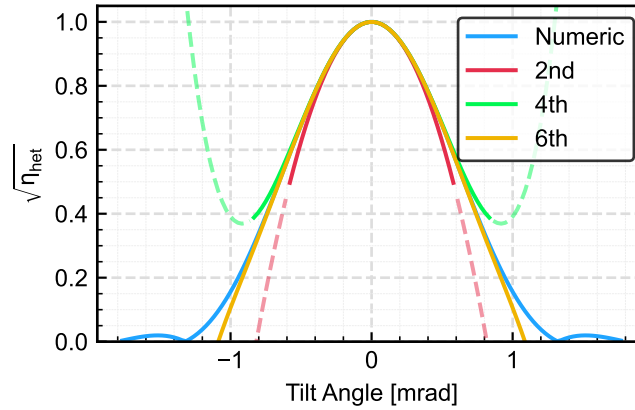


Figure 13: Plot of the HE as a function of the beam tilt calculated for a finite SEPD for the parameters $w_r = w_m = w_{\text{eff}} = 1$ mm, $r_{\text{QPD}} = 1$ mm and $\rho = 0$. The HE is calculated both numerically and analytically at various orders. Only one value of ρ is shown, as this method is exact in ρ . Dashed lines indicate where the analytic value deviates from the numerical result by more than 0.1. Note that, in the numeric curve, diffraction fringes are visible for $|\theta| > 0.75$ mrad. These are related to the sign reversal in the DWS signal observed in [26, Figure 11], which takes place only in finite QPDs.

3.6 Two Gaussian Beams on an Finite QPD

We now derive the HE as a function of the beam tilt angle for a finite QPD. This calculation follows that in Subsection 3.3, where the QPD is assumed slit-less and split into two parts according to the symmetry of the system. This result can, albeit approximated, deliver a full description of the TMI in LISA.

As in the case of the finite SEPD, the simplified overlap intensity term $I_{\text{smpl}}(x, y, \theta)$ is expanded in θ . The QPD is assumed to have no slits for simplicity.

As a first step we calculate the power detected by a QPD half to be half of that in eq. (71).

$$P_{\text{QPD}, \circ, r/m} = \frac{1}{2} P_{0, r/m} \left(1 - \exp \left(-2 \frac{r_{\text{QPD}}^2}{w_{r/m}^2} \right) \right) \quad (81)$$

As a second step, we integrate the expanded overlap intensity term onto a semicircle centered in $(x, y) = (0, 0)$. This calculation is performed in polar coordinates for convenience. Note that, unlike in the case for the finite SEPD, the odd terms in y do not cancel out in the integration process, as the integration domain is not circularly symmetric. The resulting finite QPD overlap power, obtained by integrating

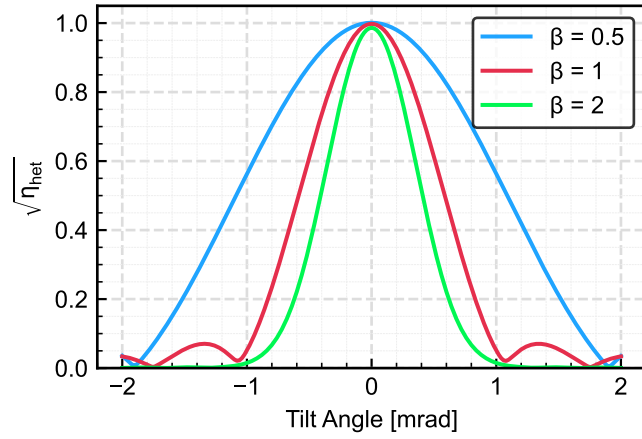


Figure 14: Plot of the HE as a function of the beam tilt numerically calculated for a GB-GB beam pair impinging on a finite SEPD. The beam parameters are $w_r = w_m = w_{\text{eff}} = 1$ mm, $r_{\text{SEPD}} = [0.5, 1, 2]/\sqrt{2}$ mm and $\rho = 0.2$. Note that, in the $\beta = 0.5$ and $\beta = 1$ plots, diffraction fringes are visible outside the main peak. These are the causes of the DWS sign reversal discussed in [26, Figure 11].

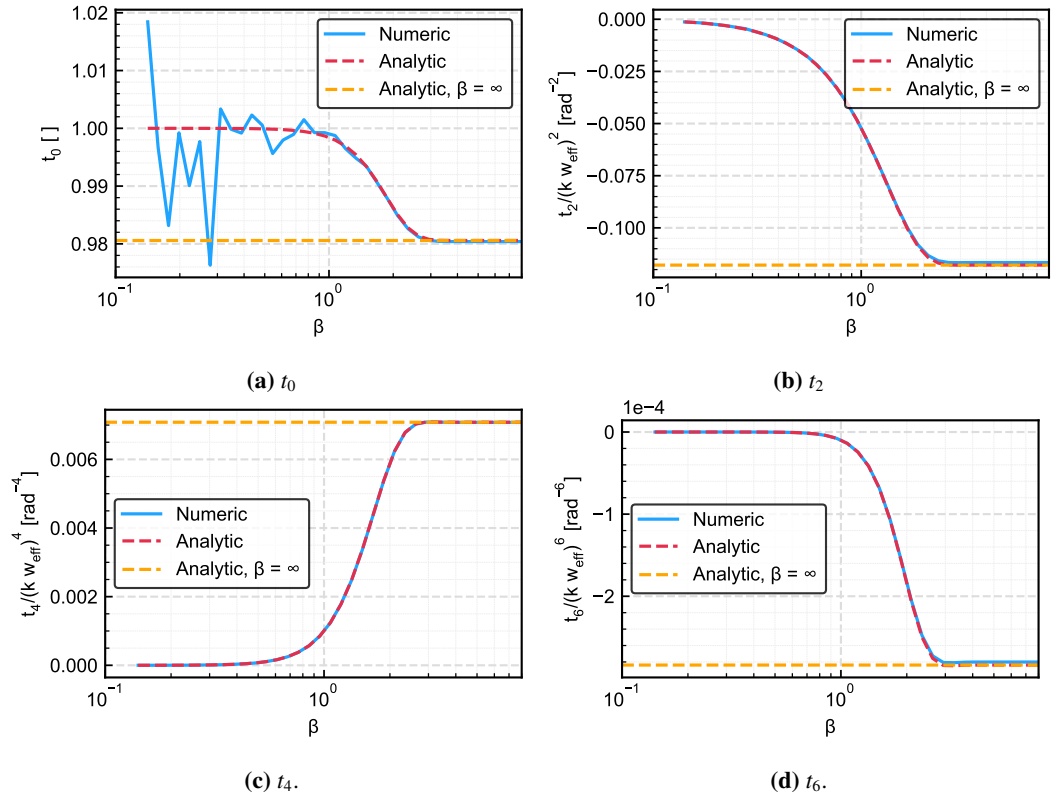


Figure 15: Plots of the t_0 , t_2 , t_4 and t_6 coefficients as a function of the ratio between SEPD radius and effective beam spot radius $\beta = \sqrt{2}r_{\text{SEPD}}/w_{\text{eff}}$ calculated both analytically using eq. (147), and numerically (see subsection 3.8). The used beam parameters are $w_r = w_m = w_{\text{eff}} = 1$ mm and $\rho = 0.2$. The numeric parameters are obtained by numerically integrating eq. (24) and linearly fitting the resulting HE, as explained in section 3.8. The deviation of the numerically calculated t_0 for low β values is attributed to fitting error. In the $\beta \rightarrow \infty$ limit, the expansion coefficients of eq. (41) are recovered. In the $\beta \rightarrow 0$ limit, t_0 tends to 1 while t_2 , t_4 and t_6 tend to zero, confirming eqs. (77) and (78). The plot shows the same large change in HE around $\beta = 1$ found in Figure 12.

eq. (75), for the top segments is reported in eq. (82) to second-order in θ .

$$\begin{aligned}
P_{\text{QPD, top, } \circ}(\theta) &= \int_0^{r_{\text{QPD}}} r dr \int_0^{2\pi} d\phi I_{\text{smp-}\theta 2}(r, \phi, \theta) \\
&= \frac{w_{\text{eff}}^2}{16(1-i\rho)^2} \left(8(1-i\rho) - k^2 w_{\text{eff}}^2 \theta^2 - e^{-2 \frac{r_{\text{QPD}}^2}{w_{\text{eff}}^2} (1-i\rho)} \left(-i \frac{16k}{\pi} r_{\text{QPD}} (1-i\rho) + 8(1-i\rho) - 2k^2 \theta^2 (r_{\text{QPD}}^2 (1-i\rho) + w_{\text{eff}}^2) \right) \right) \\
&\quad + \frac{k w_{\text{eff}}^3 \theta}{(2(1-i\rho))^{\frac{3}{2}} \sqrt{\pi}} \operatorname{erf} \left(\frac{r_{\text{QPD}} \sqrt{2(1-i\rho)}}{w_{\text{eff}}} \right) + O(k\theta)^3
\end{aligned} \tag{82}$$

Also here, the expression for the bottom segments can be calculated by reversing the sign of θ . Unlike in the case of the finite SEPD, the calculation of the absolute value of eq. (82) is analytically intractable, as the imaginary error function cannot be separated into real and imaginary parts in closed form if its argument is complex; a similar problem was encountered in [26, subsection III.B]. To get around this issue, we further Maclaurin-expand in the parameter ρ . This choice is motivated by the fact that the values of ρ are typically small [38, 26]. This procedure leads to a much more complicated series, which also contains odd terms in θ . As this is a relevant case for LISA, the resulting HE for a finite QPD is reported to fourth-order in θ and second-order in ρ in eq. (148).

Also here, new knowledge can be gained from eq. (148) regarding the limit of the coefficients t_0 - t_4 for small QPD radii. This gives a similar result as in the case of the finite SEPD, with the HE tending to a constant value of one independently of ρ and θ . Note that the term t_1 , which is related to the shift of the peak angle of the HE as argued in subsection 3.3, also tends to zero. This implies that, by reducing the radius of the QPD, the asymmetry created by a wavefront curvature mismatch is also reduced. This is reasonable, as the local phase offset between the beams, which is the ultimate cause of the HE's degradation, is proportional to the distance from the QPD center; limiting such distance also limits the maximum possible phase offset.

$$\lim_{\beta \rightarrow 0} \sqrt{\eta_{\text{het, } 0}} t_0 = 1 \quad \forall \rho, \theta \tag{83}$$

$$\lim_{\beta \rightarrow 0} \sqrt{\eta_{\text{het, } 0}} t_1 = 0 \quad \forall \rho, \theta \tag{84}$$

$$\lim_{\beta \rightarrow 0} \sqrt{\eta_{\text{het, } 0}} t_2 = 0 \quad \forall \rho, \theta \tag{85}$$

$$\lim_{\beta \rightarrow 0} \sqrt{\eta_{\text{het, } 0}} t_3 = 0 \quad \forall \rho, \theta \tag{86}$$

$$\lim_{\beta \rightarrow 0} \sqrt{\eta_{\text{het, } 0}} t_4 = 0 \quad \forall \rho, \theta \tag{87}$$

Also here, we use numerical simulations (see subsection 3.8 for more details) to assess the validity of the approximations for finite QPD sizes. Figure 16 compares the HE on a finite QPD of two beams calculated either numerically using the method described in subsection 3.8, or analytically to second-order using eq. (148). Figure 17 shows a comparison between the analytically calculated t_0 , t_1 and t_2 coefficients using eq. (148), and the numerically calculated ones following the procedure in Section 3.8. The plots show that, for small values of β , both t_1 and t_2 are suppressed, as indicated by the limits in equations eqs. (83–85), while t_0 tends to one.

3.7 Top-Hat - Gaussian Beam on a Finite PD

This subsection addresses the calculation of the heterodyne interference of a GB with a tilting TH beam on a finite PD; this case is what is needed to describe the SCI in LISA, if the PD is a QPD. This result is built on subsection 3.4, with minor adaptations. The calculation of the HE requires, first, the beam powers impinging on the PD. This is given by eq. (71) for a GB - the reference beam - on a finite size SEPD. The same calculation for the TH beam needs to be addressed more carefully: the radius of the TH beam r_{TH} in eq. (62) needs to be compared to the radius of the PD r_{PD} ; the smallest of the two determines the detected TH beam's power. We formalize this as

$$P_{\text{PD, } \circ, \text{ TH}} = I_{\text{TH}} \pi r_{\text{min}}, \quad r_{\text{min}} = \min(r_{\text{PD}}, r_{\text{TH}}) \tag{88}$$

Second, we have to integrate the overlap intensity term on the PD. As described in subsection 3.4, the overlap intensity term of the two beams does not vary with respect to the GB-to-GB case, and can be described with eq. (24). However, the integration domain is limited to r_{min} .

$$P_{\text{SEPD, } \circ}(\theta) = \int_0^{r_{\text{min}}} r dr \int_0^{2\pi} d\phi I_{\text{smp}}(r, \phi, \theta) \tag{89}$$

$$P_{\text{QPD, top, } \circ}(\theta) = \int_0^{r_{\text{min}}} r dr \int_0^{2\pi} d\phi I_{\text{smp}}(r, \phi, \theta) \tag{90}$$

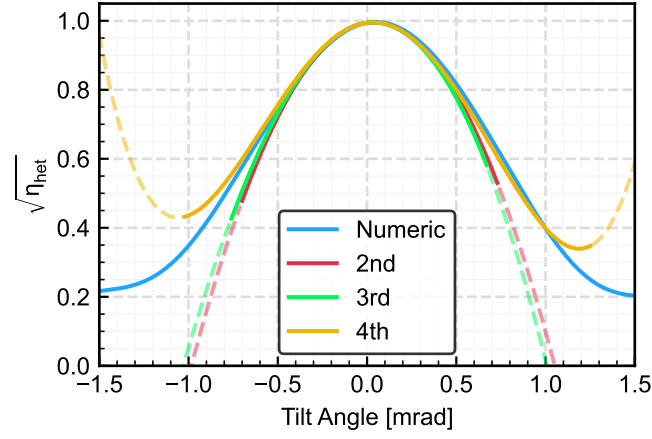


Figure 16: Plot of the HE as a function of the beam tilt calculated for the top segments of a finite QPD for the parameters $w_{\text{eff}} = 1 \text{ mm}$, $r_{\text{QPD}} = 1 \text{ mm}$ and $\rho = 0.2$. The HE is calculated both numerically and analytically at various orders. The analytic line is dashed when its value departs from the numerical one by more than 0.1.

The overlap power is hence described with the same equations eqs. (76) and (82) in the case of a SEPD or a QPD respectively, with the *caveat* that the β parameter must be adjusted to using the minimum of the two radii as in eq. (88):

$$\beta \rightarrow \frac{\sqrt{2}r_{\min}}{w_{\text{eff}}}. \quad (91)$$

The parameter β_r is unchanged, as the reference GB must be integrated on the whole PD area, while β_m is not needed anymore. The final expressions for the heterodyne efficiency eqs. (147) and (148) also hold, with the only adjustment

$$\frac{2w_r w_m}{w_r^2 + w_m^2} \frac{1}{\sqrt{1 - \exp(-\beta_r^2)} \sqrt{1 - \exp(-\beta_m^2)}} \rightarrow \frac{\sqrt{2}w_r}{r_{\min}} \frac{1}{\sqrt{1 - \exp(-\beta_r^2)}}. \quad (92)$$

In the expression for a SEPD, eq. (92) leads to the same simplification which occurred in eq. (69), where $w_r(1 + \rho^2)^{-\frac{1}{2}} \rightarrow w_{0,r}$. As an example, the HE resulting from the interference of a GB-TH beam pair on a finite SEPD is plotted in Figure 18 for three values of the parameter β . For simplicity, we set $r_{\text{TH}} = r_{\text{SEPD}}$. Figure 19 compares the analytically calculated t_0 , t_2 , t_4 and t_6 coefficients to the numerically calculated ones for a specific value of $\rho = 0.2$ and $r_{\text{TH}} = r_{\text{SEPD}}$. The numerical model confirms the analytically estimated coefficients. Note that, with respect to Figure 15, all coefficients tend to zero for $\beta \rightarrow \infty$.

3.8 Heterodyne efficiency numeric model for a generic PD

A numerical model can be developed to address all HE calculations that cannot be carried out analytically, following the same approach as in [26, Subsection III.C]. These include arbitrary PD geometries and values of ρ that extend beyond the validity range of the previous Maclaurin expansions. The model is also used to verify the validity of the previous analytical approximations, as those performed between eqs. (18) and (19). The power incident on each PD/QPD-segment is computed by numerically integrating the beam intensity (eq. (24) in the approximated case), employing a discretization of both the QPD surface and the tilt angles. A similar approach is followed by the AEI-developed simulation software IfoCAD [41], which is, furthermore, capable of simulating large-scale optics experiments. Due to the simplicity of our purpose, we opted for our own numerical integrator. The corresponding phase is then extracted as the argument of the resulting complex power $P_{\text{num}}(\theta)$.

$$\begin{aligned} P_{\text{num}}(\theta) &= \int \int_{S_{\text{PD}}} dx dy I_{\text{smp}}(x, y, \theta) \approx \\ &\approx \sum_i^{x_i \in S_{\text{PD}}} \sum_j^{y_j \in S_{\text{PD}}} I_{\text{smp}}(x_i, y_j, \theta_k) \Delta s^2 + O(\Delta s^4) \end{aligned} \quad (93)$$

As the amount of sums to be taken is proportional to Δs^2 , the discretization introduces an overall numerical error that scales as Δs^2 . We found that a spatial resolution of $\Delta s = 5 \text{ }\mu\text{m}$, which limits the integration's runtime to a few seconds, induces HE numerical artifacts of approximately 10^{-7} at most for a beam of effective spot radius 1 mm when integrating on both a SEPD (see Figure 20a) or a QPD-segment (see

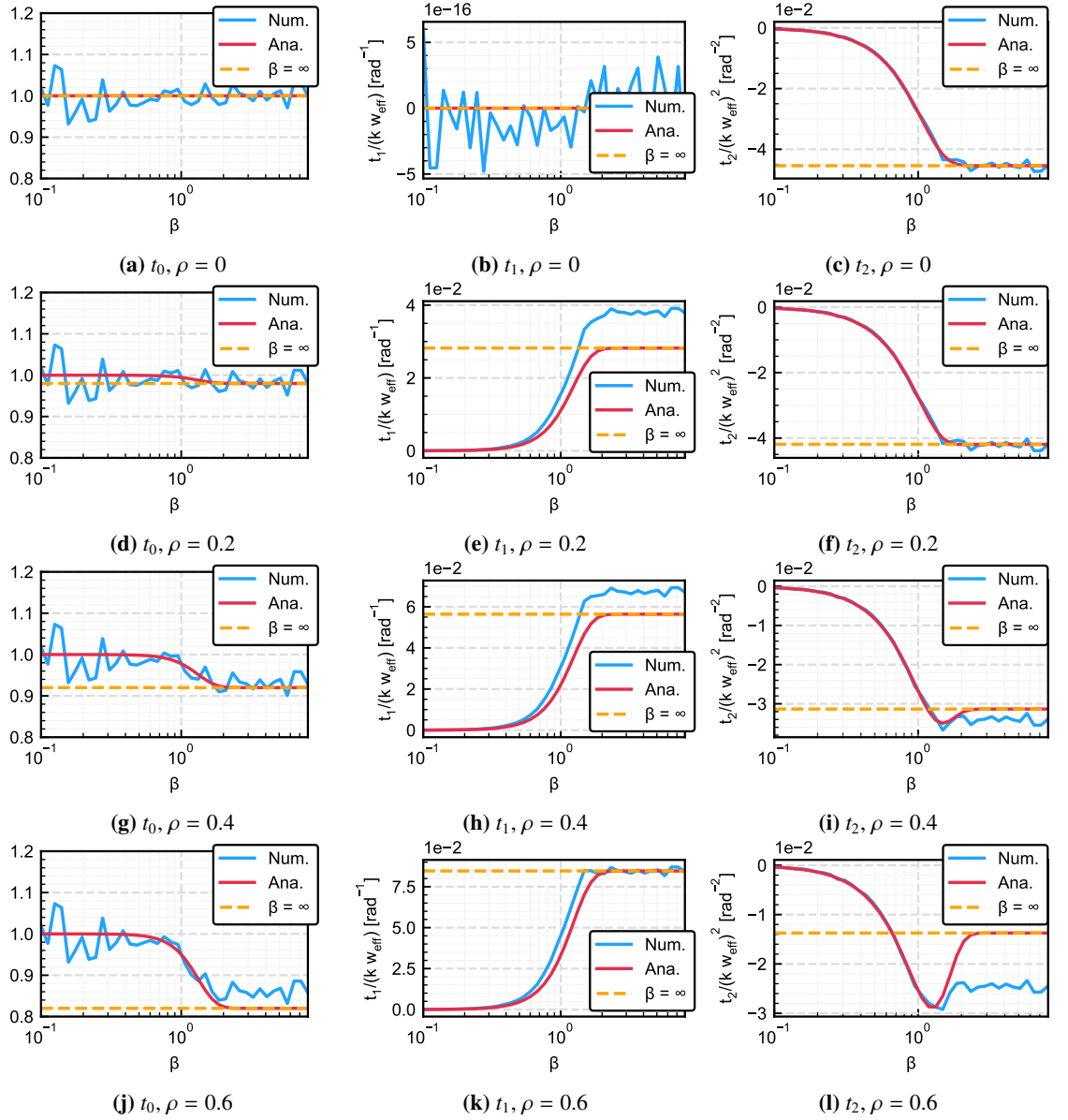


Figure 17: Comparison between the analytically obtained parameters t_0 , t_1 and t_2 from eq. (148) and the numerically calculated ones for four specific values of ρ and as a function of the parameter $\beta = r_{\text{QPD}}/w_{\text{eff}}$. t_1 and t_2 are normalized respectively by the first and second power of kw_{eff} . The asymptotic analytical value for an infinite QPD $\beta \rightarrow \infty$ is added as reference. In figs. 17a and 17b, for $\rho = 0$, the numerical solution matches the analytically predicted value of zero up to its numerical precision. In all other subfigures, the finite analytical model is in good accordance with the numerical model up to $\beta \sim 1$, where the numerical model systematically underestimates the value of the coefficients. Note that the numerical estimation of t_1 improves at higher ρ values (excluding $\rho = 0$), while that of t_2 behaves oppositely. These departures of the numerical model are understood as systematic fitting error, as the HE develops an asymmetric and non-quadratic shape. The plot shows the same large change in HE around $\beta = 1$ found in Figure 12

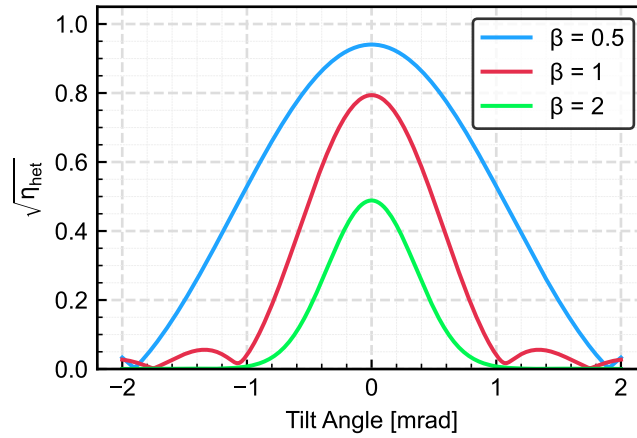


Figure 18: Plot of the HE as a function of the beam tilt numerically calculated for a GB-TH beam pair impinging on a finite SEP. The beam parameters are $w_{\text{eff}} = 1$ mm, $r_{\text{TH}} = r_{\text{SEP}} = [0.5, 1, 2]/\sqrt{2}$ mm and $\rho = 0.2$. Note that to a larger PD size corresponds a lower HE. Note that in the $\beta = 0.5$ and $\beta = 1$ plots diffraction fringes are visible outside the main peak. These are the causes of the DWS sign reversal discussed in [26, Figure 11].

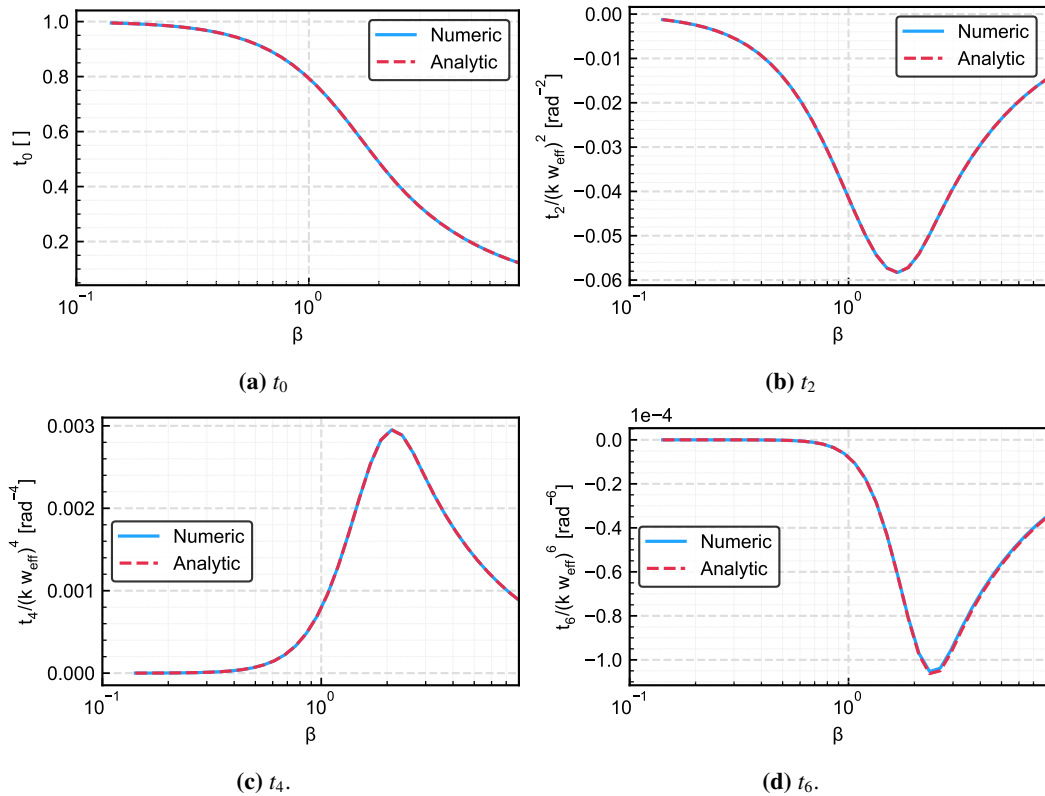


Figure 19: Plots of the t_0 , t_2 , t_4 and t_6 coefficients as a function of the ratio between SEP radius and effective beam spot radius $\beta = \sqrt{2}r_{\text{SEP}}/w_{\text{eff}}$ calculated for a GB-TH beam interference both analytically using eq. (147), and numerically (see subsection 3.8). The used beam parameters are $w_r = w_{\text{eff}} = 1$ mm, $\rho = 0.2$ and $r_{\text{TH}} = r_{\text{SEP}}$. Note that all coefficients tend to zero for $\beta \rightarrow \infty$ due to the normalization to an infinitely growing power.

Figure 20b), which is well within the target precision of this model. From the numerically computed power $P_{\text{num}}(\theta)$, the HE is extracted by evaluating its absolute value and normalizing it by the power of the two beams according to eq. (35). Finally, the parameters $t_0, t_1 \dots t_n$ are obtained by performing a linear fit of the resulting HE. We stress that this process is sensitive to the used angular fitting range, which must be adjusted accordingly to the order of the linear fit.

Numerical integrations are used to assess the validity of the approximations introduced between eq. (18) and eq. (19). The discrepancy between the fully numerically integrated HE — using eq. (18) for the measurement beam — and the approximated numerically integrated HE — using eq. (19) for the measurement beam — is of the order of 10^{-6} in the case of a SEPD (see Figure 20c) and at most of 10^{-3} in the case of a QPD (see Figure 20d). We conclude that this analytical model can estimate the HE with deviations smaller than 10^{-6} in the case of a SEPD. In the case of the QPD, the introduced approximations cause a discrepancy of the order of 10^{-4} within ± 0.5 mrad of tilt; such discrepancy grows linearly for larger tilts, in an area of lower interest for the LISA mission.

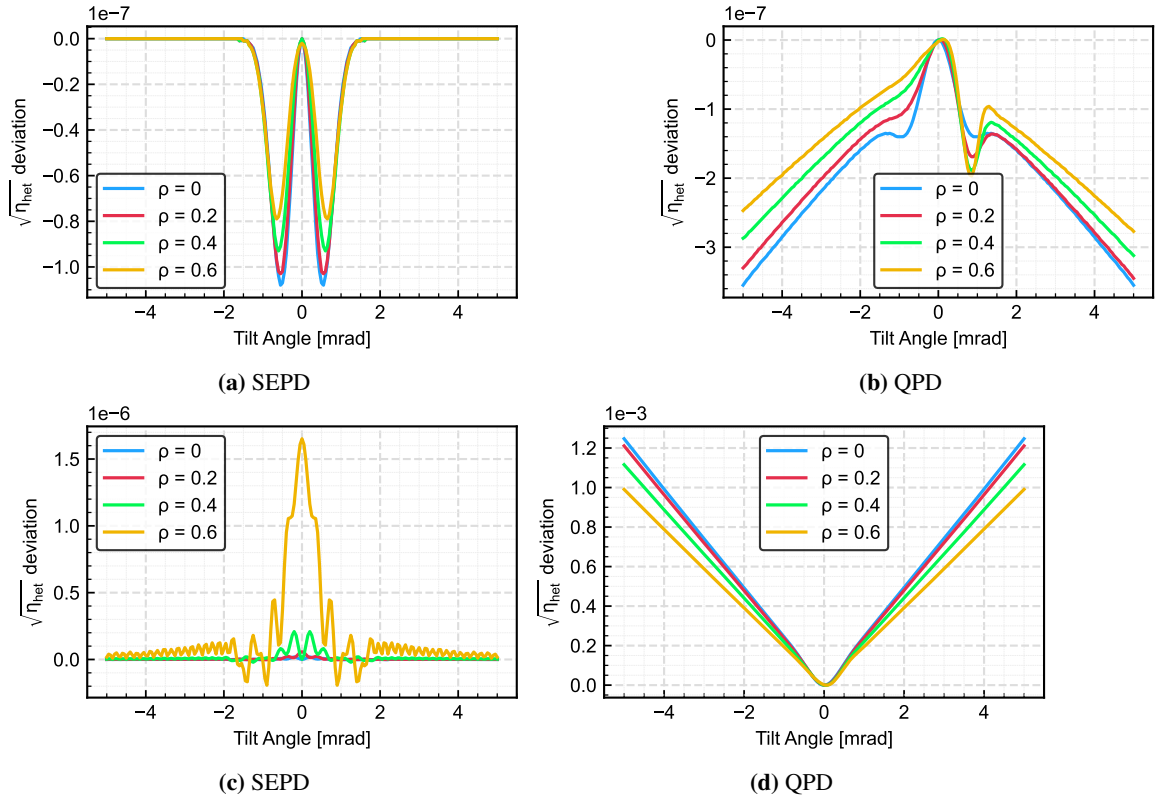


Figure 20: Above: Plot of the difference between numerically calculated HE and the analytically calculated HE for a $w_{\text{eff}} = 1$ mm beam impinging on an infinite SEPD (Figure 20a) and an infinite QPD (Figure 20b). In both cases, the approximated expression for the intensity in equation eq. (19) is used. This results in the numerical integration’s artifacts; note that the magnitude of such artifact depends on the spatial discretization Δs^2 used in the numerical integration; the result plotted in this figure uses $\Delta s = 5\mu\text{m}$. Note that fig. 20b is symmetric under the $\theta \rightarrow -\theta$ transformation only for $\rho = 0$, as wavefront mismatches break the tilt symmetry (see Figure 11). Below: Plot of the difference between numerically calculated full HE and approximated HE for a $w_{\text{eff}} = 1$ mm beam impinging on an infinite SEPD (Figure 20c) and an infinite QPD (Figure 20d). The full HE uses eq. (18) for the tilted measurement beam, and the resulting intensity can be integrated only numerically. The approximated HE uses eq. (19) instead. This discrepancy between the two outputs of the numerical integration is the effect of the approximations introduced between eq. (18) and eq. (19). Such effect is very small in the SEPD-case, where a strong dependency on ρ is also visible, while relatively large in the QPD-case, where it diverges for large tilts. Still, the most relevant part, between -0.5 mrad and 0.5 mrad is addressed within 10^{-4} precision.

4 Heterodyne Efficiency and Imaging Systems

Consider a pair of beams, i.e., a measurement beam and a reference beam, impinging on a large PD. Both beams are nominally incident perpendicular to the detector surface; however, the measurement beam is allowed to rotate by a small angle θ about the center of the PD. The effective beam spot radius and the relative RoC at the PD are denoted by w_{eff} and R_{rel} , respectively. In this configuration, the HE of the beams on the PD is given by eq. (41) in the case of a SEPD, or by eq. (47) eq. (49) in the case of a QPD.

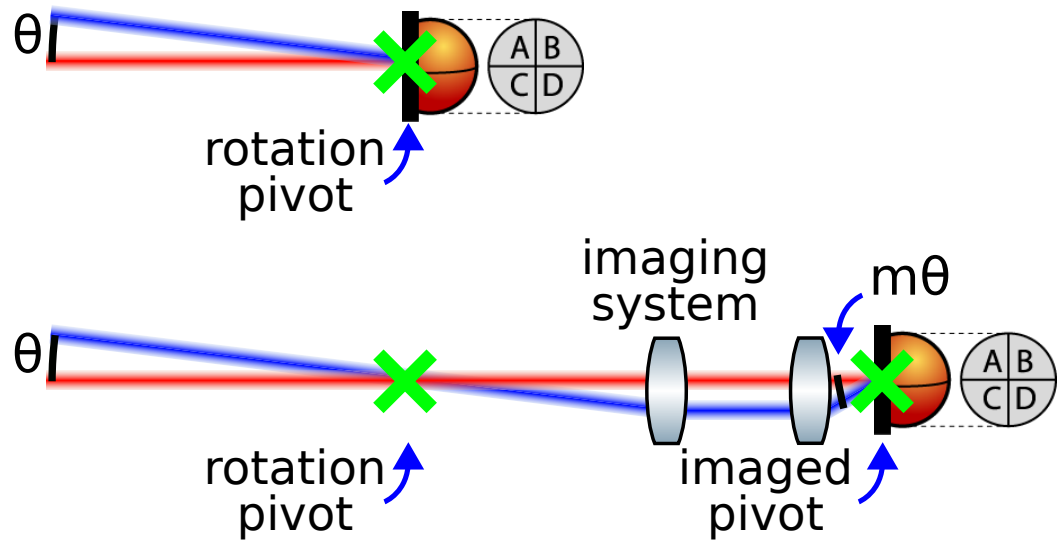


Figure 21: Drawing of the two systems compared in this section. *Above:* two beams impinging on a QPD, with the measurement beam (in blue) rotated about the center of the QPD by an angle θ . *Below:* same system as above, with an ensemble consisting of an imaging system plus a QPD being placed instead of the QPD. Note that in this case the measurement beam's angle at the QPD is magnified to $m\theta$.

Now, consider introducing a collimating imaging system as depicted in Figure 21: the entrance pupil of the imaging system is placed at the original position of the PD, while the PD itself is relocated to the exit pupil. What is the resulting HE as a function of the tilt angle for this combined system of imaging optics and detector? The propagation of a GB through a collimating imaging system with angular magnification m modifies the beam parameters according to equations eqs. (3) and (4). These transformations apply not only to the individual beam parameters, but also to the effective beam spot radius w_{eff} , the relative radius of curvature R_{rel} , and the parameter ρ [26].

$$w_{\text{eff, out}} = m^{-1} w_{\text{eff, in}} \quad (94)$$

$$R_{\text{rel, out}} = m^{-2} R_{\text{rel, in}} \quad (95)$$

$$\rho_{\text{out}} = \rho_{\text{in}} \quad (96)$$

An important consequence is that the parameter ρ (the effective-spot-radius-normalized wavefront curvature mismatch) is invariant under propagation through a collimating imaging system. In contrast, the tilt angle θ between the beams is magnified by a factor m , as described by eq. (2). When computing the HE for such a beam configuration using an infinitely large PD, the m factors cancel in eqs. (41), (47) and (49). In other words, the previously mentioned quantity $\Theta = kw_{\text{eff}}\theta$ is invariant under the presence of a collimating imaging system. Therefore, in the limit of small tilts and infinite detector size, the HE as a function of the tilt angle remains unchanged in the presence of the imaging system. For a finite-sized PD, the HE remains invariant as long as the ratio $\beta = \sqrt{2}r_{\text{PD}}/w_{\text{eff}}$ is conserved. However, this conclusion breaks down when the magnified tilt becomes large enough to invalidate the linear approximation in θ used in eq. (19) [26, Section III]. A similar argumentation is derived in [26, Section IV] for the DWS signal.

5 Experimental Results

This section presents the HE measurements performed using TDOBS, aimed at experimentally validating the HE model. Before discussing this in detail, it is important to stress that an experimental measurement of the HE in heterodyne interferometry is not trivial at all, or, at least, is way more complex than a DWS calibration. While to obtain the DWS signal, it is sufficient to measure the phase of the MHz heterodyne beat note, to measure the HE one has to compare the amplitude of the MHz heterodyne beat note to the DC powers of the two interfering beams. This is especially tricky, as the involved electronics usually present different transfer function (TF) at DC and at MHz. Furthermore, the TF at MHz is frequency dependent. Moreover, for technical convenience, the AC and DC components of the photocurrents in TDOBS are often processed separately; this happens also in TDOBS, where the output signal of the TIA is fed to a second-stage amplifier, which splits it into a DC ($f < 10 \text{ kHz}$) and AC ($f > 10 \text{ kHz}$) components. These are

then acquired by different devices: the DC component is digitized by the I/Q demodulation phasemeter, while the AC component is digitized by the DPLL phasemeter.

It is, hence, fairly difficult to perform an absolute measurement of the HE. The HE is, in principle, f_{het} -independent; however, some f_{het} -dependency will unavoidably leak in due to the electronics' TF, adding a frequency-dependent scaling factor $G(f)$. Relative variations of the HE measured at one specific frequency are, however, unaffected by this re-scaling issue.

5.1 Absolute Heterodyne Efficiency Measurement

A solution that we found to compare the beat note and DC power amplitude is to process both through the DC readout chain. We have set the beat note frequency to a few tenths of Hz¹; this enables measuring both DC powers and beat note using the DC chain [25, subsection 3.2.2]. The HE can then be extracted by using eq. (38), adapted into eq. (97), by measuring the power of the two beams and the maximum and minimum power output independently. We remark that all DC offsets have been calibrated and removed in this procedure.

$$\sqrt{\eta_{\text{het}}} = \frac{P_{\text{PD, max}} - P_{\text{PD, min}}}{4\sqrt{P_{\text{PD, r}}P_{\text{PD, m}}}} \quad (97)$$

This led to the HE measurements reported in Table 1, which were performed with parallel beams impinging on the center of each QPD.

Beams & QPDs	β	Measured	Analytic Model	Numerical Model
Rx-GB & LO @ REFQPDs	0.74 ± 0.02	0.86 ± 0.01	$0.99939 \pm 1 \times 10^{-5}$	$0.9994 \pm 1 \times 10^{-4}$
Rx-FT & LO @ REFQPDs	0.570 ± 0.005	0.92 ± 0.01	$0.99196 \pm 1 \times 10^{-5}$	$0.9951 \pm 2 \times 10^{-3}$
Rx-GB & LO @ SCIQPDs	1.87 ± 0.01	0.98 ± 0.01	$0.9853 \pm 2 \times 10^{-4}$	$0.9853 \pm 2 \times 10^{-3}$

Table 1: Absolute HE measurements in TDOBS, obtained by a DC beatnote measurement using eq. (97) using single channels of a QPD, compared to a numerical model of the interference. The table also reports the value of $\beta = \sqrt{2}r_{\text{QPD}}/w_{\text{eff}}$ of the analyzed case. This measurement technique appears to suffer larger errors if β is close to 1.

The results in Table 1 show a strong limit, as only the measurement using the Rx-GB & LO on the SCIQPDs gives a result compatible with the HE model. We attribute the large discrepancies measured using the REFQPDs to unmodelled lateral offsets of the involved beams. Variations of the HE due to, for instance, wavefront curvature mismatch, are stronger if $\beta = \sqrt{2}r_{\text{QPD}}/w_{\text{eff}}$ is close to 1; we expect the same to hold true for residual beam lateral misalignment, which is of the order of a few μm .

5.2 Normalized Heterodyne Efficiency Measurement

A second possibility is, as mentioned, to neglect the exact value of the HE's scaling factor $G(f)$ and characterize only the variations of the HE. This approach allows us to study the HE variations due to beam tilt, while using heterodyne frequencies (HFs) in the LISA-heterodyne band. The main goal of this section is to characterize the asymmetry in the HE measured by the two QPD halves as a function of the beam tilt; this is possible because the beam pairs present a wavefront curvature mismatch [26]. This procedure was followed using the beam couple Rx-GB&LO on both the REFQPDs and SCIQPD.

We performed this analysis analogously to the DWS calibrations in [26, Section V]: the Rx beam is rotated about the center of the QPD under test, i.e., either the REFQPDs or the SCIQPDs, using the steering mirrors on the TS. The procedure is depicted in Figure 22; for a full description of this procedure, see [26, Section V]. To establish the calibration, the measured beam angle is compared with the corresponding HE. Equation (98) is the relation used to recover the beam tilt angle from the differential power sensing (DPS) measurement, where Δx_{AUXQPD} is the lateral displacement of the beam measured on the auxiliary QPD (AUXQPD), and $d_{\text{QPD-AUXQPD}}$ is the distance between the two QPDs along the beam path. This procedure is the main (systematic) uncertainty source of the measurement, as $d_{\text{REFQPD-AUXQPD}}$ is known to within $\sim 7\%$ precision.

$$\theta = \frac{\Delta x_{\text{AUXQPD}}}{d_{\text{REFQPD-AUXQPD}}} \quad (98)$$

This measurement was performed at $f_{\text{het}}=5$ MHz, with the difficulties in measuring the absolute HE mentioned above due to the little-known gain factor $G(f)$. To make the HE measurement independent of $G(f)$, we normalize the measured HE by its highest value. The measurements are then compared to numerical models built for the specific case. To quantitatively compare the data and the model, we fit both with a candidate function and compare the resulting fit parameters. For the Rx-GB & LO @ REFQPDs case, we fit a simple Gaussian curve in eq. (99), as the tilt range is too small to grasp the full asymmetry of the HE.

¹This is possible, as we generate the three different frequencies from the same laser source using three independent AOMs.

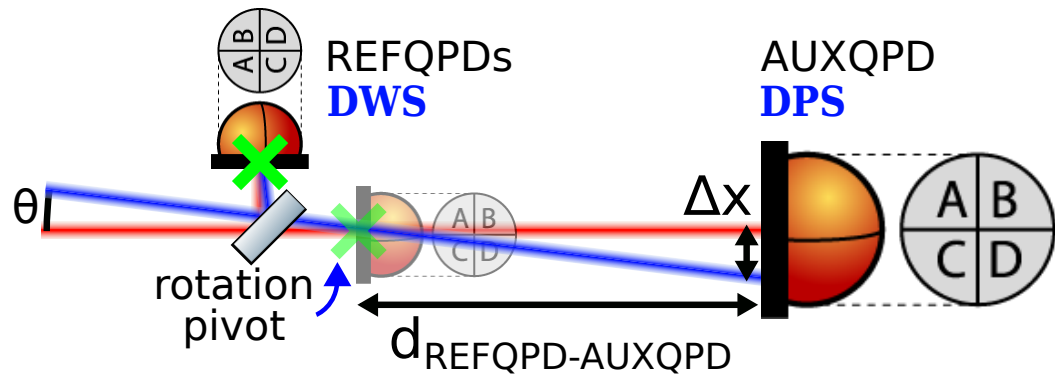


Figure 22: Drawing of the beam rotation process. The REFQPD is located on the left, while the AUXQPD is located on the right. The virtual position of the REFQPD along the beam path is also shown in transparency. The Rx beam's rotation pivot is indicated by the green cross. The lateral displacement Δx is measured using the DPS signal (see [26, Section V]) of the AUXQPD. The tilt angle of the Rx beam θ can be recovered trigonometrically using the eq. (98). The tilt angle in the figure is strongly exaggerated; this is in the range of ± 1 mrad. Figure from [26].

For the Rx-GB & LO @ SCIQPDs case, we use the full expression in eqs. (47) and (49), adapted into the fit-function form eq. (100). Note that a fit constant c was added to this equation. Despite this term not being present in the analytical model, it proves necessary to fit the HE of a finite QPD when using the curve for an infinite QPD. We stress that this is needed for fitting both experimental data and the numerically simulated HE, leading to similar estimated values of c . The reason why this constant must be added is related to the finite size of the QPD, which causes diffraction fringes to appear. If just a portion of these is included in the measurement's angular range, it manifests as an effective offset of the measured HE; a good example of this is Figure 16, where the numerically calculated HE indeed looks like a Gaussian curve with an added positive constant taking a value of roughly 0.2 in the plotted range. The parameter ρ , which is known from previous measurements to be equal to $\rho = 0.14 \pm 0.1$ in both analyzed cases [25, Figure 3.9], is fed as a fixed parameter of eq. (100) to the fit routine, as it would not converge otherwise. The parameter s , which has a theoretical value of $s_{\infty} = \frac{m}{kw_{\text{eff}}} = 0.137 \pm 0.002$ mrad for an infinite QPD, is left free, as its effective value is affected by the finite size of the QPD.

$$f(x) = a \exp\left(-\left(\frac{x-x_0}{s}\right)^2\right) \quad (99)$$

$$g_{\pm}(x) = a \exp\left(-\left(\frac{x-x_0}{s}\right)^2\right) \sqrt{1 \pm 2 \operatorname{Im}\left[\frac{x-x_0}{2^{3/2}s\sqrt{1-i\rho}}\right] + \left|\frac{x-x_0}{2^{3/2}s\sqrt{1-i\rho}}\right|^2} + c \quad (100)$$

The measured and simulated HEs are plotted in Figures 23 and 24. The respective fit parameters are reported in Tables 2 and 3. We note that this small value of ρ is large enough to introduce a detectable difference in the peak angles of the HEs of the two QPD halves during a tilt. This effect is still visible, despite being suppressed by the small value of β , in the REFQPDs. Note that, due to small beam misalignment, the tilt angle at which the two HEs share the same value is not exactly zero. This must be taken into account when comparing the data with the simulation in Figures 23b and 24b; here we shift the x -axis by $\bar{x}_0 = \frac{1}{2}(x_{0, \text{1st half}} + x_{0, \text{2nd half}})$, where the parameters $x_{0, \text{1st half}}$ and $x_{0, \text{2nd half}}$ are estimated by fitting eqs. (99) and (100) to the HEs of the two QPD halves.

Figure 23a shows the normalized measured HE as a function of the beam tilt angle using the Rx-GB & LO on REFQPD1. In this system, $\rho = 0.14 \pm 0.1$ and $\beta = 0.74 \pm 0.02$, meaning that the effects of the wavefront curvature mismatch on the two REFQPD1's halves are expected to be suppressed (see Figures 17d to 17f). Due to the limited angular range, the expected HE is expected to have a near-Gaussian shape; we therefore fit it using eq. (99), which indeed proves a very valid fit of the data points. This measurement is able to capture a tiny difference in the peak angles of the HE of the two REFQPD1's top and bottom halves. Figure 23b compares the resulting fit from Figure 23a with the numerical model developed in subsection 3.8. Table 2 compares the parameters obtained by fitting the data in Figure 23a and the model in Figure 23b with eq. (99). Measurement and simulation look quite different at first glance. However, neglecting the small uncertainties in the parameter furnished by the fit, note that the resulting s parameters present a fairly small relative discrepancy. Such discrepancy is larger, but still very small in absolute value, for the x_0 parameter.

Figure 24a shows the normalized measured HE as a function of the beam tilt angle using the Rx-GB & LO on SCIQPD1. Note that this system differs with respect to the Rx-GB & LO on REFQPD1 only due to the presence of a collimating imaging system, and therefore the two are related by the argument presented in

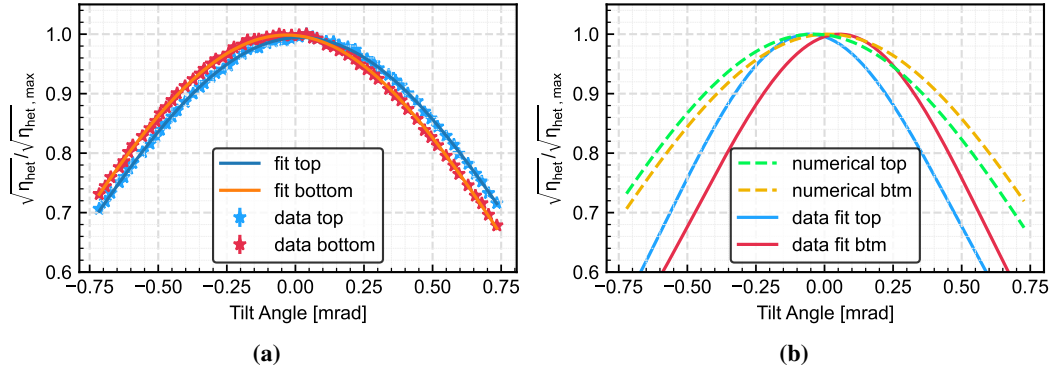


Figure 23: *Left:* Measurement of the HE as a function of the beam tilt angle using the Rx-GB&LO beams on REFQPD1. We remind that the HE has been normalized to its maximum value. The Rx-GB beam was tilted vertically, hence we show the HE measured on the top and bottom segments of the QPD. The parameters of the two interfering beams are $w_r = 0.874 \pm 0.006$ mm, $w_m = 1.038 \pm 0.008$ mm, $w_{\text{eff}} = 0.95 \pm 0.02$ mm, $\rho = 0.14 \pm 0.01$, $\beta = 0.74 \pm 0.02$. The fit is performed using eq. (99). The resulting fit parameters are reported in Table 2. *Right:* Comparison between the Gaussian fit in Figure 23a and the numerical model.

Parameter	Units	QPD-Top	QPD-Bottom	Model	Relative Discrepancy
a	-	0.9945 ± 0.004	0.9986 ± 0.0005	1 ± 0.0001	-
s	mrad	1.245 ± 0.002	1.222 ± 0.002	1.293 ± 0.0007	4.6%
$x_0 - \bar{x}_0$	mrad	0.0258 ± 0.0007	-0.0258 ± 0.0006	$\pm(0.017 \pm 0.0003)$	51%

Table 2: Table with the fit parameters from Figure 23. The centroids of the Gaussian curves are already corrected by the average centroid shift $\bar{x}_0 = -6.7 \pm 0.5$ μrad . This small deviation is attributable to a lateral misalignment of the beams with respect to the QPD. The last column reports the relative discrepancy, defined as $\frac{\text{theo}-\text{meas}}{\text{theo}}$, where $\overline{\text{meas}}$ is the average of the measured parameter for the two QPD halves. Note that the discrepancy between the measured and modelled value of s is large if compared to the errors, but relatively very small.

Section 4. Note that the angular range is magnified by the presence of the imaging system. In this system, $\rho = 0.14 \pm 0.1$ and $\beta = 1.87 \pm 0.01$, meaning that the effects of the wavefront curvature mismatch on the two SCIQPD1's halves are expected to be roughly half of those on an infinite QPD (see Figures 17d to 17f), and way more noticeable than on the REFQPDs. This measurement evidences a noticeable asymmetry between the two SCIQPD halves, and a clear difference in peak angle of the two HEs; we hence use eq. (100) to fit the experimental data. We observe that the model closely follows the experimental data, although not exactly. Figure 24b compares the resulting fit from Figure 24a with the numerical model developed in subsection 3.8. Table 3 compares the parameters obtained by fitting the data in Figure 24a and by fitting the numerical model in Figure 24b; despite the discrepancies between the estimated parameters being much larger than the associated uncertainties, the relative discrepancies are fairly small. In particular, the position of the HE's maximum, x_0 , is predicted very accurately by the numerical model, while the s parameter has a relative uncertainty as high as 23%.

Parameter	Units	QPD-Left	QPD-Right	Model	Relative Discrepancy
a	-	0.759 ± 0.003	0.801 ± 0.003	0.817 ± 0.002	4.5%
s	mrad	1.50 ± 0.01	1.49 ± 0.01	1.950 ± 0.007	23%
$x_0 - \bar{x}_0$	mrad	0.123 ± 0.005	-0.123 ± 0.005	$\pm(0.126 \pm 0.001)$	2.4%
c	-	0.237 ± 0.005	0.201 ± 0.005	0.187 ± 0.003	-17%

Table 3: Table with the fit parameters from Figure 24. The centroids of the Gaussian curves are already corrected by the average centroid shift $\bar{x}_0 = -142 \pm 5$ μrad . This small deviation is attributable to a lateral misalignment of the beams with respect to the QPD. The last column reports the relative discrepancy, defined as $\frac{\text{theo}-\text{meas}}{\text{theo}}$, where $\overline{\text{meas}}$ is the average of the measured parameter for the two QPD halves. Note that the discrepancy between the measured and modelled values of all parameters is large if compared to the uncertainties, but relatively very small.

A comparison between these two measurements can be used to obtain a result which is independent of the systematic uncertainties due to eq. (98). This is possible, as mentioned, because these two setups measure the interference of the Rx-GB&LO beams at the REFQPDs and SCIQPD, and only differ due to the

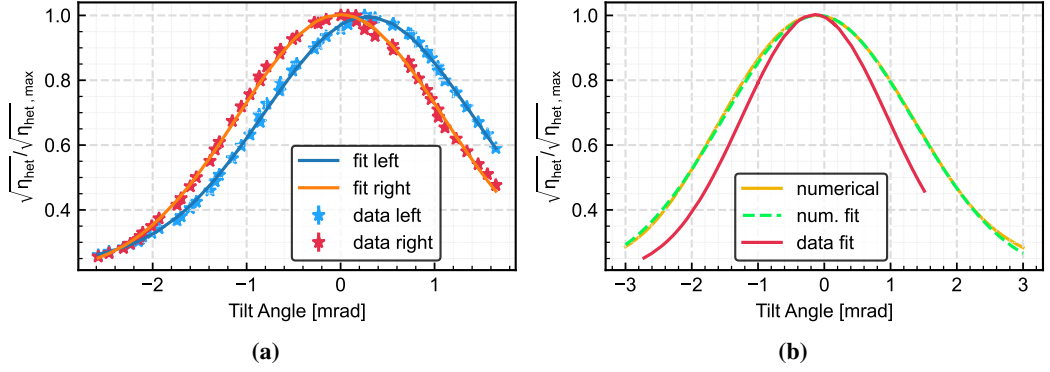


Figure 24: *Left:* Measurement of the HE as a function of the beam tilt angle in TDOBS using the Rx-GB&LO beams on SCIQPD1. We remind that the HE has been normalized to its maximum value. The Rx-GB beam was tilted horizontally, hence we show the HE measured on the left and right segments of the QPD. The parameters of the two interfering beams are $w_r = 0.350 \pm 0.002$ mm, $w_m = 0.415 \pm 0.003$ mm, $w_{\text{eff}} = 0.377 \pm 0.002$ mm, $\rho = 0.14 \pm 0.01$, $\beta = 1.87 \pm 0.01$. The Fit is performed using eq. (100). The resulting fit parameters are reported in Table 3. *Right:* Comparison between the Gaussian fit in Figure 24a and the numerical model.

presence of a collimating imaging system. A similar method, using data from the same measurement, gave a very good result in [26, eqs (68) and (69)] while comparing the DWS of the same optical system. Similarly, we can use this comparison to cross-check the resulting value of the s parameter obtained in the two configurations. We measure and model

$$\frac{S_{\text{RxGB-LO @ REFQPDs, meas}}}{S_{\text{RxGB-LO @ SCIQPDs, meas}}} = 0.826 \pm 0.006 \quad (101)$$

$$\frac{S_{\text{RxGB-LO @ REFQPDs, model}}}{S_{\text{RxGB-LO @ SCIQPDs, model}}} = 0.663 \pm 0.004 \quad (102)$$

$$(103)$$

These values are relatively close, although not as absolutely close as expected. Potential issues in the used analysis lie in the choice of the fit function in eq. (100), where the constant c was necessary in order to correctly fit the data, or in the impact of beam lateral misalignments.

6 QPD signal readout noise

This section uses the knowledge derived in the previous Sections to calculate how beam tilts affect the phase noise in LISA's interferometers. As previously mentioned, LISA employs QPDs to measure the output power of its interferometers, such that it can measure not only longitudinal signals but also angular signals via DWS and beam position via DPS. The four phases derived by the outputs of a QPD are combined, after digitization, to obtain either the LPS or the DWS signals. During LISA's science operation, the measurement beams in the SCI and TMI can be affected by tilts up to 1 mrad, causing a significant reduction of the HE, and therefore of the beat note's amplitude. This causes the interferometric phase noise to increase; to predict how much it increases, a model of the HE as a function of the beam tilt angle is needed, which is what was carried out throughout this article.

6.1 Interferometric Noise

The interferometric readout noise affecting the output phase can be distinguished into direct phase noise, additive noise, and multiplicative noise. The first and third categories are HE independent. Laser frequency noise is also common-mode in all segments, and will hence be neglected in this model. To the last category belongs $2f$ -relative intensity noise (RIN)[40]. The additive noise category includes laser shot noise, electronic noise from the TIA, and $1f$ -relative intensity noise (RIN)[40], which are the main noise sources in LISA, and is HE-dependent. $1f$ -RIN is the coupling of relative intensity variations of the laser at the frequency of the beat note, while $2f$ -RIN couples relative intensity variations of the laser at twice the f_{het} .

We hence model how these noises affect the QPD-signals' readout, depending on the incidence angle of the measurement beam, while assuming that both beams are always centered on the QPD and that the reference beam is also always orthogonal to the detector's surface, as assumed in the framework introduced in Section 3. The reasoning presented in this subsection should also be extended to other additive noise, as digitization noise and PD dark current noise, but will be limited to the previously mentioned noise sources for simplicity, but could also easily be included.

The amount of phase noise caused by a noise contributor can be quantified using the inverse of eq. (39)

$$\tilde{\phi}_{\text{noise}} = \text{SNR}^{-1} = \frac{\text{Noise ASD}}{\text{Signal RMS}}, \quad (104)$$

where $\tilde{\cdot}$ indicates noise densities, "Noise ASD" indicates the amplitude spectral density (ASD) near and around the HF f_{het} , and "Signal RMS" indicates the root mean square (RMS) of the signal $s(t)$ over a period T , defined as [39]

$$\mathcal{RMS}\{s(t)\} = \sqrt{\frac{1}{T} \int_0^T [s(t)]^2 dt}. \quad (105)$$

The signal $s(t)$ is the last term of eq. (37) and its RMS is

$$\begin{aligned} \mathcal{RMS} \left\{ 2 \sqrt{\eta_{\text{het}}(\theta) \bar{P}_{\text{seg}, r} \bar{P}_{\text{seg}, m}} \cos(\omega_{\text{het}} t + \psi_{\text{het}}) \right\} \\ = \sqrt{2 \eta_{\text{het}}(\theta) \bar{P}_{\text{seg}, r} \bar{P}_{\text{seg}, m}}, \end{aligned} \quad (106)$$

where $\bar{P}_{\text{seg}, r}$, $\bar{P}_{\text{seg}, m}$ are the average powers of the reference and measurement beams impinging on each segment. Note that $\mathcal{RMS}\{s(t)\}$ depends on the tilt angle θ via the HE $\eta_{\text{het}}(\theta)$. We further assume θ to vary at frequencies much lower than the LISA-observation band. On the other hand, the ASDs of the various noises are specific to the particular noise cause and are discussed, for instance, in [25, subsection 2.1.5], and are independent of the tilt angle. The ratio of these two quantities, which gives the phase noise, is hence tilt-dependent, and such dependency is driven only by the HE. The resulting phase noises caused by the mentioned noise sources at QPD-segment level are given in eqs. (107–110) in units of rad/ $\sqrt{\text{Hz}}$.

$$\tilde{\phi}_{\text{shot}}(\theta) = \sqrt{\frac{(\bar{P}_{\text{seg}, r} + \bar{P}_{\text{seg}, m}) h \nu_l}{\eta_{\text{QPD}} \eta_{\text{het}}(\theta) \bar{P}_{\text{seg}, r} \bar{P}_{\text{seg}, m}}} \quad (107)$$

$$\tilde{\phi}_{\text{en}}(f_{\text{het}}, \theta) = \frac{\tilde{i}_{\text{en}}(f_{\text{het}})}{A \sqrt{2 \eta_{\text{het}}(\theta) \bar{P}_{\text{seg}, r} \bar{P}_{\text{seg}, m}}} \quad (108)$$

$$\tilde{\phi}_{\text{RIN-1}f}(f_{\text{het}}, \theta) = \frac{\bar{P}_{\text{seg}, r} \tilde{r}_r(f_{\text{het}}) \boxplus \bar{P}_{\text{seg}, m} \tilde{r}_m(f_{\text{het}})}{\sqrt{2 \eta_{\text{het}}(\theta) \bar{P}_{\text{seg}, r} \bar{P}_{\text{seg}, m}}} \quad (109)$$

$$\tilde{\phi}_{\text{RIN-2}f}(f_{\text{het}}) = \frac{\tilde{r}_r(2f_{\text{het}}) \boxplus \tilde{r}_m(2f_{\text{het}})}{2 \sqrt{2}} \quad (110)$$

where h is Planck's constant, ν_l is the frequency of the used laser beam, where we neglect the frequency difference as argued in [26], η_{QPD} is the quantum efficiency of the QPD, $A = \frac{q \eta_{\text{QPD}}}{h \nu_l}$ is the responsivity of the QPD, $\tilde{i}_{\text{en}}(f_{\text{het}})$ is the equivalent input current noise density of the QPR at the HF given in eq. (1), and \tilde{r}_r , \tilde{r}_m are the relative power variations of the reference and measurement beam at f_{het} for 1f-RIN and at twice f_{het} for 2f-RIN. All such parameters are assumed to be the same for all QPD segments in this model. The symbol \boxplus indicates the root-squared sum, which is used as the power fluctuations of the two beams are uncorrelated [40]. Except for 2f-RIN, all these noise contributions depend on the HE and are therefore dependent on the tilt angle θ . The total phase noise of the QPD segment i , with $i \in (A, B, C, D)$, is

$$\begin{aligned} \tilde{\phi}_i(f_{\text{het}}, \theta) = & \left(\tilde{\phi}_{\text{shot}}^2(\theta) + \tilde{\phi}_{\text{en}}^2(\theta) + \right. \\ & \left. + \tilde{\phi}_{\text{RIN-1}f}^2(f_{\text{het}}, \theta) + \tilde{\phi}_{\text{RIN-2}f}^2(2f_{\text{het}}) \right)^{-\frac{1}{2}}. \end{aligned} \quad (111)$$

The θ dependency in the three $\eta_{\text{het}}(\theta)$ dependent noise sources can be collected by re-writing eq. (111) in the following form.

$$\begin{aligned} \tilde{\phi}_{\text{shot/en/RIN-1}f, i} &= \Upsilon_{\text{shot/en/RIN-1}f, i} / \sqrt{\eta_{\text{het}}(\theta)}, \\ \Upsilon_{\text{shot}} &= \sqrt{\frac{(\bar{P}_{\text{seg}, r} + \bar{P}_{\text{seg}, m}) h \nu_l}{\eta_{\text{QPD}} \bar{P}_{\text{seg}, r} \bar{P}_{\text{seg}, m}}}, \\ \Upsilon_{\text{en}}(f_{\text{het}}) &= \frac{\tilde{i}_{\text{en}}(f_{\text{het}})}{A \sqrt{2 \bar{P}_{\text{seg}, r} \bar{P}_{\text{seg}, m}}}, \\ \Upsilon_{\text{RIN-1}f}(f_{\text{het}}) &= \frac{\bar{P}_{\text{seg}, r} \tilde{r}_r(f_{\text{het}}) \boxplus \bar{P}_{\text{seg}, m} \tilde{r}_m(f_{\text{het}})}{\sqrt{2 \bar{P}_{\text{seg}, r} \bar{P}_{\text{seg}, m}}}. \end{aligned} \quad (112)$$

where the quantities $\Upsilon_{\text{shot/en/RIN-1}f}$ are simply θ - and segment-independent experimental parameters, which we can treat as constants related to the noise levels on a single QPD-segment. Note that the segment-independency holds as long as both beams are centered on the QPD, which is what we assume. This step allows to rewrite eq. (111) as

$$\tilde{\phi}_i(f_{\text{het}}, \theta) = \sqrt{\frac{\Upsilon_{\text{shot}}^2 + \Upsilon_{\text{en}}^2(f_{\text{het}}) + \Upsilon_{\text{RIN-1}f}^2(f_{\text{het}})}{\eta_{\text{het}, i}(\theta)}} + \tilde{\phi}_{\text{RIN-2}f}^2(f_{\text{het}}). \quad (113)$$

In the following, we drop the explicit dependency on f_{het} for clarity. We hence calculate the phase noise of the QPD-signals, i.e. combinations of the individual QPD-segments' outputs as the DWS signals and the LPS. In particular, this section focuses on the dependence of phase noise at the QPD level on the tilt angle θ and the beam parameters, with particular emphasis on the effective-beam-spot-radius wavefront curvature mismatch ρ . We apply for this purpose the HE models derived in Section 3. For simplicity, this analysis is carried out assuming only vertical tilts. Note that the proposed reasoning is independent of the QPD size, whereas the resulting coupling factor is. However, as we want to explicitly calculate the resulting coupling factors as a function of the beam parameters, this is possible in closed form only for infinite QPDs. Considerations for a finite QPD can be done either in approximated form using the series expansion of the finite QPD HE in eq. (148), or numerically.

We acknowledge that, especially, the assumption of vertical-only tilts does not give a full picture of what happens in reality; in other words, the effect of a beam tilt θ_0 surely depends on its *azimuthal* angle on the QPD; we expect, however, the noise increase be well within one order of magnitude. A full derivation of this, however, would require a much longer analysis and is left for future work. This example focuses mainly on highlighting the new QPD noise feature arising from asymmetry in HE due to a wavefront curvature mismatch.

Such assumptions simplify the problem greatly, as it implies that the two top segments of a QPD (A and B) experience the same HE as discussed in subsection 3.3. Hence, we simplify to $i \in \{\text{top}, \text{btm}\}$ instead of the individual quadrants, and we name these $\sqrt{\eta_{\text{top}}(\theta)}$ for the top segments, given by eq. (47), and $\sqrt{\eta_{\text{btm}}(\theta)}$ for the bottom segments, given by eq. (49). Therefore, the QPD can also be simplified as having only two segments; therefore, the two QPD-signals, AP-LPS and DWS, can be expressed as

$$\phi_{\text{AP}} = \frac{1}{2} (\phi_{\text{top}} + \phi_{\text{btm}}), \quad (114)$$

$$\text{DWS} = \phi_{\text{top}} - \phi_{\text{btm}}. \quad (115)$$

The noise analysis must be carried out separately for noises that are correlated and uncorrelated across the QPD segments. This is carried out in the following two subsections.

6.2 Uncorrelated noises

Shot noise and electronic noise originate at the QPR segment, and are therefore uncorrelated between the segments. Their noise contributions to QPD signals can hence simply be added using the root square sum regardless of the signs in eqs. (114) and (115). This results in $\tilde{\phi}_{\text{AP}} = \frac{1}{2} \widetilde{\text{DWS}}$; we hence focus our analysis only on the DWS signal's noise, as that of the LPS can be recovered from it by applying the relation above. We can hence write

$$\begin{aligned} \widetilde{\text{DWS}}_{\text{unc}}(\theta) &= \sqrt{\tilde{\phi}_{\text{top}}^2(\theta) + \tilde{\phi}_{\text{btm}}^2(\theta)} \\ &= \sqrt{\Upsilon_{\text{shot}}^2 + \Upsilon_{\text{en}}^2} \sqrt{\frac{1}{\eta_{\text{top}}(\theta)} + \frac{1}{\eta_{\text{btm}}(\theta)}} \\ &= \sqrt{\Upsilon_{\text{shot}}^2 + \Upsilon_{\text{en}}^2} \sqrt{2} k_{\text{unc}}(\theta), \end{aligned} \quad (116)$$

where in the second line the DWS noise was rewritten using eq. (112), which allows to isolate the θ dependent factors, and in the third line the *QPD-signal tilt-coupling coefficient for uncorrelated noises* of a two-segment QPD $k_{\text{unc}}(\theta)$ was introduced.

$$k_{\text{unc}}(\theta) = \frac{1}{\sqrt{2}} \sqrt{\frac{1}{\eta_{\text{top}}(\theta)} + \frac{1}{\eta_{\text{btm}}(\theta)}} \quad (117)$$

By substituting the relations in eqs. (47) and (49) in eq. (117), one can get an expression for $k_{\text{unc}}(\theta)$ for an infinite QPD depending explicitly on the beam parameters:

$$k_{\text{unc}}^{-1}(\theta) = \frac{1}{\sqrt{1 + \rho^2}} \frac{2w_r w_m}{w_r^2 + w_m^2} \exp\left(-\frac{k^2 w_{\text{eff}}^2 \theta^2}{8(1 + \rho^2)}\right) \sqrt{\frac{(1 + |\alpha|^2)^2 - 4(\text{Im}[\alpha])^2}{1 + |\alpha|^2}}, \quad (118)$$

where, for convenience, the quantity

$$\alpha = \operatorname{erfi} \left(\frac{k w_{\text{eff}} \theta}{2^{\frac{3}{2}} \sqrt{1 - i\rho}} \right) \quad (119)$$

was defined. As eq. (118) shows, even though we define the quantity $k_{\text{unc}}(\theta)$ as the coupling coefficient, its reciprocal is much easier to handle. Furthermore, as it resembles the HE, $k_{\text{unc}}^{-1}(\theta)$ can easily be compared to the HE of a QPD-segment on a plot.

The *QPD-signal tilt-coupling coefficient for uncorrelated noises* $k_{\text{unc}}(\theta)$ captures the whole angular dependence of the uncorrelated noise sources affecting the QPD; it depends, of course, on the angle θ , as well as on all the geometrical parameters used to calculate the HE. The dependency of $k_{\text{unc}}^{-1}(\theta)$ on the interferometric configuration's geometric parameters is similar to that of the HE; however the term in the square root gives additional relevance to the effective-spot-radius-normalized wavefront curvature mismatch ρ . On top of the already argued decrease of the HE due to wavefront curvature mismatch, $k_{\text{unc}}(\theta)$ also takes into account that, if $\rho \neq 0$ and in the presence of a tilt, the heterodyne efficiencies of the individual QPD segments take different values. This implies, looking at Figure 8, that the phase noise of the QPD segments with the lowest HE will contribute more to the overall phase noise than those with the highest HE. Such an effect becomes more noticeable when ρ takes particularly large values, such as $\rho = 0.6$.

As a function, $k_{\text{unc}}^{-1}(\theta) \in [0, 1]$ as the HE. It must be symmetric about $\theta = 0$ even in the presence of a wavefront curvature mismatch, and must therefore have a maximum at $\theta = 0$. Note that $\theta = 0$ implies $\alpha = 0$, hence the argument of the square root in eqs. (47) and (49) is zero and the expression simplifies to the HE of an infinite SEPD at $\theta = 0$, or $k_{\text{unc}}^{-1}(\theta = 0) = \sqrt{\eta_{\text{hetSEPD}}(\theta = 0)}$. Also, in the case of $\rho = 0$, this implies $\operatorname{Im}[\alpha] = 0$, and hence eq. (117) simplifies to the HE of an infinite QPD reported in eq. (54).

A plot of $k_{\text{unc}}^{-1}(\theta)$ for an infinite QPD is shown in Figure 25 for four values of the effective-spot-radius-normalized wavefront curvature mismatch parameter ρ . This plot shows that $k_{\text{unc}}^{-1}(\theta)$ is very close to the whole-QPD HE $\sqrt{\eta_{\text{hetQPD}, \infty}(\theta)}$, and the two are identical for $\rho = 0$. On the other hand, $k_{\text{unc}}^{-1}(\theta)$ is very different from the HE of a SEPD; therefore, we stress that the modelling of phase readout noise in LISA must treat QPD segments separately. An increase of ρ causes, together with a higher coupling due to a decrease of the maximum achievable HE, a small discrepancy to arise between the whole-QPD HE and $k_{\text{unc}}^{-1}(\theta)$. Figure 25 evidences how, in the presence of an effective-spot-radius-normalized wavefront curvature mismatch of $\rho = 0.6$, even in the absence of tilts, $k_{\text{unc}}^{-1}(\theta = 0)$ is at most 0.857. This corresponds to an increase in the uncorrelated noise coupling of $\sim 16.7\%$. To the LISA collaboration's knowledge, the highest expected value of ρ in LISA's interferometers is $\rho = 0.469$ [26, Table III]; if LISA was to be built in such configuration, this would cause an increase of interferometric readout phase noise of $\sim 10\%$. This could be easily avoided by better mode matching the beams in both the TMI and SCI. Furthermore, in Figure 25d, one can see how, at a tilt angle of ± 0.5 mrad, $k_{\text{unc}}^{-1}(\theta)$ is relatively $\sim 8\%$ lower than the whole-QPD HE, implying increased noise coupling in a tilt range likely to happen in LISA.

6.3 Correlated noises

The relative intensity variations in the laser beams influence all QPDs and QPD-segments in the same way; therefore, RIN are correlated among the segments of a QPD [40]. A similar argument can be made for straylight, as long as this impinges identically on all segments of the QPD; as this is not a general case, we leave this out and focus solely on RIN.

The phase noise for summation and subtraction of perfectly correlated phase noises is derived in Section A in eq. (146), and is given in eqs. (120) and (121)

$$\tilde{\phi}_{\text{AP, cor}}(\theta) = \frac{1}{2} \sqrt{\tilde{\phi}_{\text{top}}^2(\theta) + \tilde{\phi}_{\text{btm}}^2(\theta) + 2\tilde{\phi}_{\text{top}}(\theta)\tilde{\phi}_{\text{btm}}(\theta) \cos(\tilde{\phi}_{\text{top}}(\theta) - \tilde{\phi}_{\text{btm}}(\theta))}, \quad (120)$$

$$\widetilde{\text{DWS}}_{\text{cor}}(\theta) = \sqrt{\tilde{\phi}_{\text{top}}^2(\theta) + \tilde{\phi}_{\text{btm}}^2(\theta) - 2\tilde{\phi}_{\text{top}}(\theta)\tilde{\phi}_{\text{btm}}(\theta) \cos(\tilde{\phi}_{\text{top}}(\theta) - \tilde{\phi}_{\text{btm}}(\theta))}, \quad (121)$$

where $\tilde{\phi}$ is the average phase, defined assuming that $\tilde{\phi} \ll 2\pi$. Note that it depends also on the difference of the average phases: $\tilde{\phi}_{\text{AP, cor}}$ is minimum if $\tilde{\phi}_{\text{top}} - \tilde{\phi}_{\text{btm}} = \pi + 2n\pi$, while $\widetilde{\text{DWS}}_{\text{cor}}$ is minimum for $\tilde{\phi}_{\text{top}} - \tilde{\phi}_{\text{btm}} = 0 + 2n\pi$, $n \in \mathbb{Z}$.

As a general experimental remark, note that the average phases are the resulting phases at the output of the measurement chain. They, therefore, include also eventual phase offsets originating along the analog- and phasemeter-signal processing of each QPD segment. As these chains generally present slightly different phase TFs, this results in different phase outputs for the same optical input. Such issue is related to the DWS-bias mentioned in [25, Figure 3.18]. Such biases are, for simplicity, neglected in this model, and only average phase variations due to beam tilt and QPD geometry are considered. With this assumption, the average phase difference $\tilde{\phi}_{\text{top}}(\theta) - \tilde{\phi}_{\text{btm}}(\theta)$ that appears as the argument of the cosine is simply the vertical DWS signal introduced in eq. (115). This can therefore be expressed as a function of the beam's tilt as demonstrated in [26, eqs. (29, 30)], provided that the tilt is sufficiently small. We name this quantity $\text{DWS}(\theta)$.

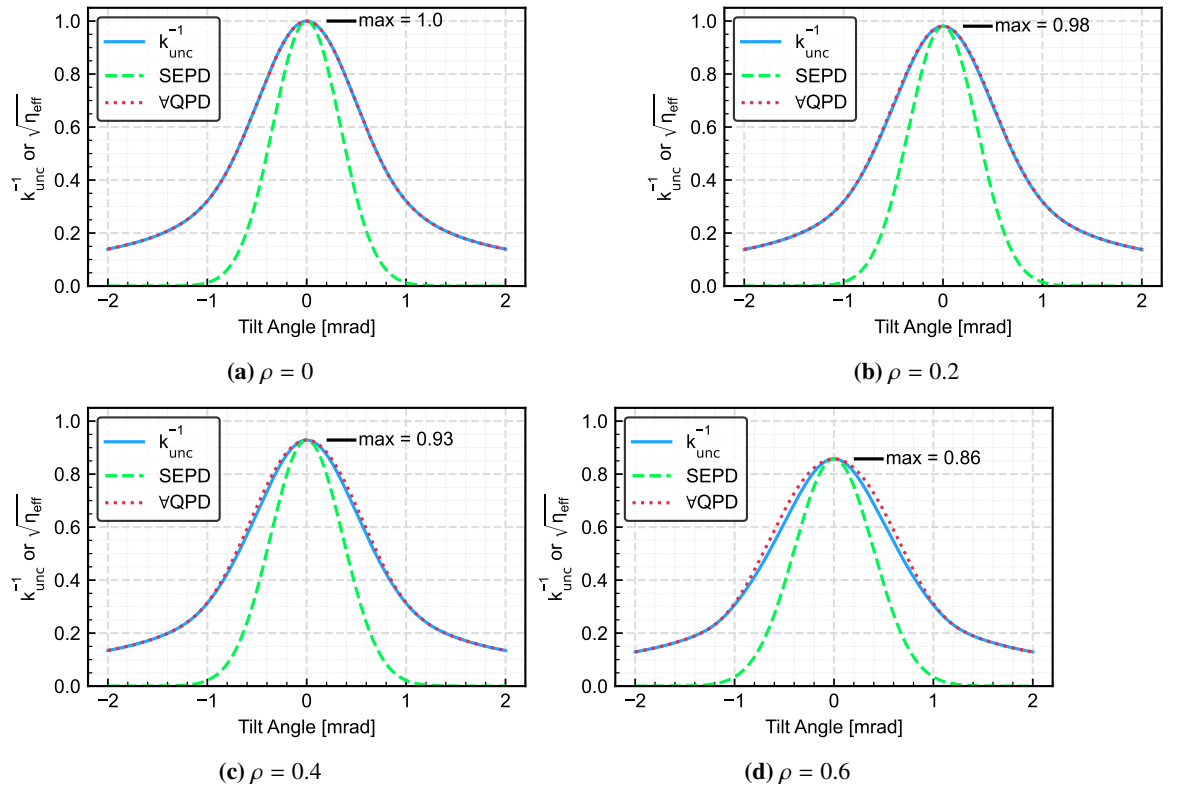


Figure 25: Plot of the reciprocal of QPD-signal tilt-coupling coefficient for uncorrelated noises in eq. (117) for an infinite QPD as a function of the beam tilt, compared with the HEs of an infinite SEP in eq. (41) and the whole-QPD HE of an infinite $\sqrt{\eta_{\text{hetVQPD},\infty}}$ QPD in eq. (59). The used beam parameters are $w_r = w_m = w_{\text{eff}} = 1$ mm, and an infinite QPD radius, and four different values of the effective-spot-radius-normalized wavefront curvature mismatch parameter ρ . This function is meant to capture the entire angular dependence of the uncorrelated noise sources affecting the QPD signals. Note that a smaller value of $k_{\text{unc}}^{-1}(\theta)$ corresponds to a higher noise coupling.

By expressing eqs. (120) and (121) using the $\Upsilon_{\text{RIN-1}f}$ parameter defined in eq. (112), the average phase noise and DWS noise can be rewritten as

$$\tilde{\phi}_{\text{AP, cor}}(\theta) = \frac{1}{2} \Upsilon_{\text{RIN-1}f} \sqrt{2} k_{\text{cor, } \Sigma}(\theta), \quad (122)$$

$$k_{\text{cor, } \Sigma}(\theta) = \frac{1}{\sqrt{2}} \sqrt{\frac{1}{\eta_{\text{top}}(\theta)} + \frac{1}{\eta_{\text{btm}}(\theta)} + \frac{2}{\sqrt{\eta_{\text{top}}(\theta)\eta_{\text{btm}}(\theta)}} \cos(\text{DWS}(\theta))}, \quad (123)$$

$$\widetilde{\text{DWS}}_{\text{cor}}(\theta) = \Upsilon_{\text{RIN-1}f} \sqrt{2} k_{\text{cor, } \Delta}(\theta), \quad (124)$$

$$k_{\text{cor, } \Delta}(\theta) = \frac{1}{\sqrt{2}} \sqrt{\frac{1}{\eta_{\text{top}}(\theta)} + \frac{1}{\eta_{\text{btm}}(\theta)} - \frac{2}{\sqrt{\eta_{\text{top}}(\theta)\eta_{\text{btm}}(\theta)}} \cos(\text{DWS}(\theta))}, \quad (125)$$

where the *QPD-signal tilt-coupling coefficient for correlated noise for sum* $k_{\text{cor, } \Sigma}(\theta)$ and *difference* $k_{\text{cor, } \Delta}(\theta)$ were introduced in eqs. (123) and (125), respectively.

By substituting the relations in eqs. (47) and (49) in eqs. (123) and (125), one can get an expression for $k_{\text{cor, } \Sigma/\Delta}^{-1}(\theta)$ for an infinite QPD depending explicitly on the beam parameters:

$$k_{\text{cor, } \Sigma/\Delta}^{-1}(\theta) = \frac{1}{\sqrt{1 + \rho^2}} \frac{2w_r w_m}{w_r^2 + w_m^2} \exp\left(-\frac{k^2 w_{\text{eff}}^2 \theta^2}{8(1 + \rho^2)}\right) \sqrt{\frac{(1 + |\alpha|^2)^2 - 4(\text{Im}[\alpha])^2}{1 + |\alpha|^2 \pm \sqrt{(1 + |\alpha|^2)^2 - 4(\text{Im}[\alpha])^2} \cos(\text{DWS}(\theta))}}, \quad (126)$$

where the + and the - are meant to be used for sum and difference, respectively.

As the QPD-signal tilt-coupling coefficient for uncorrelated noises, these two functions capture the whole angular dependence of the correlated noise sources affecting the QPD readout, which in this case comprises both the angular variation of the HE and noise correlation between the QPD-segments. Equations (123) and (125) are rather complicated, and further complex than eq. (117).

We now take a closer look at two particular situations of the derived coupling coefficient. The two coupling factors greatly simplify if either there is perfect beam mode-matching $\rho = 0$, or in the case of no tilt $\theta = 0$. In the first case, the HEs of both the top and bottom segments coincident; we hence define $\sqrt{\eta_{\text{hetQPD, top}}(\theta, \rho = 0)} = \sqrt{\eta_{\text{hetQPD, btm}}(\theta, \rho = 0)} = \sqrt{\eta_{\text{hetQPD}}(\theta)}$. Furthermore, for an infinite QPD, $\text{Im}[\alpha] = 0$, and eq. (126) simplifies to

$$k_{\text{cor, } \Sigma/\Delta}^{-1}(\theta) = \frac{2w_r w_m}{w_r^2 + w_m^2} \exp\left(-\frac{k^2 w_{\text{eff}}^2 \theta^2}{8}\right) \sqrt{\frac{1 + \alpha^2}{1 \pm \cos(\text{DWS}(\theta))}}, \quad (127)$$

while $k_{\text{cor, } \Sigma/\Delta}^{-1}(\theta)$, for a generic size QPD, simplify to

$$k_{\text{cor, } \Sigma}(\theta) = \frac{\sqrt{2}}{\sqrt{\eta_{\text{hetQPD}}(\theta)}} \cos\left(\frac{1}{2}\text{DWS}(\theta)\right), \quad (128)$$

$$k_{\text{cor, } \Delta}(\theta) = \frac{\sqrt{2}}{\sqrt{\eta_{\text{hetQPD}}(\theta)}} \sin\left(\frac{1}{2}\text{DWS}(\theta)\right), \quad (129)$$

in accordance with the result in [40, eq. (51)] and [42, eqs. (4-7)]. In the second case, for $\theta = 0 \rightarrow \alpha = 0$ this results, independently of ρ , in

$$k_{\text{cor, } \Sigma}(\theta = 0) = \frac{\sqrt{2}}{\sqrt{\eta_{\text{hetQPD}}(\theta = 0)}}, \quad (130)$$

$$k_{\text{cor, } \Delta}(\theta = 0) = 0, \quad (131)$$

where we remind that $\text{DWS}(\theta = 0) = 0$ [26].

A plot of $k_{\text{cor, } \Sigma}^{-1}(\theta)$ and $k_{\text{cor, } \Delta}^{-1}(\theta)$ for an infinite QPD is shown in Figure 26. As one can see, these functions present a fundamental difference with respect to the QPD-signal tilt-coupling coefficient for uncorrelated noises: they diverge at some specific tilt values. This is due to the fact that at those specific angles, these noises are anticorrelated and therefore cancel each other out. At such angles, the coupling of the correlated noise sources tends to zero, and therefore $k_{\text{cor, } \Sigma/\Delta}^{-1}(\theta)$ tend to infinity.

A plot of the two functions $k_{\text{cor, } \Delta}^{-1}(\theta)$ and $k_{\text{cor, } \Sigma}^{-1}(\theta)$ is shown in Figures 26a and 26b, respectively, for four values of the effective-spot-radius-normalized wavefront curvature mismatch parameter ρ . These two manifest opposite angular behaviour, as $k_{\text{cor, } \Delta}^{-1}(\theta)$ diverges for $\theta = 0$, whereas $k_{\text{cor, } \Sigma}^{-1}(\theta)$ diverges for $\theta = \pm\pi$. LISA operates close to $\theta = 0$, meaning that RIN has a very small coupling to the DWS signal, while there is

little to no mitigation for the LPS. In particular, a value of $\rho = 0.6$ causes an increase of 16.6% in the correlated noise in comparison to the case $\rho = 0$, a situation close to that of the QPD-signal tilt-coupling coefficient for uncorrelated noises $k_{\text{unc}}^{-1}(\theta)$. Furthermore, a higher value of ρ broadens the angular range where $k_{\text{cor},\Sigma}^{-1}(\theta)$ does not diverge, effectively increasing the noise coupling in the whole operational angular range. In Figure 26b, $k_{\text{cor},\Delta}^{-1}(\theta)$ is less affected by the presence of an effective-spot-radius-normalized wavefront curvature mismatch. Still, this causes a higher coupling of correlated noise sources. In general, scenarios with lower ρ manifest lower optical noise.

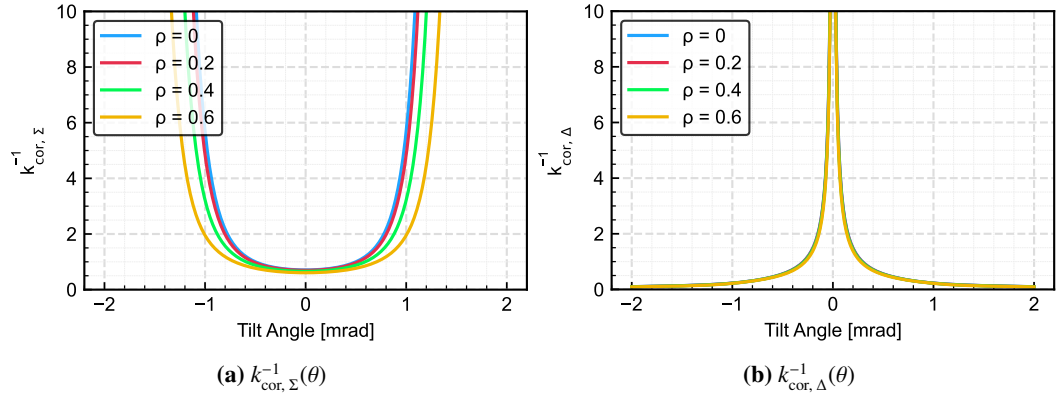


Figure 26: Plot of the reciprocal of the QPD-signal tilt-coupling coefficient for correlated noises for sum $k_{\text{cor},\Sigma}^{-1}(\theta)$ (a) and difference $k_{\text{cor},\Delta}^{-1}(\theta)$ (b) for an infinite QPD from eqs. (123) and (125). The used beam parameters are $w_{\text{eff}} = 1$ mm, and an infinite QPD radius, and four different values of the effective-spot-radius-normalized wavefront curvature mismatch parameter ρ . Note that a smaller value of $k_{\text{cor},\Sigma/\Delta}^{-1}(\theta)$ corresponds to a higher noise coupling; therefore, $k_{\text{cor},\Sigma/\Delta}^{-1}(\theta)$ diverge when the correlated noise are expected to perfectly cancel. This happens at $\theta = 0$ for $k_{\text{cor},\Delta}^{-1}(\theta)$ and roughly at ± 1.2 mrad for $k_{\text{cor},\Sigma}^{-1}(\theta)$ for the parameters used in this plot.

6.4 Total QPD readout noise

Combining together the results of subsections 6.2 and 6.3, the total readout noise of the QPD-signals is recovered in eqs. (132) and (133), where we report this with both θ and f_{het} dependency. The angular dependence of $2f$ -RIN, which does not depend on the HE, is taken from [40, 42]. This final expression is a constructed using the coupling factors mentioned above and the individual phase noises for a single QPD-segment.

$$\tilde{\phi}_{\text{AP}}(f_{\text{het}}, \theta) = \frac{1}{2} \sqrt{2(\Upsilon_{\text{shot}}^2 + \Upsilon_{\text{en}}^2(f_{\text{het}})) k_{\text{unc}}^2(\theta) + 2\Upsilon_{\text{RIN-1f}}^2(f_{\text{het}}) k_{\text{cor},\Sigma}^2(\theta) + 4\tilde{\phi}_{\text{RIN-2f}}^2(f_{\text{het}}) \cos^2(\text{DWS}(\theta))} \quad (132)$$

$$\widetilde{\text{DWS}}(f_{\text{het}}, \theta) = \sqrt{2(\Upsilon_{\text{shot}}^2 + \Upsilon_{\text{en}}^2(f_{\text{het}})) k_{\text{unc}}^2(\theta) + 2\Upsilon_{\text{RIN-1f}}^2(f_{\text{het}}) k_{\text{cor},\Delta}^2(\theta) + 4\tilde{\phi}_{\text{RIN-2f}}^2(f_{\text{het}}) \sin^2(\text{DWS}(\theta))} \quad (133)$$

Equations (123) and (125) state that, in the calculation of the overall readout phase noise of QPD signals as a function of the beam tilt, one must consider the QPD as a whole, as the individual segments manifest different behaviours as a function of the tilt angle. The only exception to this is when $\rho = 0$; then, all segments will present the same HE, as the symmetry presented in Figure 11 is not broken. The functions $k_{\text{unc}}(\theta)$, $k_{\text{cor},\Sigma}(\theta)$, $k_{\text{cor},\Delta}(\theta)$ collect the whole angular dependence of the QPD signals' noise, which is related both to the geometry of the interferometric topology and to the correlation of the noise sources, while the $\Upsilon_{\text{shot/en/RIN-1f}}$ parameters collect the information about beam power and noise magnitude.

In other words, in the case of perfectly matched beams, all segments manifest the same HE for all tilts; one can hence calculate the phase readout noise based solely on the HE of one segment. In the presence of wavefront curvature mismatch, this does not hold anymore, and the phase readout noise cannot be calculated exactly based only on the HE of one single segment. In this scenario, the segments have to be analyzed separately and their individual phase noises combined. We also stress that there is a substantial difference between the phase noise of a QPD's output and that of a SEPD. This is due to their different HEs.

The magnitude of the impact of this novel approach in the phase noise modelling of QPD-signals depends on the value of the wavefront curvature mismatch; for small values of ρ , modelling all segments as having the same HE is indeed a good approximation; otherwise, individual dedicated modelling is to be preferred. A benchmark value of $\rho > 0.2$ can be set to discriminate between these two cases. We further remark that this is a simplified model accounting only for vertical tilts. The predicted noise increase due to

wavefront curvature mismatches becomes more significant in the presence of horizontal tilts, as this further increases the asymmetry between the measured power.

7 LISA noise budget operating with tilted TM

The performance of LISA is affected, among other noises, by the alignment precision of the components on the LOB. Static misalignments that occur during the build of the OB due to the imperfect positioning of optical components lead to departures from the nominal interferometric topology, thereby enhancing additive interferometric noise couplings. Such effects cannot be fully investigated experimentally on ground before the mission, and have to be mitigated in flight.

Let's suppose, for instance, that a static misalignment affects the LO beam in the TMI; this beam impinges at the center of the QPDs, but with a small tilt, of the order of a few tenths of μrad . At the same time, the Tx beam sits in its nominal position, impinging orthogonally on the QPDs. The result is a lower HE, and an enhancement of all HE dependent noise sources.

As the LOB lacks beam-angle correction mechanisms for the LO beam, such an issue cannot be corrected. One possible solution is to make the Tx beam "follow" the misaligned LO beam, thereby recovering an optimal HE. This can be achieved by intentionally tilting the TM, which is the only actuatable mirror on the Tx beam's path. This means operating the TM at a small tilt angle, or the order of a few μrad , such that the Tx beam, reflecting on the TM, is made parallel to the LO beam. Such an operation point is named *DWS-zero*. In contrast, the operation without correction for residual beam tilt is called *DWS-offset*. Such a method improves the optical noise balance, as the HE of the two beams increases; however, it also increases the TTL-coupling, as tilting the TM, which would otherwise sit in its optimal position, couples its lateral jitter into the interferometrically measured LPS. Such an approach was successfully used in LISA-Pathfinder [43, 44], where the maximum tilt of the reference TM tilt was of the order of $60 \mu\text{rad}$ [45, Table VII], translating to a beam tilt of $120 \mu\text{rad}$ at QPD-level.

This section aims to check whether operating at *DWS-zero* is also reasonable for LISA. To answer this question, a detailed comparison of the two noise couplings – additive interferometric noise and TTL coupling – is needed, in order to find the optimal operating point. As we lack the expertise to derive additional TTL coupling due to TM tilt, this section addresses only the optical noise considerations, which are linked to the HE as a function of beam tilt, which was extensively modelled in this article. We hope that the results of this section can help answer the full matter.

We approach this question not by examining how the tilts of the measurement beam affect the interferometric noise in the TMI, which, neglecting QPD tilts, yields a similar answer: the performance degradation that a measurement beam causes due to a tilt is hence assumed to be the improvement that "following" the LO beam's tilt can achieve. We argue that QPD tilts can be neglected as long as the QPD's radius is sufficiently larger than the beams' spot size; we show that this is the case in the TMI.

We estimate here the predicted increase in optical noise at small angles of the Tx beam. Give the tilt range in LISA-Pathfinder, we can hence reasonably suppose a LO beam tilt of the order of $100 \mu\text{rad}$ in LISA, assuming once more only vertical tilts and consequently two QPD halves. First, we characterize the HE of the TMI: this depends on the beam and QPD sizes. These values are reported in [26, Section VI], and are:

- The Gaussian beam's (hence the Tx and LO) parameters lie in the range $0.34 \text{ mm} < w_0 < 0.46 \text{ mm}$ and $|z_0| < 160 \text{ mm}$, with $z_0 = 0 \text{ mm}$ indicating the position of the QPD. The two beams can be considered independent.
- The QPD's diameter is 1.5 mm . There are $20 \mu\text{m}$ gaps between the segments [46]. These gaps are approximately as sensitive as the QPD's active area, hence the QPD can be considered as having no gaps.

From the latest LISA design, a range of possible HEs can be estimated. These can be split into best- and worst-case scenarios using eq. (41). The best-case scenario corresponds to a perfect mode match, hence a minimum value of $|\rho| = 0$ and $w_{\text{Tx}} = w_{\text{LO}}$, and a minimum value of w_{eff} , to minimize the degradation of the HE as a function of the tilt. The worst-case scenario is more difficult to determine, as both the beam-size mismatch and the wavefront-curvature mismatch contribute to degrading the HE. Numerical comparisons show that the wavefront-curvature mismatch is the leading contributor; hence, the worst-case scenario is given by the maximum value of $|\rho| = 0.469$ [26]; such value of ρ is also reached when the waist size w_0 of the two GBs is minimum. The resulting interferometric parameters are listed in Table 4. Note that these best- and worst-case scenarios for the HE do not exactly correspond, but are close, to the best- and worst-case scenarios for the DWS signal reported in [26]. Note that the values of $\beta = \sqrt{2}r_{\text{QPD}}/w_{\text{eff}}$ are relatively large, hence justifying an infinite-QPD approximation. This leads to the HEs plotted in Figure 27 for the two QPD halves.

From these estimations, a theoretical phase noise model can be derived. A comparison between the phase noise in these two cases is shown in Figure 28, which shows the AP and AP-LPS noise on the left, and WFA

Parameter	Unit	Value	
		Best-case	Worst-case
w_{eff}	mm	0.34	0.376
ρ	-	0	0.469
β	-	3.12	2.82

Table 4: Relevant parameters of the TMI's geometry in the best- and worst-case scenarios.

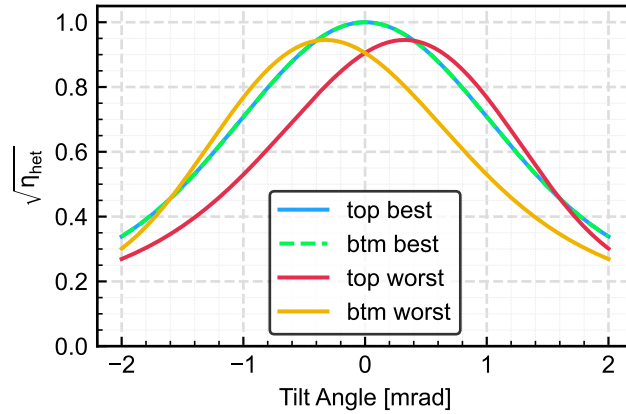


Figure 27: Plot of the best- and worst-case scenario HEs of the TMI in LISA. Note that the x axis is the Tx beam's tilt angle; the TM's angle can be obtained by rescaling the x axis by a factor of $m_{\text{IS}}/2$, where m_{IS} is the magnification of the imaging system in LISA. As previously argued, the top and bottom HEs are coincident in the best-case scenario, as $\rho = 0$.

noise on the right. The noise parameters for LISA, which were used in this calculation, are reported in Table 5.

First, the most noticeable result in Figure 28 is that the WFA noise sharply increases for tilts larger than 1 mrad, due to the reduction of the DWS gain. Secondly, in the absence of tilts, the worst-scenario configuration results in a noise increase of 10.4% in LPS and 7.7% WFA noise; we therefore recommend, once more, good mode matching between the interfering beams. Third, in the tilt range of $\pm 100 \mu\text{rad}$, the noise increase is modest. Tables 6 and 7 quantitatively report the noise increase as a function of the tilt angle for LPS and WFA, respectively.

This result shows that beam tilts of the order of a few μrad cause very modest increases in the noise, with relative performance degradation of the order of one part per thousand. This noise increase corresponds to the improvement that operating at DWS-zero can hope to achieve. In comparison to such a small improvement, the TTL of the TM surely worsens; although this improvement has not been compared with the increase of TTL noise, we think that it is small enough to argue that operation at a DWS offset is preferable. Further checks should still be performed comparing the interferometric and TTL performances.

Experimental measurements of the DWS performance as a function of beam tilt have already been performed in TDOBS and are in the process of publication to consolidate this model.

Parameter	Value	Units
P_{Tx}	1.5×10^{-4}	W
P_{LO}	8.3×10^{-7}	W
η_{PD}	0.93	-
A	0.80	A W^{-1}
$\tilde{i}_{\text{en}}(f_{\text{het}})$	2	$\text{pA/Hz}^{1/2}$
\tilde{r}	3×10^{-8}	$1/\text{Hz}^{1/2}$

Table 5: Parameters of the LISA mission used to calculate the interferometric noise. For simplicity, the electronic noise of the QPR \tilde{i}_{en} is set to be frequency independent and equal to the requirement. Source: [25].

8 Summary and conclusion

Gravitational spaceborne interferometers aim to measure the variation of distance between free-falling TMs with a precision of the order of $\text{pm}/\sqrt{\text{Hz}}$ in the $10^{-4} - 1 \text{ Hz}$ band. Such performance is challenged by the presence of spacecraft and TM jitter. The coupling of the consequent beam jitter into the interferometrically

Tilt Angle [μrad]	Best-case scenario		Worst-case scenario	
	LPS noise [$\text{pm}/\text{Hz}^{1/2}$]	Relative Increase	LPS noise [$\text{pm}/\text{Hz}^{1/2}$]	Relative Increase
5	3.2633×10^{-1}	8.4304×10^{-6}	3.6043×10^{-1}	1.0033×10^{-5}
10	3.2634×10^{-1}	3.3722×10^{-5}	3.6044×10^{-1}	4.0133×10^{-5}
20	3.2637×10^{-1}	1.3489×10^{-4}	3.6048×10^{-1}	1.6054×10^{-4}
50	3.2660×10^{-1}	8.4338×10^{-4}	3.6079×10^{-1}	1.0036×10^{-3}
100	3.2743×10^{-1}	3.3777×10^{-3}	3.6187×10^{-1}	4.0180×10^{-3}

Table 6: AP-LPS noise and relative noise increase as a function of the beam tilt angle for LISA's TMI. This calculation is based on eq. (132), using the parameters in Table 4 for the best- and worst-case scenarios, and on Table 5 for the TMI's parameters. These values in the table correspond to Figure 28a. The relative noise increase is stated with respect to the no-tilt case.

Tilt Angle [μrad]	Best-case scenario		Worst-case scenario	
	WFA noise [$\text{nrad}/\text{Hz}^{1/2}$]	Relative	WFA noise [$\text{nrad}/\text{Hz}^{1/2}$]	Relative
5	8.3153×10^{-1}	1.6796×10^{-5}	8.9543×10^{-1}	1.7825×10^{-5}
10	8.3157×10^{-1}	6.7186×10^{-5}	8.9548×10^{-1}	7.1300×10^{-5}
20	8.3174×10^{-1}	2.6877×10^{-4}	8.9567×10^{-1}	2.8522×10^{-4}
50	8.3292×10^{-1}	1.6810×10^{-3}	8.9701×10^{-1}	1.7837×10^{-3}
100	8.3712×10^{-1}	6.7353×10^{-3}	9.0181×10^{-1}	7.1451×10^{-3}

Table 7: WFA noise and relative noise increase as a function of the beam tilt angle for LISA's TMI. This calculation is based on eq. (133), using the parameters in Table 4 for the best- and worst-case scenarios, and on Table 5 for the TMI's parameters. The values in the table correspond to Figure 28b. The relative noise increase is stated with respect to the no-tilt case.

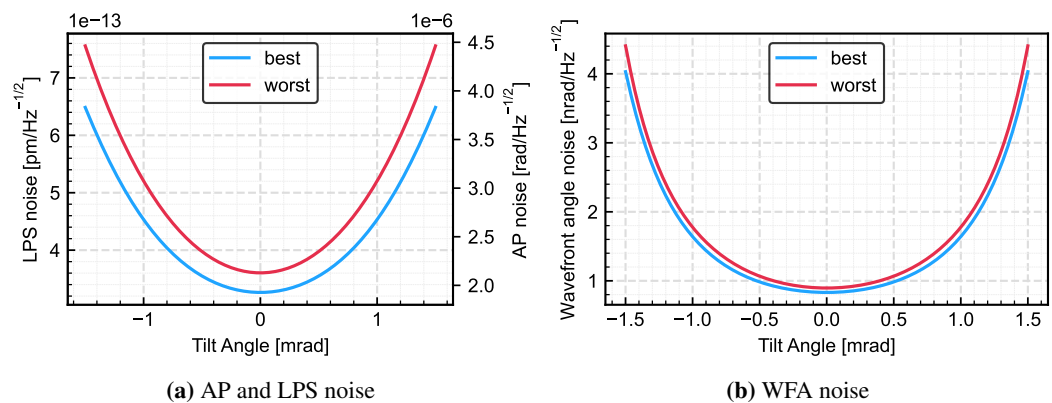


Figure 28: Calculated LPS and WFA noise as a function of the Tx beam's tilt angle for the TMI in LISA. These curves are based on equations eqs. (132) and (133), which assume an infinite QPD. This approximation is justified by the values of β in Table 4, which are larger enough than one. The used noise input parameters are reported in Table 5. Figure 28a also reports the AP noise on a second y-axis; this is easily done, as the two y-axis are linearly related. The same does not hold for DWS and WFA. In fact, note that the WFA noise rapidly increases for tilts larger than 1 mrad, as the DWS gain tends to zero.

measured pathlength is an extremely relevant aspect in spaceborne interferometers such as LISA. To mitigate this issue, while also ensuring constellation and TM alignment, LISA is implementing an angular readout using a technique named DWS. This technique, which requires the use of QPDs, enables LISA to both actively control the tilts of the TM and subtract the spurious pathlength contributions due to the tilt in post-processing. Therefore, the success of the mission depends on the achieved sensitivity not only of the LPS, but also of DWS, with a target of $\text{nrad}/\sqrt{\text{Hz}}$.

Such sensitivity is significantly affected by the dynamics we expect in LISA. The TMI and SCI measurement beams undergo tilts of up to 1 mrad at the QPD, causing a drop in the HE of up to a factor of five. This reduces the amplitude of the measured signal, consequently decreasing SNR and increasing readout noise. A correct modelling of how the HE is affected by tilts is hence crucial to understand the range of tilt motion that can be tolerated whilst maintaining performance.

In this paper, an approximated analytic description of the HE is proposed in Section 3. The resulting expression is capable of analytically deriving the HE of two beams impinging on infinite SEPDS and QPDs, and to analytically derive the first few Maclaurin expansion coefficients of the HE of two beams impinging on a finite PDs. The references to the derived expressions are collected in Table 8. The resulting HEs derived by this model are compared to numerical integration, achieving excellent results for small wavefront curvature mismatches. The derivation is general, and can be used to estimate the beam overlap in any interferometric topology featuring beam tilts around the detector's center. These results are applicable to any interferometer, although the models are most relevant for spaceborne interferometers. In particular, the model developed in this paper predicts that, for two beams interfering on a QPD, in the presence of a wavefront curvature mismatch, the HE measured by the individual segment differs; such a feature is reported for the first time in this work.

In Section 4, we derived how the use of imaging systems affects the HE. In Section 5, this model is finally compared to a HE measurement performed on an ultra-stable testbed described in Section 2. These experimental results confirm the prediction of the model.

In Section 6, the HE model is used to derive the behaviour of the interferometric readout noise of the QPD-signals as a function of the beam tilt. In this context, the noise sources remain constant, whereas the signal amplitude degrades; due to the decrease in SNR, the phase noise increases solely as a result of the decrease in HE. The QPD signals' readout noise is analyzed in a simplified model which uses only vertical tilts and only two segments. This model, albeit simplified, is able to grasp a new feature of the QPD readout, which is induced by the prediction of the analytic HE model: in the presence of wavefront curvature mismatches, tilts affect the HE of the two segments differently, leading to different SNRs and additive noise couplings between the two segments. This results in an increase in readout noise compared to a situation where such a difference is neglected. Therefore, in light of such considerations, the QPD must be treated as a whole. A general conclusion of this article is to minimize the mode mismatch between the beams in order to improve SNR.

In Section 7, we calculate the possible benefits of intentionally tilting the TM in the TMI to correct for build imperfections of the LOB. A realignment of the TM can reduce interferometric noise coupling, at the cost of increasing the coupling of the TM's lateral jitter to the measured LPS. We estimate the magnitude of the possible interferometric noise mitigation using the models developed in Section 3, which have to be compared to the TTL noise increase to obtain an ultimate answer. However, this leads, in our opinion, to negligible gains in interferometric noise. Experimental results confirming this claim are in the process of publication.

We see several possibilities for further expansion and use of this work, which would benefit the LISA mission, future space interferometers add potentially also any interferometer. For instance, a good model of the amplitudes of LISA's interferometric signals can also be used, either in postprocessing or in the phasemeter, to monitor and correct for cycle slips in the phasemeter [47, chapter 4]. These occur in the DPLL when the magnitude of the phase error exceeds 0.5 cycles, driving the loop to find stability one or more cycles apart. In such a case, the phase output of the phasemeter is subject to a jump of $2\pi n$ with $n \in \mathbb{Z}$. This jump would carry over to the LPS and DWS signals, being interpreted as a sudden change in pathlength or beam angle, respectively. As we have demonstrated during this article, a real beam tilts also implies a change of HE². Counter-checking variations of signal amplitude can hence be used to discriminate between real and cycle-slip-originated phase changes. A second use of a HE model would be to combine it with the DWS signal. As demonstrated in [26], the DWS signal is a very powerful QPD-signal for monitoring the beam tilt-angle. This technique, however, has a limited range due to the finite size of the used QPDs and the inevitable presence of wavefront curvature mismatches. These cause the DWS signal to *wrap* and invert its sign, as soon as it crosses $\pm\pi$ (see [26, Figure 11]). This can also occur for relatively small tilts. On the other hand, the HE is not subject to periodic jumps, as it is not a phase measurement. Combining the two quantities can, therefore, broaden the range of operation of the DWS signal beyond its first wrapping.

²This is true, unless the tilt simply swaps the sign of the resulting beam angle

The model used in this article considers simply two beams, either a pair of GBs or a GB-TH beam couple. Any interferometer using such beam pairs which is subject to tilts around the detector's center might find this work useful to evaluate the amplitude of the resulting signal. Future space interferometers can benefit from this work to improve their design.

We hope that this model will be beneficial not only to the space-borne interferometry community but also to any optics experiments that are subject to beam tilts.

Beams	Quantity	SEPD		QPD	
		infinte	finite	infinite	finite
GB-GB	$\sqrt{\eta_{\text{het}}}$	eq. (41) Figure 7	eq. (147) Figures 13 to 15	eqs. (47) and (49) Figure 8	eq. (148) Figures 16 and 17
	ψ_{het}	eq. (42)	not calculated	eqs. (48) and (50)	not calculated
GB-TH	$\sqrt{\eta_{\text{het}}}$	eq. (69)	eq. (147) adjusted with eqs. (91) and (92) Figures 18 and 19	eq. (70)	eq. (148) adjusted with eqs. (91) and (92)
	ψ_{het}	eq. (42)	not calculated	eqs. (48) and (50)	not calculated

Table 8: Summary of the analytical results derived in this work for the HE and heterodyne phase shift. The main assumption of the analytical framework is that the beam tilts on the PD are sufficiently small to allow linearization of the resulting electric field, performed between eq. (18) and eq. (19). The resulting intensity is integrated over circular PDs of either infinite or finite radius, leading to the results in this table, which are calculated either for a GB-GB or GB-TH beam interference. These cases are representative of the TMI and SCI in LISA. Both $\sqrt{\eta_{\text{het}}}$ and ψ_{het} depend on θ , w_{eff} , r_{QPD} . An GB-GB interferometric topology can be considered to have an infinite PD if $\beta = \sqrt{2}r_{\text{QPD}}/w_{\text{eff}} > 3$ (see Figures 15 and 17). The GB-TH case can realistically be treated only in the finite PD case. Stating such a rule, in general, for an GB-TH interferometric topology is less trivial; cases with relatively high HE must be described with a finite PD size.Z

Acknowledgements

We gratefully acknowledge support by the Deutsches Zentrum für Luft- und Raumfahrt (DLR) with funding of the Bundesministerium für Wirtschaft und Klimaschutz with a decision of the Deutsche Bundestag (DLR Project Reference No. FKZ 50 OQ 1801) and FKZ 50OQ2301. Additionally, we acknowledge funding by the European Space Agency within the project ‘‘Optical Bench Development for LISA’’ (22331/09/NL/HB), support from UK Space Agency, University of Glasgow, Scottish Universities Physics Alliance (SUPA).

*

A Correlated Phase Noises

We derive expressions for the ASDs of the sum and the difference of two potentially correlated noise contributions with arbitrary amplitudes and a specified relative phase or delay. The derivation follows [48] and begins with the standard Fourier-domain definitions of auto- and cross-power spectral densities and coherence, ultimately leading to compact formulas that explicitly include the phase offset.

A.1 Setup and Definitions

Let $x(t)$ and $y(t)$ be (wide-sense) stationary, zero-mean random processes. We hence define the Fourier transforms $X_T(f)$ and $Y_T(f)$ of these processes over a finite time period $[0, T]$ as:

$$X_T(f) = \int_0^T x(t)e^{-i2\pi ft} dt, \quad (134)$$

$$Y_T(f) = \int_0^T y(t)e^{-i2\pi ft} dt \quad (135)$$

We use eqs. (134) and (135) to define the power spectral densities (PSDs), in the limit that $T \rightarrow \infty$, to approach the underlying processes' properties. The one-sided auto- and cross-power spectral densities $G_{\cdot\cdot}(f)$, for $x(t)$ and $y(t)$, are defined from the noise processes' ensemble averages in the aforementioned limit (following [48, chapter 5]),

$$G_{xx}(f) = 2 \lim_{T \rightarrow \infty} \frac{1}{T} \mathbb{E}\{X_T^*(f)X_T(f)\}, \quad (136)$$

$$G_{yy}(f) = 2 \lim_{T \rightarrow \infty} \frac{1}{T} \mathbb{E}\{Y_T^*(f)Y_T(f)\}, \quad (137)$$

$$G_{xy}(f) = 2 \lim_{T \rightarrow \infty} \frac{1}{T} \mathbb{E}\{X_T^*(f)Y_T(f)\}. \quad (138)$$

Here, $\mathbb{E}\{\cdot\}$ is the expectation value operator. The one-sided cross-power spectral density $G_{xy}(f)$ can be expressed in polar form as

$$G_{xy}(f) = |G_{xy}(f)|e^{-i\theta_{xy}(f)}, \quad 0 < f < \infty, \quad (139)$$

with magnitude factor $|G_{xy}(f)|$ and $\theta_{xy}(f)$ as the relative phase between x and y at frequency f . Further, the coherence squared function is (as defined in [48, eq. (5.90)])

$$\gamma_{xy}^2(f) = \frac{|G_{xy}(f)|^2}{G_{xx}(f)G_{yy}(f)}, \quad (140)$$

where $0 \leq \gamma_{xy}(f) \leq 1$ is the magnitude of the coherence at frequency f .

A.2 Sum and Difference Processes

We define the sum and difference processes as

$$z_{\pm}(t) = x(t) \pm y(t), \quad (141)$$

and their corresponding (and existing) time-limited Fourier domain expressions (as given by eq. (134))

$$Z_{\pm,T}(f) = X_T(f) \pm Y_T(f). \quad (142)$$

This gives the following expression by direct expansion and linearity of the expectation operator in the Fourier domain for the corresponding spectral density, $G_{z_{\pm}z_{\pm}}(f)$,

$$\begin{aligned} G_{z_{\pm}z_{\pm}}(f) &= 2 \lim_{T \rightarrow \infty} \frac{1}{T} \mathbb{E}\{Z_{\pm,T}^*(f)Z_{\pm,T}(f)\} \\ &= G_{xx}(f) + G_{yy}(f) \pm (G_{xy}(f) + G_{yx}(f)) \\ &= G_{xx}(f) + G_{yy}(f) \pm 2 \operatorname{Re}[G_{xy}(f)]. \end{aligned} \quad (143)$$

This identity is a (slightly expanded) standard property of power spectra for linear combinations as given as an example in [48, 5.7]. Using eq. (139) and the definition of the coherence function, eq. (140),

$$\begin{aligned} \operatorname{Re}[G_{xy}(f)] &= |G_{xy}(f)| \cos(\theta_{xy}(f)) \\ &= \gamma_{xy}(f) \sqrt{G_{xx}(f)G_{yy}(f)} \cos(\theta_{xy}(f)). \end{aligned} \quad (144)$$

Equation (143) then leads to the following general form; the one-sided power spectral density for the sum and difference processes,

$$\begin{aligned} G_{z_{\pm}z_{\pm}}(f) &= G_{xx}(f) + G_{yy}(f) + \\ &\quad \pm 2\gamma_{xy}(f) \sqrt{G_{xx}(f)G_{yy}(f)} \cos(\theta_{xy}(f)). \end{aligned} \quad (145)$$

A.3 Amplitude spectral densities

As we often work with ASDs, we define $\tilde{n}_x(f) = \sqrt{G_{xx}(f)}$ and $\tilde{n}_y(f) = \sqrt{G_{yy}(f)}$. The ASDs of the sum and difference, $\tilde{n}_{\pm}(f) = \sqrt{G_{z_{\pm}z_{\pm}}(f)}$, follow from eq. (145) (dropping the indices for the coherence and phase factor):

$$\tilde{n}_{\pm}(f) = \sqrt{\tilde{n}_x^2(f) + \tilde{n}_y^2(f) \pm 2\gamma(f)\tilde{n}_x(f)\tilde{n}_y(f) \cos(\theta(f))}. \quad (146)$$

Equation (146) is the desired result used in this work. It reduces to common special cases (dropping the explicit frequency dependency):

Fully coherent case ($\gamma = 1$) $\tilde{n}_{\pm} = \sqrt{\tilde{n}_x^2 + \tilde{n}_y^2 \pm 2\tilde{n}_x\tilde{n}_y \cos(\theta)}$.

In phase $\theta = 0$ $\tilde{n}_+ = |\tilde{n}_x + \tilde{n}_y|$, $\tilde{n}_- = |\tilde{n}_x - \tilde{n}_y|$.

Anti-phase $\theta = \pi$ $\tilde{n}_+ = |\tilde{n}_x - \tilde{n}_y|$, $\tilde{n}_- = \tilde{n}_x + \tilde{n}_y$.

Quadrature $\theta = \pi/2$ $\tilde{n}_+ = \tilde{n}_- = \sqrt{\tilde{n}_1^2 + \tilde{n}_2^2}$ (same as uncorrelated).

Uncorrelated noises ($\gamma = 0$) $\tilde{n}_{\pm} = \sqrt{\tilde{n}_x^2 + \tilde{n}_y^2}$ (the usual root squared sum).

$$\begin{aligned}
 \sqrt{\eta_{\text{het, SEPD}, \circ}} &= \sqrt{\eta_{\text{het}, 0}} \left(\sum_{i=0}^6 t_i \theta^i \right) + \mathcal{O}(\theta^8) \\
 \sqrt{\eta_{\text{het}, 0}} &= \frac{1}{\sqrt{1 + \rho^2}} \frac{2w_r w_m}{w_r^2 + w_m^2} \frac{1}{\sqrt{1 - \exp(-\beta_r^2)} \sqrt{1 - \exp(-\beta_m^2)}} \\
 t_0 &= \sqrt{1 - 2e^{-\beta^2} \cos(\beta^2 \rho) + e^{-2\beta^2}} \\
 t_2 &= \frac{(kw_{\text{eff}})^2 \left(1 - (2 + \beta^2(1 + \rho^2)) \cos(\beta^2 \rho) e^{-\beta^2} + (1 + \beta^2(1 + \rho^2)) e^{-2\beta^2} \right)}{8(1 + \rho^2) \left(1 - 2e^{-\beta^2} \cos(\beta^2 \rho) + e^{-2\beta^2} \right)^{\frac{3}{2}}} \\
 t_4 &= \frac{(kw_{\text{eff}})^4}{128(1 + \rho^2)^2 \left(1 - 2e^{-\beta^2} \cos(\beta^2 \rho) + e^{-2\beta^2} \right)^{\frac{3}{2}}} \left(\sum_{n=0}^4 e^{-n\beta^2} \tau_n \right) \\
 \tau_0 &= 1 \\
 \tau_1 &= -\frac{1}{2} \cos(\beta^2 \rho) \left(8 + \beta^2(1 + \rho^2)(2 + \beta^2(1 + \rho^2)) \right) - \sin(\beta^2 \rho) \beta^2 \rho(1 + \rho^2) \\
 \tau_2 &= 4 + \frac{1}{2} \beta^2(1 + \rho^2)(4 + 3\beta^2(1 + \rho^2)) + (2 + \beta^2(1 + \rho^2)) \cos(2\beta^2 \rho) + \\
 &\quad - \beta^2 \rho(1 + \rho^2) \sin(2\beta^2 \rho) \\
 \tau_3 &= -\frac{1}{2} \left(8 + 3\beta^2(1 + \rho^2)(2 + \beta^2(1 + \rho^2)) \right) \cos(\beta^2 \rho) - \beta^2 \rho \sin(\beta^2 \rho) \\
 \tau_4 &= 1 + \beta^2(1 + \rho^2) \frac{1}{2} \beta^4(1 + \rho^2)^2 \\
 t_6 &= \frac{(kw_{\text{eff}})^6}{9216(1 + \rho^2)^3 \left(1 - 2e^{-\beta^2} \cos(\beta^2 \rho) + e^{-2\beta^2} \right)^{\frac{3}{2}}} \left(\sum_{n=0}^6 e^{-n\beta^2} \tau_n \right) \\
 \tau_0 &= -12 + \frac{9}{\left(1 - 2e^{-\beta^2} \cos(\beta^2 \rho) + e^{-2\beta^2} \right)^2} \\
 \tau_1 &= \frac{1}{2} \left((48 + \beta^2(1 + \rho^2)(6(7 - \rho^2) + \beta^2(1 + \rho^2)(12 + \beta^2(1 + \rho^2)))) \cos(\beta^2 \rho) + 6\beta^2 \rho(1 + \rho^2)(4 + \beta^2(1 + \rho^2)) \right) \times \\
 &\quad \times \sin(\beta^2 \rho) - \frac{9 \left((12 + \beta^2(1 + \rho^2)(4 + \beta^2(1 + \rho^2))) \cos(\beta^2 \rho) + 2\beta^2 \rho(1 + \rho^2) \sin(\beta^2 \rho) \right)}{2 \left(1 - 2e^{-\beta^2} \cos(\beta^2 \rho) + e^{-2\beta^2} \right)^2} \\
 \tau_2 &= -12 - \beta^2(1 + \rho^2) \left(3(7 - \rho^2) + 5\beta^2(1 + \rho^2) \left(3 + \beta^2(1 + \rho^2) \right) \right) + \frac{9}{4 \left(1 - 2e^{-\beta^2} \cos(\beta^2 \rho) + e^{-2\beta^2} \right)^2} \left(36 + \right. \\
 &\quad \left. + \beta^2(1 + \rho^2)(4 + \beta^2(1 + \rho^2))(6 + \beta^2(1 + \rho^2)) + (2 + \beta^2(1 + \rho^2))(12 + \beta^2(1 + \rho^2)(2 + \beta^2(1 + \rho^2))) \cos(2\beta^2 \rho) + \right. \\
 &\quad \left. 2\beta^2 \rho(1 + \rho^2)(4 + \beta^2(1 + \rho^2)) \sin(2\beta^2 \rho) \right) \\
 \tau_3 &= -\frac{9}{2 \left(1 - 2e^{-\beta^2} \cos(\beta^2 \rho) + e^{-2\beta^2} \right)^2} \left(2 + \beta^2(1 + \rho^2) \right) \left((18 + \beta^2(1 + \rho^2)(9 + 4\beta^2(1 + \rho^2))) \cos(\beta^2 \rho) + \right. \\
 &\quad \left. + 2 \cos(3\beta^2 \rho) + \beta^2(1 + \rho^2) \left(\cos(3\beta^2 \rho) + \rho \left(3 \sin(\beta^2 \rho) + \sin(3\beta^2 \rho) \right) \right) \right) \\
 \tau_4 &= \frac{9}{4 \left(1 - 2e^{-\beta^2} \cos(\beta^2 \rho) + e^{-2\beta^2} \right)^2} \left(36 + \beta^2(1 + \rho^2)(48 + \beta^2(1 + \rho^2)(29 + 9\beta^2(1 + \rho^2))) + \right. \\
 &\quad \left. (2 + \beta^2(1 + \rho^2))(12 + \beta^2(1 + \rho^2)(10 + 3\beta^2(1 + \rho^2))) \cos(2\beta^2 \rho) + 2\beta^2 \rho(4 + 3\beta^2(1 + \rho^2)) \sin(2\beta^2 \rho) \right) \\
 \tau_5 &= -\frac{9}{2 \left(1 - 2e^{-\beta^2} \cos(\beta^2 \rho) + e^{-2\beta^2} \right)^2} \left((12 + \beta^2(1 + \rho^2)(20 + \beta^2(1 + \rho^2)(13 + 4\beta^2(1 + \rho^2)))) \cos(\beta^2 \rho) \right. \\
 &\quad \left. + 2\beta^2 \rho(1 + \rho^2)(1 + \beta^2(1 + \rho^2)) \sin(\beta^2 \rho) \right) \\
 \tau_6 &= \frac{9}{2 \left(1 - 2e^{-\beta^2} \cos(\beta^2 \rho) + e^{-2\beta^2} \right)^2} (1 + \beta^2(1 + \rho^2))(2 + \beta^2(1 + \rho^2))(2 + \beta^2(1 + \rho^2))
 \end{aligned}$$

(147)

$$\sqrt{\eta_{\text{het, QPD, top, } \circ}} = \sqrt{\eta_{\text{het, 0}}} \left(\sum_{i=0}^4 t_i \theta^i \right) + \mathcal{O}(\theta^5, \rho^3)$$

$$\sqrt{\eta_{\text{het, 0}}} = \frac{2w_r w_m}{w_r^2 + w_m^2} \frac{1}{\sqrt{1 - \exp(-\beta_r^2)} \sqrt{1 - \exp(-\beta_m^2)}}$$

$$t_0 = \frac{1}{2(1 - e^{-\beta^2})} \left(2 - \rho^2 + (-4 + 2\rho^2 + \beta^4 \rho^2) e^{-\beta^2} + (2 - \rho^2) e^{-2\beta^2} \right)$$

$$t_1 = \frac{(kw_{\text{eff}})\rho}{4\pi(1 - e^{-\beta^2})} \left(\sqrt{\pi} \operatorname{erf}(\beta) - (2\beta(1 + 2\beta^2) + \sqrt{\pi}(1 - 2\beta^2) \operatorname{erf}(\beta)) e^{-\beta^2} + 2\beta e^{-2\beta^2} \right)$$

$$t_2 = \frac{(kw_{\text{eff}})^2}{16\pi^2(1 - e^{-\beta^2})^3} \sum_{n=0}^4 \tau_n e^{-n\beta^2}$$

$$\tau_0 = \pi \left((4 - 5\rho^2) \operatorname{erf}^2(\beta) + \pi(3\rho^2 - 2) \right)$$

$$\tau_1 = \pi^2 \left(2\beta^2 - (\beta^6 + \beta^4 + \beta^2 + 12)\rho^2 + 8 \right) - 2\pi \left((\beta^4 + 2\beta^2 - 5)\rho^2 + 4 \right) \operatorname{erf}^2(\beta) + 4\sqrt{\pi}\beta \left((2\beta^4 + \beta^2 + 5)\rho^2 - 4 \right) \operatorname{erf}(\beta)$$

$$\tau_2 = \beta^2 \left(4 - (4\beta^4 + 2\beta^2 + 5)\rho^2 \right) + \pi^2 \left((\beta^6 + 2\beta^4 + 3\beta^2 + 18)\rho^2 - 6(\beta^2 + 2) \right) + 8\sqrt{\pi}\beta \left((\beta^4 + \beta^2 - 5)\rho^2 + 4 \right) \operatorname{erf}(\beta) + \pi \left((-4\beta^4 + 4\beta^2 - 5)\rho^2 + 4 \right) \operatorname{erf}^2(\beta)$$

$$\tau_3 = -8\beta^2 \left((\beta^4 - 5)\rho^2 + 4 \right) + \pi^2 \left(6\beta^2 - (\beta^4 + 3\beta^2 + 12)\rho^2 + 8 \right) + 4\sqrt{\pi}\beta \left((2\beta^4 - 3\beta^2 + 5)\rho^2 - 4 \right) \operatorname{erf}(\beta)$$

$$\tau_4 = 4\beta^2 \left((2\beta^2 - 5)\rho^2 + 4 \right) + \pi^2 \left(\beta^2(\rho^2 - 2) + 3\rho^2 - 2 \right)$$

$$t_3 = -\frac{(kw_{\text{eff}})^3 \rho}{144\sqrt{2}\pi^3(1 - e^{-\beta^2})^3} \sum_{n=0}^4 \tau_n e^{-n\beta^2}$$

$$\tau_0 = 9\pi^{\frac{3}{2}} \operatorname{erf}(\beta)^3$$

$$\tau_1 = \pi \left(-4\pi\beta^3(3 + 2\beta^2) + 3 \operatorname{erf}(\beta)(\pi^{\frac{3}{2}}\beta^2(2 + 3\beta^2) - 6\beta(3 + 2\beta^2) \operatorname{erf}(\beta) + 3\sqrt{\pi}(-1 + 2\beta^2) \operatorname{erf}^2(\beta)) \right)$$

$$\tau_2 = -2\pi^2\beta^2(\beta^2 - 12) + 3\sqrt{\pi}\beta^2(34 + 48\beta^2 - \pi^2(4 + 3\beta^2)) \operatorname{erf}(\beta) + 18\pi\beta(3 - 4\beta^2) \operatorname{erf}^2(\beta)$$

$$\tau_3 = -2\beta^2 \left(6(6 + \pi^2)\beta + (72 - 5\pi^2)\beta^3 - 3\sqrt{\pi}(\pi^2 - 18 + 12\beta^2) \operatorname{erf}(\beta) \right)$$

$$\tau_4 = 72\beta^3$$

$$t_4 = \frac{(kw_{\text{eff}})^4}{2304\pi^4(1 - e^{-\beta^2})^3} \sum_{n=0}^4 \tau_n e^{-n\beta^2} - \frac{(kw_{\text{eff}})^4 \rho^2}{4608\pi^4(1 - e^{-\beta^2})^5} \sum_{n=0}^6 \sigma_n e^{-n\beta^2}$$

$$\tau_0 = \pi^2 \left(9\pi^2 - 12\pi \operatorname{erf}^2(\beta) - 36 \operatorname{erf}^4(\beta) \right)$$

$$\tau_1 = -\frac{9}{2}\pi^4 \left(8 + 2\beta^2 + \beta^4 \right) + 4\pi^{\frac{3}{2}} \operatorname{erf}(\beta) \left(4\pi\beta(3 + 4\beta^2) + 3\pi^{\frac{3}{2}}(2 - 3\beta^2) \operatorname{erf}(\beta) + 72\beta \operatorname{erf}^2(\beta) \right)$$

$$\tau_2 = -16\pi^2\beta^2(3 + 8\beta^2) + \frac{27}{2}\pi^4(4 + 2\beta^2 + \beta^4) + 4\pi \operatorname{erf}(\beta) \left(4\pi^{\frac{3}{2}}\beta(\beta^2 - 6) - 3\pi^2 \operatorname{erf}(\beta) + 9(\pi^2 - 24)\beta^2 \operatorname{erf}(\beta) \right)$$

$$\tau_3 = 16\pi^2\beta^2(6 + 7\beta^2) - \frac{9}{2}\pi^4(8 + 6\beta^2 + 3\beta^4) + 16\sqrt{\pi}\beta(72\beta^2 + \pi^2(3 - 5\beta^2)) \operatorname{erf}(\beta)$$

$$\tau_4 = -576\beta^4 + 12\pi^2\beta^2(-3 + \beta^2) + \frac{9}{2}(2 + 2\beta^2 + \beta^4)$$

$$\sigma_0 = 3\pi^2 \left(15\pi^2 - 10\pi \operatorname{erf}^2(\beta) - 72 \operatorname{erf}^4(\beta) \right)$$

$$\sigma_1 = -\frac{9}{2}\pi^4(60 + 6\beta^2 - \beta^4 + 2\beta^6 + \beta^8) + 2\pi^{\frac{3}{2}} \operatorname{erf}(\beta) \left(4\pi\beta(15 + 5\beta^2 + 6\beta^4 + 8\beta^6) - 3\pi^{\frac{3}{2}}(-20 + 11\beta^2 + 14\beta^4 + 6\beta^6) \operatorname{erf}(\beta) + 72\beta(12 + 5\beta^2 + 2\beta^4) \operatorname{erf}^2(\beta) - 54\sqrt{\pi}(-4 + 4\beta^2 + \beta^4) \operatorname{erf}^3(\beta) \right)$$

$$\begin{aligned}
\sigma_2 &= -8\pi^2\beta^2(15 + 10\beta^2 + 20\beta^4 + 32\beta^6) - \frac{9}{2}\pi^4(-150 - 30\beta^2 + 3\beta^4 - 6\beta^6 + \beta^8) + \\
&\quad 2\pi \operatorname{erf}(\beta) \left(4\pi^{\frac{3}{2}}\beta(-60 + 13\beta^2 + 47\beta^4 + 64\beta^6) + 9 \operatorname{erf}(\beta) (-10\pi^2 + (-288 + 11\pi^2)\beta^2 + 4(-60 + \pi^2)\beta^4 + \right. \\
&\quad \left. -10(16 + \pi^2)\beta^6 + 16\sqrt{\pi}\beta(-12 + 7(\beta^2 + \beta^4)) \operatorname{erf}(\beta) - 12\pi(1 - 2\beta^2 + 2\beta^4) \operatorname{erf}^2(\beta) \right) \\
\sigma_3 &= -8\pi^2\beta^2(-60 - 7\beta^2 + 20\beta^4 + 78\beta^6) + \frac{9}{2}\pi^4(-200 - 60\beta^2 + 2\beta^4 - 6\beta^6 + 5\beta^8) + \\
&\quad + 6\sqrt{\pi} \operatorname{erf}(\beta) (96\beta^3(12 + 15\beta^2 + 14\beta^4) - 4\pi^2\beta(-30 + 23\beta^2 + 29\beta^4) + \sqrt{\pi}(-48\beta^2(-36 + 6\beta^2 + 25\beta^4) + \\
&\quad + \pi^2(20 - 33\beta^2 + 18\beta^4 + 24\beta^6)) \operatorname{erf}(\beta) + 24\pi\beta(12 - 19\beta^2 + 14\beta^4) \operatorname{erf}^2(\beta)) \\
\sigma_4 &= -1152\beta^4(3 + 5\beta^2 + 6\beta^4) + \frac{9}{2}\pi^4(150 + 60\beta^2 + 2\beta^4 + 2\beta^6 - 3\beta^8) + 24\pi^2\beta^2(-30 + \beta^2(13 + 30(\beta^2 + \beta^4))) + \\
&\quad - 8\sqrt{\pi}\beta(-144\beta^2(-12 - 3\beta^2 + 7\beta^4) + \pi^2(60 - 79\beta^2 - 9\beta^4 + 62\beta^6)) \operatorname{erf}(\beta) + 6\pi(\pi^2(-5 + 6\beta^2)(1 - \beta^2 + 2\beta^4) + \\
&\quad -48\beta^2(18 - 21\beta^2 + 10\beta^4)) \operatorname{erf}^2(\beta) \\
\sigma_5 &= -\frac{27}{2}\pi^4(20 + 10\beta^2 + \beta^4) - 576\beta^4(-12 - 8\beta^2 + 3\beta^4) + 8\pi^2\beta^2(60 - 59\beta^2 - 40\beta^4 + 20\beta^6) + \\
&\quad - 8\sqrt{\pi}\beta(-72\beta^2(12 - 9\beta^2 + 2\beta^4) + \pi^2(-15 + 28\beta^2 - 25\beta^4 + 10\beta^6)) \operatorname{erf}(\beta) \\
\sigma_6 &= 1152\beta^4(-3 + \beta^2) + \frac{9}{2}\pi^4(10 + 6\beta^2 + \beta^4) - 8\pi^2\beta^2(15 - 23\beta^2 + 10\beta^4)
\end{aligned}$$

(148)

References

- [1] Pizzella G 2016 *The European Physical Journal H* **41** 267–302 URL <https://doi.org/10.1140/epjh/e2016-70036-8>
- [2] Moss G E, Miller L R and Forward R L 1971 *Appl. Opt.* **10** 2495–2498 URL <https://opg.optica.org/ao/abstract.cfm?URI=ao-10-11-2495>
- [3] Weiss R 2022 *General Relativity and Gravitation* **54** 153 ISSN 1572-9532 URL <https://doi.org/10.1007/s10714-022-03021-3>
- [4] Abbott B P *et al.* (LIGO Scientific Collaboration and Virgo Collaboration) 2016 *Phys. Rev. Lett.* **116**(6) 061102 URL <https://link.aps.org/doi/10.1103/PhysRevLett.116.061102>
- [5] Branchesi M, Maggiore M, Alonso D, Badger C, Banerjee B, Beirnaert F, Belgacem E, Bhagwat S, Boileau G, Borhanian S, Brown D D, Leong Chan M, Cusin G, Danilishin S L, Degallaix J, De Luca V, Dhani A, Dietrich T, Dupletsa U, Foffa S, Franciolini G, Freise A, Gemme G, Goncharov B, Ghosh A, Gulminelli F, Gupta I, Kumar Gupta P, Harms J, Hazra N, Hild S, Hinderer T, Siong Heng I, Iacovelli F, Janquart J, Janssens K, Jenkins A C, Kalaghatgi C, Korovesi X, Li T G, Li Y, Loffredo E, Maggio E, Mancarella M, Mapelli M, Martinovic K, Maselli A, Meyers P, Miller A L, Mondal C, Muttoni N, Narola H, Oertel M, Oganessian G, Pacilio C, Palomba C, Pani P, Pasqualetti A, Perego A, PÉrigois C, Pieroni M, Piccinni O J, Puecher A, Puppo P, Ricciardone A, Riotto A, Ronchini S, Sakellariadou M, Samajdar A, Santoliquido F, Sathyaprakash B, Steinlechner J, Steinlechner S, Utina A, Van Den Broeck C and Zhang T 2023 *Journal of Cosmology and Astroparticle Physics* **2023** 068 ISSN 1475-7516 URL <http://dx.doi.org/10.1088/1475-7516/2023/07/068>
- [6] Evans M, Corsi A, Afe C, Ananyeva A, Arun K G, Ballmer S, Bandopadhyay A, Barsotti L, Baryakhtar M, Berger E, Berti E, Biscoveanu S, Borhanian S, Broekgaarden F, Brown D A, Cahillane C, Campbell L, Chen H Y, Daniel K J, Dhani A, Driggers J C, Effler A, Eisenstein R, Fairhurst S, Feicht J, Fritschel P, Fulda P, Gupta I, Hall E D, Hammond G, Hannuksela O A, Hansen H, Haster C J, Kacanja K, Kamai B, Kashyap R, Key J S, Khadkikar S, Kontos A, Kuns K, Landry M, Landry P, Lantz B, Li T G F, Lovelace G, Mandic V, Mansell G L, Martynov D, McCuller L, Miller A L, Nitz A H, Owen B J, Palomba C, Read J, Phurailatpam H, Reddy S, Richardson J, Rollins J, Romano J D, Sathyaprakash B S, Schofield R, Shoemaker D H, Sigg D, Singh D, Slagmolen B, Sledge P, Smith J, Soares-Santos M, Strunk A, Sun L, Tanner D, van Son L A C, Vitale S, Willke B, Yamamoto H and Zucker M 2023 Cosmic explorer: A submission to the nsf mpsac nggw subcommittee (*Preprint* 2306.13745) URL <https://arxiv.org/abs/2306.13745>
- [7] Cahillane C and Mansell G 2022 *Galaxies* **10** 36 URL <https://doi.org/10.3390/galaxies10010036>
- [8] Colpi M, Danzmann K, Hewitson M, Holley-Bockelmann K, Jetzer P, Nelemans G, Petiteau A, Shoemaker D, Sopuerta C, Stebbins R, Tanvir N, Ward H, Weber W J, Thorpe I, Dauriskikh A, Deep A, Núñez I F, Marirrodiga C G, Gehler M, Halain J P, Jennrich O, Lammers U, Larrañaga J, Lieser M, Lützgendorf N, Martens W, Mondin L, Niño A P, Amaro-Seoane P, Sedda M A, Auclair P, Babak S, Baghi Q, Baibhav V, Baker T, Bayle J B, Berry C, Berti E, Boileau G, Bonetti M, Brito R, Buscicchio R, Calcagni G, Capelo P R, Caprini C, Caputo A, Castelli E, Chen H Y, Chen X, Chua A, Davies G, Derdzinski A, Domcke V F, Doneva D, Dvorkin I, Ezquiaga J M, Gair J, Haiman Z, Harry I, Hartwig O, Hees A, Heffernan A, Husa S, Izquierdo D, Karnesis N, Klein A, Korol V, Korsakova N, Kupfer T, Laghi D, Lamberts A, Larson S, Jeune M L, Lewicki M, Littenberg T, Madge E, Mangiagli A, Marsat S, Vilchez I M, Maselli A, Mathews J, van de Meent M, Muratore M, Nardini G, Pani P, Peloso M, Pieroni M, Pound A, Quelquejay-Leclere H, Ricciardone A, Rossi E M, Sartirana A, Savalle E, Sberna L, Sesana A, Shoemaker D, Slutsky J, Sotiriou T, Speri L, Staab M, Steer D, Tamanini N, Tasinato G, Torrado J, Torres-Orjuela A, Toubiana A, Vallisneri M, Vecchio A, Volonteri M, Yagi K and Zwick L 2024 Lisa definition study report (*Preprint* 2402.07571) URL <https://arxiv.org/abs/2402.07571>
- [9] ESA 2024 Capturing the ripples of spacetime: Lisa gets go-ahead URL https://www.esa.int/Science_Exploration/Space_Science/LISA/Capturing_the_ripples_of_spacetime_LISA_gets_go-ahead
- [10] Armano M, Audley H, Auger G, Baird J T, Bassan M, Binetruy P, Born M, Bortoluzzi D, Brandt N, Caleno M, Carbone L, Cavalleri A, Cesarini A, Ciani G, Congedo G, Cruise A M, Danzmann K, de Deus Silva M, De Rosa R, Diaz-Aguiló M, Di Fiore L, Diepholz I, Dixon G, Dolesi R, Dunbar N, Ferraioli L, Ferroni V, Fichter W, Fitzsimons E D, Flatscher R, Freschi M, García Marín A F,

- García Marirrodriaga C, Gerndt R, Gesa L, Gibert F, Giardini D, Giusteri R, Guzmán F, Grado A, Grimani C, Grynagier A, Grzymisch J, Harrison I, Heinzl G, Hewitson M, Hollington D, Hoyland D, Hueller M, Inchauspé H, Jennrich O, Jetzer P, Johann U, Johlander B, Karnesis N, Kaune B, Korsakova N, Killow C J, Lobo J A, Lloro I, Liu L, López-Zaragoza J P, Maarschalkerweerd R, Mance D, Martín V, Martín-Polo L, Martino J, Martín-Porqueras F, Madden S, Mateos I, McNamara P W, Mendes J, Mendes L, Monsky A, Nicolodi D, Nofrarias M, Paczkowski S, Perreur-Lloyd M, Petiteau A, Pivato P, Plagnol E, Prat P, Ragnit U, Raïs B, Ramos-Castro J, Reiche J, Robertson D I, Rozemeijer H, Rivas F, Russano G, Sanjuán J, Sarra P, Schleicher A, Shaul D, Slutsky J, Sopena C F, Stanga R, Steier F, Sumner T, Texier D, Thorpe J I, Trenkel C, Tröbs M, Tu H B, Vetrugno D, Vitale S, Wand V, Wanner G, Ward H, Warren C, Wass P J, Wealthy D, Weber W J, Wissel L, Wittchen A, Zambotti A, Zanonì C, Ziegler T and Zweifel P 2016 *Phys. Rev. Lett.* **116**(23) 231101 URL <https://link.aps.org/doi/10.1103/PhysRevLett.116.231101>
- [11] Armano M, Audley H, Baird J, Binetruy P, Born M, Bortoluzzi D, Castelli E, Cavalleri A, Cesarini A, Cruise A M, Danzmann K, de Deus Silva M, Diepholz I, Dixon G, Dolesi R, Ferraioli L, Ferroni V, Fitzsimons E D, Freschi M, Gesa L, Gibert F, Giardini D, Giusteri R, Grimani C, Grzymisch J, Harrison I, Heinzl G, Hewitson M, Hollington D, Hoyland D, Hueller M, Inchauspé H, Jennrich O, Jetzer P, Karnesis N, Kaune B, Korsakova N, Killow C J, Lobo J A, Lloro I, Liu L, López-Zaragoza J P, Maarschalkerweerd R, Mance D, Meshksar N, Martín V, Martín-Polo L, Martino J, Martín-Porqueras F, Mateos I, McNamara P W, Mendes J, Mendes L, Nofrarias M, Paczkowski S, Perreur-Lloyd M, Petiteau A, Pivato P, Plagnol E, Ramos-Castro J, Reiche J, Robertson D I, Rivas F, Russano G, Slutsky J, Sopena C F, Sumner T, Texier D, Thorpe J I, Vetrugno D, Vitale S, Wanner G, Ward H, Wass P J, Weber W J, Wissel L, Wittchen A and Zweifel P 2018 *Phys. Rev. Lett.* **120**(6) 061101 URL <https://link.aps.org/doi/10.1103/PhysRevLett.120.061101>
- [12] Wanner G 2019 *Nature Physics* **15** 200–202 ISSN 1745-2481 URL <https://doi.org/10.1038/s41567-019-0462-3>
- [13] Danzmann K, Prince T and the LISA international science team 2011 Assessment study report (yellow book) URL https://sci.esa.int/documents/35005/36499/1567258681608-LISA_YellowBook_ESA-SRE-2011-3_Feb2011.pdf
- [14] Chwalla M, Danzmann K, Alvarez M D, Delgado J E, Barranco G F, Fitzsimons E, Gerberding O, Heinzl G, Killow C, Lieser M, Perreur-Lloyd M, Robertson D, Rohr J, Schuster S, Schwarze T, Tröbs M, Wanner G and Ward H 2020 *Physical Review Applied* **14** URL <https://doi.org/10.1103/PhysRevApplied.14.014030>
- [15] Brzozowski W, Robertson D, Fitzsimons E, Ward H, Keogh J, Taylor A, Milanova M, Perreur-Lloyd M, Ali Z, Earle A, Clarkson D, Sharman R, Wells M and Parr-Burman P 2022 The LISA optical bench: an overview and engineering challenges *Space Telescopes and Instrumentation 2022: Optical, Infrared, and Millimeter Wave* vol 12180 ed Coyle L E, Matsuura S and Perrin M D International Society for Optics and Photonics (SPIE) p 1218000 URL <https://doi.org/10.1117/12.2627465>
- [16] van Veggel A M A and Killow C J 2014 *Advanced Optical Technologies* **3** 293–307 URL <https://doi.org/10.1515/aot-2014-0022>
- [17] Wanner G, Karnesis N and on behalf of the LISA Pathfinder collaboration 2017 *Journal of Physics: Conference Series* **840** 012043 URL <https://dx.doi.org/10.1088/1742-6596/840/1/012043>
- [18] Fitzsimons E, Martino J and Vetrugno D 2024 *LISA Performance Model and Error Budget*
- [19] Tröbs M, Schuster S, Lieser M, Zwetz M, Chwalla M, Danzmann K, Barranco G F, Fitzsimons E D, Gerberding O, Heinzl G, Killow C J, Perreur-Lloyd M, Robertson D I, Schwarze T S, Wanner G and Ward H 2018 *Classical and Quantum Gravity* **35** 105001 URL <https://dx.doi.org/10.1088/1361-6382/aab86c>
- [20] Hartig M S, Paczkowski S, Hewitson M, Heinzl G and Wanner G 2025 *Phys. Rev. D* **111**(4) 043048 URL <https://link.aps.org/doi/10.1103/PhysRevD.111.043048>
- [21] Wu Y L, Luo Z R, Wang J Y, Bai M, Bian W, Cai R G, Cai Z M, Cao J, Chen D J, Chen L, Chen L S, Chen M W, Chen W B, Chen Z Y, Cong L X, Deng J F, Dong X L, Duan L, Fan S Q, Fan S S, Fang C, Fang Y, Feng K, Feng P, Feng Z, Gao R H, Gao R L, Guo Z K, He J W, He J B, Hou X, Hu L, Hu W R, Hu Z Q, Huang M J, Jia J J, Jiang K L, Jin G, Jin H B, Kang Q, Lei J G, Li B Q, Li D J, Li F, Li H S, Li H W, Li L F, Li W, Li X K, Li Y M, Li Y G, Li Y P, Li Y P, Li Z, Lin Z Y, Liu C, Liu D B, Liu H S, Liu

- H, Liu P, Liu Y R, Lu Z Y, Luo H W, Ma F L, Ma L F, Ma X S, Ma X, Man Y C, Min J, Niu Y, Peng J K, Peng X D, Qi K Q, Qiang L, Qiao C F, Qu Y X, Ruan W H, Sha W, Shen J, Shi X J, Shu R, Su J, Sui Y L, Sun G W, Tang W L, Tao H J, Tao W Z, Tian Z, Wan L F, Wang C Y, Wang J, Wang J, Wang L L, Wang S X, Wang X P, Wang Y K, Wang Z, Wang Z L, Wei Y X, Wu D, Wu L M, Wu P Z, Wu Z H, Xi D X, Xie Y F, Xin G F, Xu L X, Xu P, Xu S Y, Xu Y, Xue S W, Xue Z B, Yang C, Yang R, Yang S J, Yang S, Yang Y, Yang Z G, Yin Y L, Yu J P, Yu T, Zhang A B, Zhang C, Zhang M, Zhang X Q, Zhang Y Z, Zhao J, Zhao W W, Zhao Y, Zheng J H, Zhou C Y, Zhu Z C, Zou X B, Zou Z M and Collaboration T T S 2021 *Communications Physics* **4** 34 ISSN 2399-3650 URL <https://doi.org/10.1038/s42005-021-00529-z>
- [22] Luo J, Chen L S, Duan H Z, Gong Y G, Hu S, Ji J, Liu Q, Mei J, Milyukov V, Sazhin M, Shao C G, Toth V T, Tu H B, Wang Y, Wang Y, Yeh H C, Zhan M S, Zhang Y, Zharov V and Zhou Z B 2016 *Classical and Quantum Gravity* **33** 035010 URL <https://dx.doi.org/10.1088/0264-9381/33/3/035010>
- [23] Sheard B S, Heinzel G, Danzmann K, Shaddock D A, Klipstein W M and Folkner W M 2012 *Journal of Geodesy* **86** 1083–1095 ISSN 1432-1394 URL <https://doi.org/10.1007/s00190-012-0566-3>
- [24] Chwalla M, Danzmann K, Barranco G F, Fitzsimons E, Gerberding O, Heinzel G, Killow C J, Lieser M, Perreur-Lloyd M, Robertson D I, Schuster S, Schwarze T S, Tröbs M, Ward H and Zwetz M 2016 *Classical and Quantum Gravity* **33** 245015 URL <https://dx.doi.org/10.1088/0264-9381/33/24/245015>
- [25] Pizzella A 2025 *LISA optical bench development: experimental investigation of differential-wavefront sensing for a spaceborne gravitational wave detector* Ph.D. thesis Leibniz Universität Hannover URL <https://doi.org/10.15488/18487>
- [26] Pizzella A, Dovale-Álvarez M, Cano P M, Álvarez R G, Bode C, Delgado J J E and Heinzel G 2025 *Phys. Rev. D* **112**(8) 082005 URL <https://link.aps.org/doi/10.1103/sqgt-plx6>
- [27] Huarcaya V, Álvarez M D, Penkert D, Gozzo S, Cano P M, Yamamoto K, Delgado J J E, Mehmet M, Danzmann K and Heinzel G 2023 *Phys. Rev. Appl.* **20**(2) 024078 URL <https://link.aps.org/doi/10.1103/PhysRevApplied.20.024078>
- [28] Donley E A, Heavner T P, Levi F, Tataw M O and Jefferts S R 2005 *Review of Scientific Instruments* **76** 063112 ISSN 0034-6748 (Preprint https://pubs.aip.org/aip/rsi/article-pdf/doi/10.1063/1.1930095/16000353/063112_1_online.pdf) URL <https://doi.org/10.1063/1.1930095>
- [29] Fernandez Barranco G 2017 *Photodetection in intersatellite laser interferometers* Ph.D. thesis Leibniz Universität Hannover URL <https://doi.org/10.15488/3866>
- [30] Fernández Barranco G, Sheard B S, Dahl C, Mathis W and Heinzel G 2018 *IEEE Sensors Journal* **18** 7414–7420
- [31] Siegman A 1986 *Lasers* (University Science Books) ISBN 9780685055953 URL <https://books.google.de/books?id=qBBaDQEACAAJ>
- [32] Gerberding O, Dahl C, Kullmann J, Tröbs M, Bykov I, Barke S, Brause N, Esteban Delgado J J, Schwarze T, Reiche J, Danzmann K, Rasmussen T, Hansen T, Enggaard A, Pedersen S, Jennrich O, Suess M, Sodnik Z and Heinzel G 2015 *The Review of scientific instruments* **86**
- [33] Gerberding O 2014 *Phase readout for satellite interferometry* Ph.D. thesis Leibniz Universität Hannover URL <https://doi.org/10.15488/8255>
- [34] Bode C 2024 *Noise in the LISA phasemeter* Ph.D. thesis Leibniz Universität Hannover URL <https://doi.org/10.15488/17997>
- [35] Hartig M S, Schuster S, Heinzel G and Wanner G 2023 *Journal of Optics* **25** 055601 URL <https://doi.org/10.1088/2040-8986/acc3ac>
- [36] Morrison E, Meers B J, Robertson D I and Ward H 1994 *Appl. Opt.* **33** 5041–5049 URL <https://opg.optica.org/ao/abstract.cfm?URI=ao-33-22-5041>
- [37] Morrison E, Meers B J, Robertson D I and Ward H 1994 *Appl. Opt.* **33** 5037–5040 URL <https://opg.optica.org/ao/abstract.cfm?URI=ao-33-22-5037>

- [38] Hechenblaikner G 2010 *J. Opt. Soc. Am. A* **27** 2078–2083 URL <https://opg.optica.org/josaa/abstract.cfm?URI=josaa-27-9-2078>
- [39] Heinzl G, Álvarez M D, Pizzella A, Brause N and Delgado J J E 2020 *Phys. Rev. Appl.* **14**(5) 054013 URL <https://link.aps.org/doi/10.1103/PhysRevApplied.14.054013>
- [40] Wissel L, Wittchen A, Schwarze T S, Hewitson M, Heinzl G and Halloin H 2022 *Phys. Rev. Appl.* **17**(2) 024025 URL <https://link.aps.org/doi/10.1103/PhysRevApplied.17.024025>
- [41] Wanner G, Heinzl G, Kochkina E, Mahrtdt C, Sheard B S, Schuster S and Danzmann K 2012 *Optics Communications* **285** 4831–4839 ISSN 0030-4018 URL <https://www.sciencedirect.com/science/article/pii/S0030401812008528>
- [42] Wissel L, Hewitson M and Heinzl G 2024 *Phys. Rev. Appl.* **22**(4) 044048 URL <https://link.aps.org/doi/10.1103/PhysRevApplied.22.044048>
- [43] Wanner G, Karnesis N and on behalf of the LISA Pathfinder collaboration 2017 *Journal of Physics: Conference Series* **840** 012043 URL <https://doi.org/10.1088/1742-6596/840/1/012043>
- [44] Wanner G 2010 *Complex optical systems in space : numerical modelling of the heterodyne interferometry of LISA Pathfinder and LISA* Ph.D. thesis Leibniz Universität Hannover URL <https://doi.org/10.15488/7550>
- [45] Armano M, Audley H, Baird J, Binetruy P, Born M, Bortoluzzi D, Castelli E, Cavalleri A, Cesarini A, Cruise A M, Danzmann K, de Deus Silva M, Diepholz I, Dixon G, Dolesi R, Ferraioli L, Ferroni V, Fitzsimons E D, Freschi M, Gesa L, Giardini D, Gibert F, Giusteri R, Grimani C, Grzymisch J, Harrison I, Hartig M S, Heinzl G, Hewitson M, Hollington D, Hoyland D, Hueller M, Inchauspé H, Jennrich O, Jetzer P, Johann U, Johlander B, Karnesis N, Kaune B, Killow C J, Korsakova N, Lobo J A, López-Zaragoza J P, Maarschalkerweerd R, Mance D, Martín V, Martín-Polo L, Martín-Porqueras F, Martino J, McNamara P W, Mendes J, Mendes L, Meshksar N, Nofrarias M, Paczkowski S, Perreur-Lloyd M, Petiteau A, Plagnol E, Ramos-Castro J, Reiche J, Rivas F, Robertson D I, Russano G, Sanjuan J, Slutsky J, Sopena C F, Sumner T, Tevlin L, Texier D, Thorpe J I, Vetrugno D, Vitale S, Wanner G, Ward H, Wass P J, Weber W J, Wissel L, Wittchen A and Zweifel P 2023 *Phys. Rev. D* **108**(10) 102003 URL <https://link.aps.org/doi/10.1103/PhysRevD.108.102003>
- [46] Mistry T e a 2024 The eyes of lisa URL <https://app.oxfordabstracts.com/content/events/5189/submitters/405298/submissions/fe-412377de-ee7f-408e-849d-84ca70d81af8/questions/91860/file/e18cb94a-84d5-4284-b64f-39c13cb08bb4.pdf>
- [47] Francis S P 2017 *Multi-link laser interferometer architecture for a next generation GRACE* Ph.D. thesis Australian National University
- [48] Bendat J S and Piersol A G 2000 *Random Data: Analysis and Measurement Procedures* 3rd ed (USA: John Wiley & Sons, Inc.) ISBN 0471317330